Injectivity decline in ultra-filtered water flooding of high permeability sandstone reservoir

Ali Murtaza

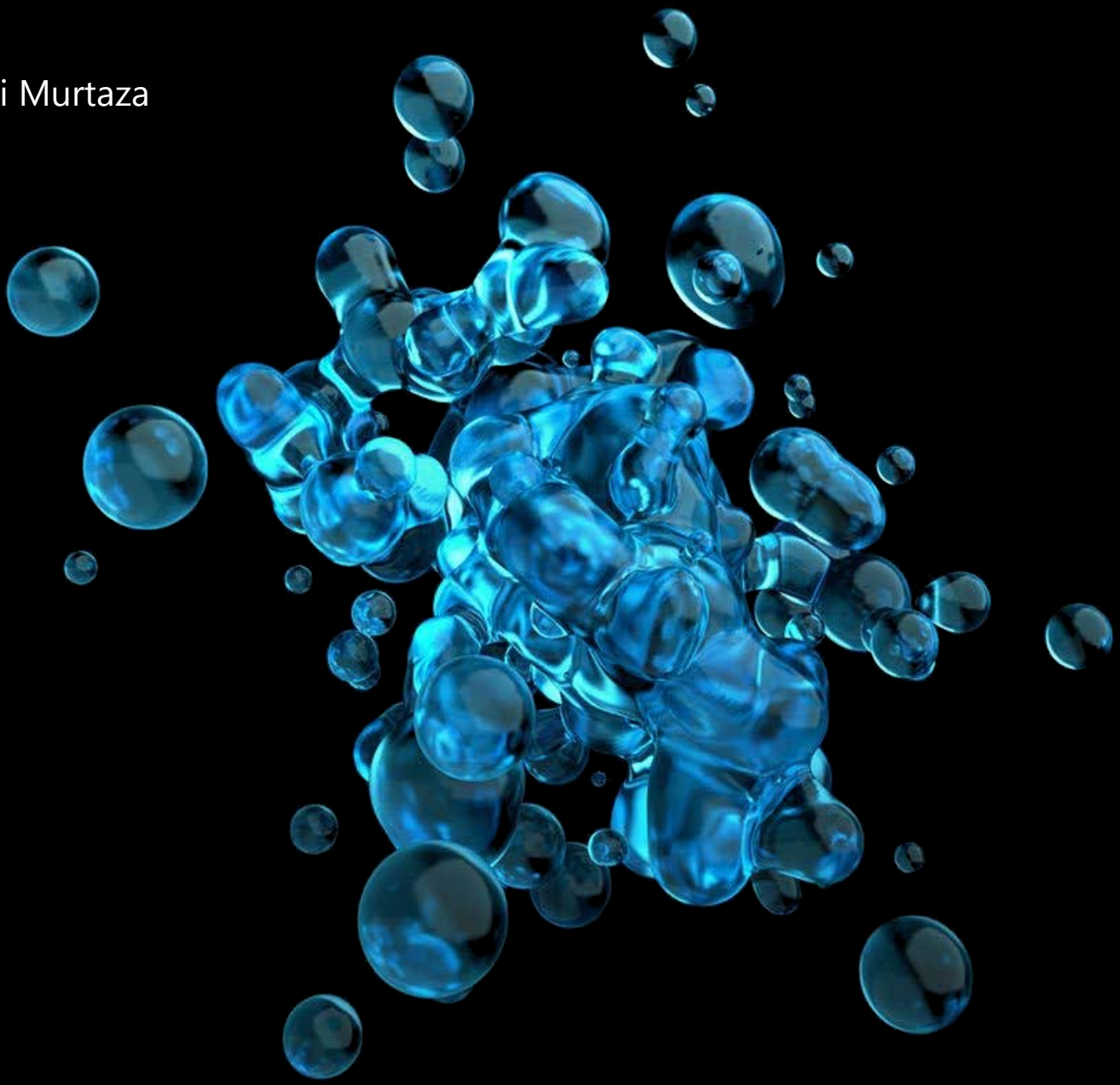

TU Delft
Delft University of Technology

Injectivity Decline in Ultra-Filtered Water Flooding of High Permeability Sandstone Reservoirs

By

Ali Murtaza

in partial fulfilment of the requirements for the degree of

Master of Science

in Applied Earth sciences

Petroleum Engineering and Geosciences

at the Delft University of Technology,

to be defended publicly on Monday November 27, 2017 at 02:00 PM

Supervisors:

Dr. Ali Fadili	(Shell Global Solutions B.V.)
Prof. Dr. P.L.J. Zitha	(Delft University of Technology)
Dr. Paul Van Den Hoek	(Delft University of Technology)

Thesis Committee:

Chair: Prof. Dr. P.L.J. Zitha	(Delft University of Technology)
Dr. Ali Fadili	(Shell Global Solutions B.V.)
Dr. Paul Van Den Hoek	(Delft University of Technology)
Dr. K.H.A.A. Wolf	(Delft University of Technology)

Abstract

Water injection is a core element of geothermal, petroleum and waste water management industries where water is injected into the subsurface after treatment and filtration to comply with environmental regulations and water quality requirements. Some impurities still remain in the water even after the filtration process. It has been widely reported that water injection operations encounter severe injectivity decline which is of substantial concern for field management. Total dissolved and suspended solids in injection water are one of the significant reasons for injectivity decline. These solids are then filtered by the porous media and cause formation damage which can result in significant injectivity decline.

Major past studies have assumed typical filtration techniques (micro-filtration) where the size of remaining dispersed particles in the water are reduced to ~2 microns. Hence, the majority of the experimental studies have used suspended particles of ~1-5 microns to investigate injectivity decline. These studies show that initially internal filter cake starts to develop and after some transition time external filter cake is formed, after which injection face is almost completely plugged. However, not many studies have been performed with ultrafiltration where remaining dispersed particle size in injection water is reduced to nano size range.

In this study, injectivity decline by ultra-filtered water injection was investigated experimentally. To mimic ultra-filtered water, spherical silica nanoparticles of 120 nm diameter were used as dispersed particles in the injected water. First, stability study of nanoparticle colloid was carried out by varying nanoparticle concentration, brine compositions and pH. Hydrodynamic size and zeta potential measurements showed that there exists a salinity and pH range in which nanoparticle colloid remain within the expected size range.

Core flood experiments were conducted on Bentheimer sandstone core plugs. Pressure measurements along the core and influent/effluent analysis were used to study the transport and retention of nanoparticles in porous media. Experimental results showed about 50 to 70 percent less injectivity decline compared to micron size suspended particles. Furthermore, results showed that external filter cake does not form by nanoparticle flow through porous media if the injection fluid's pH and salinity are kept within a defined range obtained from stability study. Only deep bed filtration takes place where three main retention mechanisms dominate i.e. surface deposition, plugging and entrainment.

Finally, a numerical model is presented in this study that describes deep bed filtration taking into account observed retention mechanisms. Model results are found to be in good agreement with experimental results.

Acknowledgement

Praise to Almighty for His countless blessings, mercy and protection.

I am delighted to take this opportunity to present my deepest gratitude to Dr. Ali Fadili for his continuous support and encouragement throughout the period of this study, particularly in the difficult times. Regular meetings, discussions and feedback helped me to tackle the problem at hand in a more efficient manner. I thank you for mentoring and guiding me with patience, intellect and professionalism in the right direction to achieve the goals of this study. I also owe my gratitude to Prof. Dr. Pacelli Zitha for his support and supervision. I am thankful to him for taking time out of his busy schedule whenever I requested. His inputs in experimental practices and procedures were extremely helpful. I would also like to express my gratitude to Dr. Paul van den Hoek for giving me the opportunity to work on this subject. His guidance enabled me to understand the concepts and problems associated with water flooding. Without them this thesis would never have been possible.

I thank Dr. Karl Heinz Wolf for accepting to be a part of the final thesis assessment committee. I would like to thank Marc Friebel, Henk van Asten, Michiel Slob and Jolanda van Haagen from TU Delft's Geoscience & Engineering Laboratory for helping me build the experimental setup and providing technical support throughout the experiments. Thanks to Arjan Thijssen from TU Delft's Micro Mechanics Laboratory for assisting in MIP analysis and SEM images. Thanks to Ruud Hendrikx from TU Delft's department of Materials Science and Engineering for XRD/XRF analysis. I would also like to extend my gratitude to Hilbert van der Linde and Ab Coorn from Shell Global Solutions, Rijswijk Laboratories for their assistance in nanoparticle characterization and CT scanning or core plugs.

I thank my parents for unparalleled and unconditional love and support they have provided me throughout my life. I dedicate this work to them as a token of appreciation.

Finally, I thank all my friends for their support and encouragement throughout my stay in TU Delft. I thank them all for making my stay in Netherlands a memorable one.

Ali Murtaza
The Hague, November 2017

Contents

Table of Figures

Chapter 1: Introduction

Chapter 2: Theory

Chapter 4: Experimental Methods

Chapter 5: Results & Discussion

Appendix B

Appendix C

1 Introduction

It is usually said in reference to energy and water that "*one does not flow without the other*" (World Energy Outlook, 2016). In geothermal and oil and gas industry, water is used for different purposes. In geothermal industry, energy is captured from geothermal sources naturally occurring in the subsurface. In all basic systems of geothermal power plants, hot water or steam is produced from the ground and is used to drive turbines either directly (dry steam and flash steam power plants) or indirectly (Binary cycle power plants) where produced hot water is used to heat a working fluid with low boiling temperature to generate electricity as shown below in Figure 1-1. The resulting colder water is injected back into the ground [1].

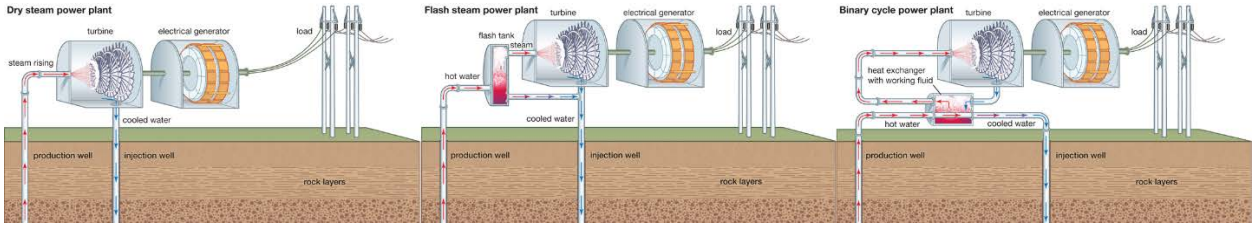

Figure 1-1: The three basic designs for geothermal power plants: dry steam, flash steam, and binary cycle. [Source: 2011 Encyclopaedia Britannica, Inc.]

In oil and gas industry water is produced with the production of hydrocarbons and is injected into the reservoir for either pressure support, improved or enhanced oil recovery or for simply disposing off [2]. This water might be naturally present along with hydrocarbons in form of an adjacent aquifer, in the adjacent layers or might have been previously injected to increase hydrocarbon production by water flooding or steam flooding operations [3]. Some of the water produced is the result of stimulation of unconventional oil and gas formations using hydraulic fracturing through which a large amount of water is injected under high pressure into the formation and is produced later (which is referred as *flow-back water*) [4]. Simple illustration of on-shore and off-shore water injection operation in oil and gas industry is shown in *Figure 1-2*.

Regardless of how the water is produced, it has remained a challenge to clean and inject water into the subsurface. Drastic decline of well injectivity is widely reported during seawater injection, produced water re-injection and injection of waste water for disposal [5].

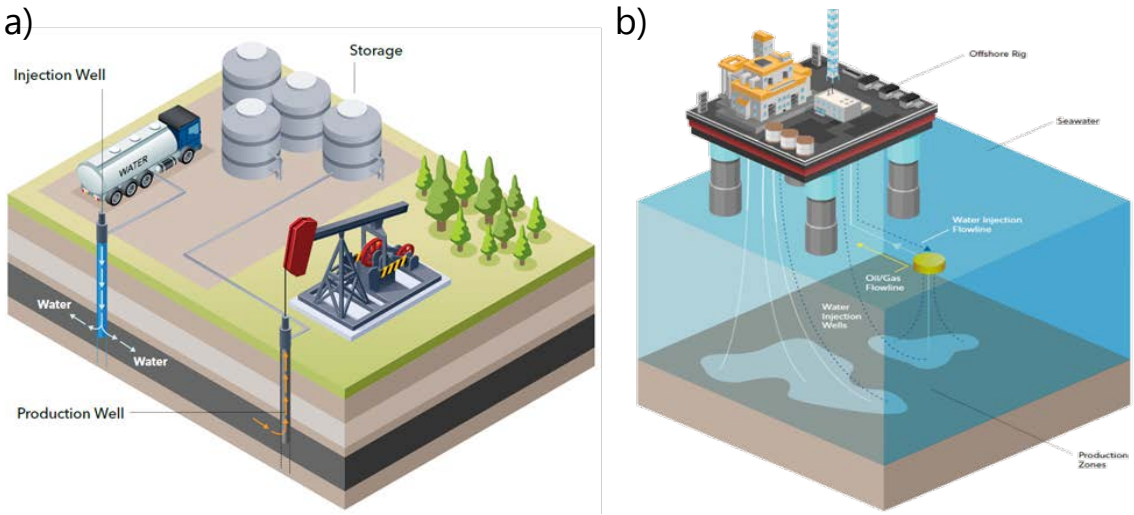

Figure 1-2: Illustration of a) Onshore water-flooding operation, b) Offshore water flooding operations [Source: Xylem Inc., 2014]

Produced water from oil and gas industry globally was approximately 1.7 times more than the total hydrocarbon production according to International association of Oil and Gas Producers (IOGP) in 2014. 90% of the produced water onshore was re-injected in to the subsurface whereas on average 28% of produced water was re-injected offshore[a] globally [6] *Figure 1-3*. As per United States National Energy Technology Laboratory (NETL), about 21 billion barrels (bbls) of water is produced each year that is about 57 million bbls per day. According to Ground Water Protection Council (GWPC) report, in US in 2012, about 93% of the produced water was injected onshore (46% was injected for enhanced recovery, 40% was injected into non-commercial injection wells, and 7% was injected into commercial disposal wells) whereas 20% was injected offshore [7]. Similar trends are also reported by the oil and gas UK environment report 2016 where 20% of the produced water in the region of United Kingdom Continental Shelf (UKCS) is re-injected. In geothermal industry vast volumes of water are re-injected into the subsurface. According to Argonne national laboratory report, in California geothermal power plants about 0.3-1.05 million bbls of water is injected per day and around 0.27-0.35 million bbls of water is used for all stimulation activities for one well [8]. These numbers show the importance of water injection and the need of addressing the problems associated with it.

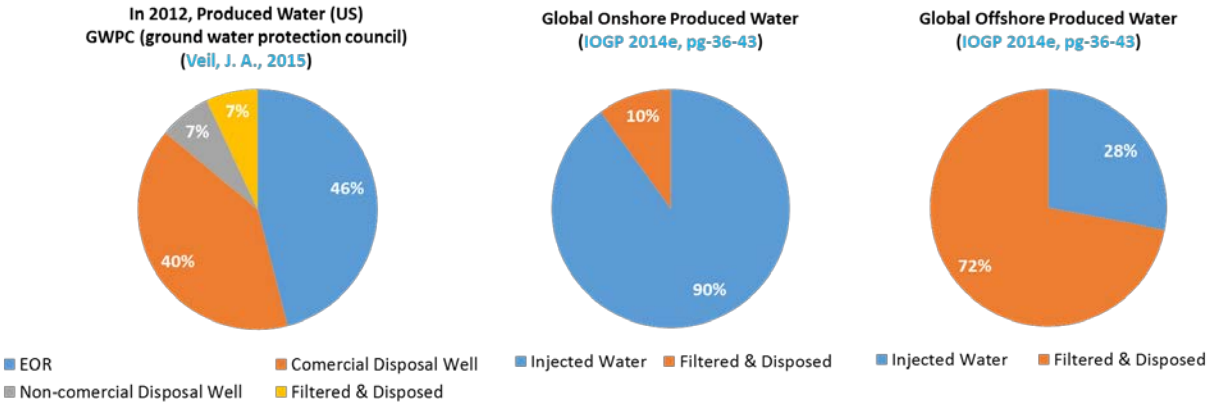

Figure 1-3: statistics of water production and injection in the United States and globally

[a] Please visit www.iogp.org/pubs/2014e.pdf for details and the list of participating companies in the IOPG 2014e report.

As water is injected into the formation, there exist several factors that affect the behaviour of the injection such as physical reservoir aspects (increase in flow resistance), quality of the injection water and degradation and/or chemically related reactions [9-12]. The main factor that contributes the most is the quality of the injection water which is discussed later in *section 2.2.4*. Globally, about 20% of water flooding operations have remained unable to meet their planned targets due to the mismatch between water quality and host reservoir [13]. This mismatch is caused by the induced formation damage from injection water that causes reduction in permeability. The reduction in permeability results in increased injection pressure, reduced injection rates and consequently more frequent stimulation operations which can become an economical nightmare if injectivity decline is not properly assessed beforehand [14, 15]. Despite decades of extensive research work, the understanding and prediction of injectivity decline as a result of formation damage cannot be considered complete and no unified approach exists [16, 17].

There are number of water quality issues that can contribute towards impaired injectivity of injection and disposal wells (*see section 2.2.4*). Most of the researchers have agreed that suspended particles are the main cause of the injection related problems [10, 11, 18-20]. Presence of tiny particles in the water is a well acknowledged fact. Most common names found for these particles in the literature are colloidal and suspended particles [21]. A distinction has been drawn between colloidal and suspended particles discussed later in *section 2.2.3*. The understanding of colloidal and suspended particle flow through porous media is of utmost importance to predict injectivity decline of a well and ensuring anticipated injection operations.

When water containing colloidal and/or suspended particles is injected into a porous media, these particles penetrate into the near wellbore vicinity and form internal filter cake and relatively bigger particles can get deposited over the injection face and form an external filter cake [11, 13, 14, 18, 20, 22-30]. The formation of internal and external filter cake is purely due to retention of particles which is influenced by several factors that are further discussed later in *section 2.2.7* These filter cakes can cause drastic reduction in well injectivity [5, 10, 14]. To avoid formation of internal and external filter cake and to comply with the environmental regulations, injection water is extensively treated and filtered prior to injection. Even then, there still exist dispersed particles in filtered injection water [2, 11, 13, 31]. Typical filtration practices such as primary and secondary filtration (discussed later in *section 2.2.2*), can remove dispersed particles down to ~2 microns. That means nano-sized particles are not filtered at all. With advancement in technology and availability of more comprehensive filtration techniques such as ultra-filtration, it is possible to filter dispersed particles down to nano-size. Hence, opens up a research topic to study injectivity decline induced by ultra-filtered water injection.

1.1 Research Objective

The objective of this study is to study the practical feasibility of ultra-filtration for water injection wells. Given the need to address the issues related to injectivity decline in ultra-

filtered water flooding, following sub research objectives are formulated to complement the main objective.

- Importance of stability of injection fluid for water injection.
- Quantification of injectivity decline induced by ultra-filtered water flooding.
- Investigation of the depth of penetration of dispersed particles in a porous medium.
- Qualitative interpretation of particle retention mechanisms taking place in ultra-filtered water flooding.
- Investigate the effect of variation in pH of injection fluid on injectivity decline in ultra-filtered water flooding.
- Investigate the effect of dispersed particle size in injection water on injectivity decline.
- Development of a numerical model to predict injectivity decline induced by ultra-filtered water flooding.

1.2 Approach

The study is carried out by adopting an experimental approach in a sequential manner to achieve the objectives of this study. Synthetic ultra-filtered water was prepared by adding nanoparticles in filtered demineralized water. Different brines were prepared by varying dissolved salt concentration, pH and dispersed nanoparticles in synthetic ultra-filtered water to study the stability of injection fluid. On basis of this, injection brine was selected. Core flood experimental setup was designed and built to perform water flood experiments in a precise manner. Three sets of experiments were performed. The first set of experiments included four core flood experiments to quantify injectivity decline, investigate the depth of penetration of nanoparticles and study the retention mechanisms. The second set of experiments composed of two core flood experiments that were carried out by varying pH of injection brine. The third set of experiment also consisted of two experiments that were carried out in unfavourable conditions i.e. presence of iron particles in injection fluid and fracture in the core plug. One of the experiments in that last set was unfortunately unsuccessful. Finally, a Matlab numerical model was developed to predict experimental results and was validated.

1.3 Outline of Thesis

The report consists of six chapters. Chapter 1 gives an overview of the motivation behind this study while also stating the objectives to be met. Chapter 2 contains a brief discussion of the relevant literature and covers theories to give the reader a brief idea of the work already done in this field and concepts involved. Chapter 3 describes the presented model formulation. Chapter 4 contains the experimental procedures and stability analysis carried out for injection brine. The results of the experimental investigation are presented and discussed in detail in Chapter 5. Finally, the conclusions drawn from the work done are presented in Chapter 6 and recommendations are listed in Chapter 7.

2 Theory

All geothermal power generation plants in the world operate on the principal of production and injection of water from underground geothermal formations [1]. In oil and gas industry, hydrocarbons are produced mostly with the help of water-flooding or aquifer support [32]. Where the aquifer potential is weak, water-flooding is adopted to provide pressure support and is most widely used for improved oil recovery (IOR) technique [33, 34]. For mature oil fields, water-flooding is considered as one of the economically viable techniques for recovery of additional oil [35]. During the production of hydrocarbons and later stages of the reservoir life, water production increases. This water is present either from the adjacent water bearing formations or was previously injected while water-flooding operations. The produced water either in the geothermal power generation or oil and gas upstream operations, needs to be injected into the underground formations for different purposes. Environmental regulations demand that the produced water must be thoroughly cleaned of impurities (solid and liquid particles) prior to injection into the subsurface. Even then, either water is injected into the reservoir for improving sweep, pressure support or in the subsurface for simple waste disposal, it frequently contains suspended fine particles. These particles during water injection get deposited over the injection formation face due to the formation of external filter cake (EFC) and into the near well bore vicinity due to internal filter cake (IFC) formation. This causes permeability reduction and formation damage that results in reduced injectivity of injection wells. Therefore, stimulation jobs are performed periodically after the injection commences to stimulate the impaired formation and increase the injectivity of the injection wells. The costs involved in treatment and filtration of injection water and stimulation jobs are appreciably high, especially offshore, therefore arises the need for understanding and predicting injectivity decline. Extensive time had been devoted to date in investigating the injectivity decline. In this chapter some of the previous works and prominent developed theories related to the scope of this research are presented.

2.1 Previous Works on Injectivity Decline

Considerable work has been done to predict the injectivity decline for injection and several analytical predictive models had been developed. Most of the models developed earlier looked into internal filtration and external filtration separately, neglecting the fact that both can take place simultaneously. Many attempts in the recent times have been made to capture both processes simultaneously. Many mechanisms are involved in this process with respect to properties of suspended particles, carrying fluid and rock. In this section a brief review of the prominent previous work is presented where the researchers have pointed out main mechanisms responsible for injectivity decline caused by particulate flow through porous media observed through experiments and presented different models to predict it.

Herzig [9] presented a comprehensive review of deep bed filtration and identified retention sites, retention forces along with the processes of clogging and de-clogging during suspended particle flow through porous media. Barkman & Davidson [18] proposed a measure of water quality ratio (i.e. ratio of the concentration of the suspended particles to the permeability of the filter cake formed by those particles) for an injection well and used it to predict the rate of impairment. They suggested that there are four mechanisms by which an injection well can be impaired by solids and that wellbore narrowing (EFC) is the predominant cause of impairment in injection wells. Donaldson & Baker [36] emphasized upon the particle size distribution. They observed that external filter-cake starts to build-up with relatively larger suspended particles and if an optimum particle size distribution is used, the particles will flow pass through the medium without getting trapped. This proposition was not appreciated by the works done later using suspended particles in the submicron ranges, as particles still got retained in the porous medium due to colloidal forces. Gruesbeck & Collins [12] studied abnormal decline in productivity of producing wells with particles being the naturally occurring fines (i.e. not injected but native particles). Their study focused on the flow rate variations and they observed that there exists a critical velocity of flow above which entrainment of retained particles becomes significant. They further reported that entrainment and re-deposition of fines is restricted to the near wellbore region. This finding was later questioned as damage radius would also depend on rock structure, rock composition and size and shape of fines that may vary from reservoir to reservoir. Todd [37] studied the depth of penetration of suspended particles and their effect on injectivity decline. Their results showed that when the suspension of <3 μm particles was injected, the damage was observed all through the core, no EFC was observed and that damage decreased with depth. When the suspension of 4-6 μm was injected, similar results were obtained. When the suspension of 8-10 μm was injected, 90% of the damage was observed near the injection face and EFC was formed. They concluded that the prediction of permeability loss is clearly more complicated than the simple geometrical applications of pore size to particle size ratio rules as proposed by Abrams [22] (i.e. if ratio of mean particle size diameter to mean pore size diameter is less than 1/3 than predicted filter cake would be EFC whereas if ratio is more than 1/7 then no damage would take place and if the ratio is in between 1/3-1/7 then IFC would form). Vetter [38] studied the importance of particle charges by using submicron sized (<2 μm) suspended particles. They attributed electrical interactions between particles and grains as the main contributing factor of formation damage in the submicron sized particulate flow. Eylander [23] studied irreversible and reversible formation damage by suspension injection and clean brine forward/back-flush tests. He observed that EFC is reversible whereas IFC is not completely reversible. The permeability gained after the back-flush experiment was attributed to breaking of particle bridges. He observed that both external and internal filtration can take place simultaneously. Khatib [24] studied the properties of EFC by using different suspended particles and observed that for a given porosity of the external filter-cake, permeability varies for different particle types. She attributed this to the difference in particle size and compressible nature of particles. All recent studies have also experienced similar mechanisms in terms of particle retention but they have found that multiple retention mechanisms may take place simultaneously. Apart from the usual experimental procedures available in the literature, in

recent studies more efficient experimental techniques to study retention mechanisms of particles have been developed. Bedrikovetsky [20] shed light on the importance of an additional intermediary point on the core plug for pressure measurement in injectivity decline experiments. R. Farajzadeh [29], Al-Abduwani [30] and Yerramilli [39] showed that computed tomography (CT) scanning can be used to quantify and map local retained-particle concentrations with exceptional spatial and temporal resolutions. Al-Abduwani also proposed the post-mortem approach for quantification of deposition profiles from image and chemical analysis, which is a destructive method as core sample has to be broken into different small segments. These methods of visualizing the retained particles can be useful to understand the amount and type of retention taking place in dilute suspension flow through porous media.

In terms of modelling, there are many models in the literature to predict injectivity decline due to IFC and EFC but most of them seem a little unrealistic in many cases as they predict unlimited growth of retained particle concentration. Gruesbeck & Collins [12] proposed a model for deep bed filtration that also considers entrainment of retained particles. This was later modified by Wang & Civan [40] and further modified version of this model has also been used by Yi [28], Broek [41] and Eclipse Reservoir Simulation software [42] where it is used to predict formation damage due to asphaltene deposition. This model takes into account three main depositional mechanisms i.e. adsorption, plugging and entrainment and predicts injectivity decline due to deep bed filtration. The presence of entrainment term helps in limiting the growth of retained particle concentration. Nonetheless, the selection of a model to predict injectivity decline entirely depends upon the retention mechanisms taking place and therefore a thorough understanding of particulate flow through porous media is necessary for modelling.

2.2 Theoretical Background

In this section, main theories and concepts related to water injection are presented. As mentioned earlier, it is widely reported that injection operations always encounter injectivity decline. There are different injection schemes through which water is injected into the reservoir.

2.2.1 Water Injection Schemes

There are mainly four types of water injection schemes through which water is injected into the reservoir given below;

- Fresh-Water Injection (FWI): Fresh water either from shallow water aquifers or natural waters is injected into the reservoir (on-shore operations).
- Sea-Water Injection (SWI): Seawater is injected into the reservoir (off-shore operations).
- Produced-Water Injection (PWI): water produced while hydrocarbon production is injected into subsurface after separating it from hydrocarbons.

- Produced-Water Re-Injection (PWRI): Water produced while production of hydrocarbons is injected into the same reservoir and is produced again and injected back. This could be considered a closed loop operation.

In all the aforementioned schemes, water being injected is extensively treated and filtered prior to injection. Before discussing issues associated with treated and filtered water injection it is important to shed some light on the difference between current filtration practices and ultra-filtration that is the objective of this study.

2.2.2 Injection Water Filtration Practices

Injection water is always treated and filtered before injection. Typical filtration practices for injection wells use micro-filtration plant that is a combination of primary and secondary filtration. After micro-filtration of injected water, dispersed solids remaining in the water are between 10µm to 0.45µm. With advancement in technology and availability of more comprehensive filtration techniques such as ultra-filtration, it is possible to filter dispersed solids down to nano-size. With ultrafiltration of injection water, dispersed solids remaining in the water are between 0.45µm to 10nm. Therefore, in this study, nanoparticles are added into the filtered water to mimic synthetic ultra-filtered water.

Most common names found in the literature for solids dispersed in water are colloidal and suspended particles [21]. Here, it deems necessary to understand the difference between colloidal and suspended particles.

2.2.3 Classification of Particles in Injection Water

Distinction has been drawn between colloidal and suspended particles generally with colloidal being the ones having the biggest dimension with a size smaller than 1µm whereas suspended particles are those where the biggest dimension has a size greater than 1µm. A mixture prepared by using suspended particles is called suspension whereas mixture prepared with colloidal particles is called colloid. This distinction is justified based on the properties of colloids and suspensions. Colloidal particles are mostly invisible with say 0.5µm wavelength of ordinary light whereas suspended particles can easily be observed by naked eye. *Figure 2-1* shows a simple illustration of colloid and suspension in presence of light.

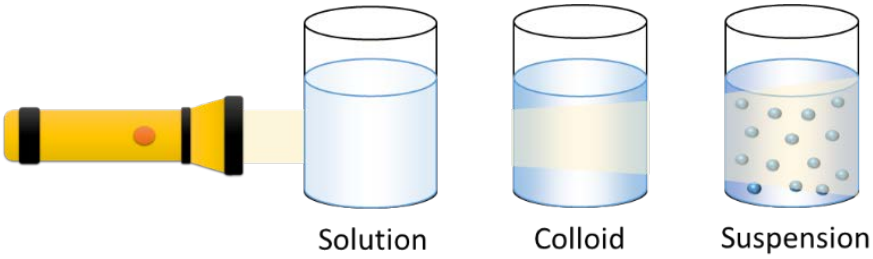

Figure 2-1: Classification of colloid and suspension

Another attribute differentiating between colloidal and suspended particles is the sedimentation rate. Sedimentation rate of suspended particles is significantly higher than colloidal particles which tend to stay in dispersed state for longer times. Below particle size of 1µm, surface effects such as adsorption begin to predominate and as particle size

decreases, colloidal interactions become increasingly significant relative to external forces (gravitational and hydrodynamic effects). Hence, it is convenient to say 1µm as a dividing line [43]. In natural waters an operational distinction has been made between suspended and colloidal particles, if the particles get retained at a membrane filter of 0.45µm then they are suspended particles otherwise they are classified as colloidal particles [43, 44]. This operational distinction is commonly referred to as total suspended solid (TSS) limit. In this study, nanoparticles are used which lie into colloidal particle category. Henceforth term 'particle' will be used throughout to refer to colloidal particles.

As mentioned earlier water quality of injection fluid is termed as one of the core components for injectivity decline [9-11, 13] hence it is important to understand what water quality is.

2.2.4 Water Quality

Water quality is based on composition of injection water. For evaluation purposes, water quality can be subdivided into seven categories i.e. ionic composition, chemical contaminants, suspended solids, scale and precipitate potential, hydrocarbon content, non-condensable gas content and bacterial content [2, 45]. Water quality greatly impacts rock and fluid interaction. Hence good water quality is that which does not result in damaging the rock. Water quality of injection fluid cannot be kept same for every injection operation as different minerals in reservoir rock could react differently to injected water e.g. water quality for high clay content formations would be different from less clay content formations.

In this study, we will assume that water is free of most impurities mentioned above and water quality is only defined by dispersed solid particles, dissolved salt concentration and pH. Salt concentration and pH of injection water could determine whether in-situ fines will be released from a potential source in the reservoir and also the likelihood of already dispersed solids to aggregate. This depends on the forces between the surface of the dispersed solids and reservoir grains. These inter-surface forces are subject to the DLVO theory that is sum of London van der Waals attraction, double layer attraction or repulsion and short range forces (*see section 2.2.4.3*). Changes in pH of the injection water can alter double layer potential energy and therefore a key element in promoting fines in reservoir and aggregation of dispersed solids. Ionic strength and dispersed solid size can also effect inter surface forces [21, 43, 46, 47].

2.2.4.1 Influence of Salt Concentration

In terms of in-situ fine mobilization, when salt concentration of injection fluid exceeds a critical value, clay minerals present in the reservoir would swell. Swelling of clays results in increase in attractive forces between clay particles as their double layer is compressed due to part of the cations moves from the diffuse layer to the stern layer and consequently the zeta-potential (*see section 2.2.4.5*) decreases. This causes aggregation or bridging of clay particles to form bigger particles. Fines attached to swelling clays may also dislodge and liberate during swelling of clays. The amount of swelling depends on the type of clay for example, montmorillonite (smectite group) swells more than illite or kaolinite (kaolin group). In terms of dispersed particles, salt concentration influences the double layer thickness and the stability of colloid [16, 21, 48-50].

2.2.4.2 Influence of pH

pH effects stability of colloid as electric double layer of particles is altered by variation in pH which could result in increasing or decreasing zeta-potential. Reduction in the magnitude of zeta-potential value reduces the repulsive forces between particles which results in the formation of aggregates. pH could also influence the release of fines by clay dispersal and by dissolution of cementing agents such as oxide minerals and calcites. As pH increases, the tendency of losing protons increases resulting in more negatively charged oxide surface. There is a characteristic pH value where the surface has no apparent charge and is called point of zero charge (PZC) [16, 43, 51]. It is repeatedly reported in the literature that if injection water's pH is high i.e. >9, then permeability reduction is experienced even in sandstones with little clay content [46, 52].

2.2.4.3 DLVO Theory

When two similarly charged particles approach each other in an electrolyte solution then there exists repulsive force between them due to the overlap of their diffuse electric double layer. But in the same time, there exists an attractive force between molecules that is known as London van der Waals forces. Together these forces give basis of the DLVO theory of colloidal stability which was developed independently by Derjaguin & Landau, 1941 and Verwey & Overbeek, 1948. Sum of repulsive and attractive potentials curves give a net potential curve. If the net potential curve is repulsive then the highest value on this curve is called energy barrier. If the kinetic energy of particles on a collision course increases the energy barrier then they agglomerate.

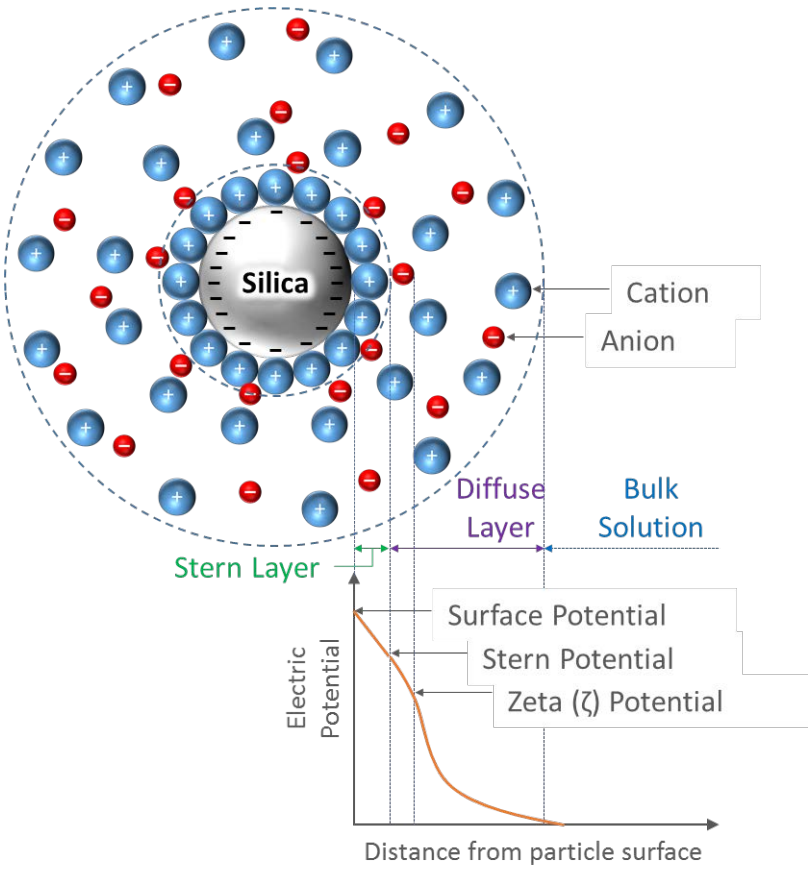

Figure 2-2: Depiction of double layer & zeta potential location

2.2.4.4 Electric Double Layer

When a particle is dispersed in electrolyte, some of the counter-ions are electrostatically attracted close to the particle's surface and the rest remain randomly diffused throughout the solution. Negatively charged particle initially repels co-ions (anions) and attracts its counter-ions (cations) which form a firm layer around the surface of the particle. This layer is known as Stern layer. Other counter-ions are still attracted by the particle but due to the formation of Stern layer, these counter-ions are repelled at the same time too. This results in formation of Diffuse layer of counter-ions. The concentration of counter-ions reduces whereas concentration of co-ions increases further away from the particle, till it reaches equilibrium with solution's concentration. The surface charge on a particle and associated counter-ion charge in stern and diffuse layer altogether form an electric double layer [16, 43, 51]. A simple illustration of electric double layer around a particle is shown in *Figure 2-2*.

2.2.4.5 Zeta Potential (ζ)

Most widely used experimental technique to study the surface charge is through electro-kinetic techniques. Whenever there is a relative movement between a charged particle and electrolyte solution, part of double layer charge moves with the liquid. Here the concept of plane of shear comes into play which distinguishes between the fixed and mobile parts of electric double layer. The electrical potential at shear plane is known as electro-kinetic potential or zeta potential (ζ). Shear plane is known to lie outside but fairly close to stern plane indicating all of diffuse layer is mobile whereas counter-ions in stern layer are fixed. This highlights the fact that value of zeta potential is less than true surface charge but as there exists clear correlation between zeta potential and colloidal stability, this value is widely used [16, 43, 51]. Distance from particle surface at which zeta-potential is measured is depicted in *Figure 2-2*.

2.2.4.6 Electrophoretic Mobility

The device used in this study to measure zeta potential is Malvern Zetasizer Nano-ZS. This device uses the concept of electrophoresis where the charged particle moves relative to liquid under the influence of an applied electrical field. Charged particles in the solution are attracted towards the electrode of opposite charge. Viscous forces acting on the particles oppose this movement but when equilibrium is reached between these two forces, the particle moves with constant velocity. This velocity is commonly known as electrophoretic mobility and is related to the zeta potential of the particle, viscosity and dielectric constant of the liquid by Henry's equation shown in the equation below.

$$U_E = \frac{2\varepsilon\zeta f(Ka)}{3\mu}$$

U_E is the electrophoretic mobility, ε is the dielectric constant, $f(Ka)$ is Henry's function The device uses a technique of Laser Doppler Velocimetry (LDV) combined with Phase Analysis Light Scattering (PALS) to measure the electrophoretic mobility which is then converted to zeta potential using theoretical considerations. Detailed description of operational techniques for LDV and PALS can be found elsewhere in Malvern zetasizer nano-ZS operational manual.

As described in previous sections, particles may be introduced through injection water or may be mobilized in-situ due to incompatible injected fluid. Once particles migrating with the carrier fluid are introduced into a porous medium, they get retained.

2.2.5 Retention Sites

Retention of particles takes place at different sites available in the porous medium that are listed below [9, 11, 29] and illustrated in *Figure 2-3*.

- Surface sites: surface of grains forming a porous medium
- Constriction sites: when space between grains are smaller than the size of particle
- Crevice sites: cleft or convex formed between multiple grains
- Cavern sites: sheltered area or small pockets formed by grains that are not disturbed by flow streams

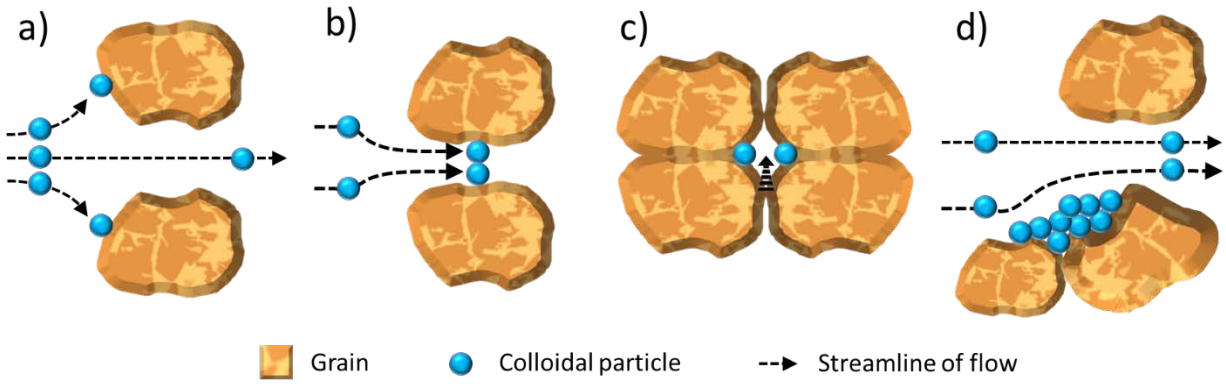

Figure 2-3: Retention sites in porous media a) Surface sites, b) Constriction sites, c) Crevice sites and d) Cavern sites

2.2.6 Retention Forces

The forces that influence retention are [9, 16];

- Axial pressure of fluid: Fluid pressure may hold a particle against an opening if the particle size is bigger than the pore throat.
- Frictional forces: Shape or surface of the particle lodged in a crevice may have been slightly deformed due to impact or sliding and might get retained there due to friction.
- Surface forces: These include Van der Waal's forces and electro-static or electro-kinetic forces that are either attractive or repulsive based on the physio chemical conditions of the colloid.
- Chemical forces: Based on the composition of the injected fluid and porous medium, actual chemical bonding may take place and the particles get retained.

2.2.7 Retention Mechanisms

Retention mechanisms involved in capture process of the particles flowing with the injected fluid through porous medium are described by the following fundamental colloids retention mechanisms [9, 10, 12, 25, 38]. These retention mechanisms are described looking at a single particle and a single collector (grain).

- Sedimentation: If there exists density difference between the particle and the carrier fluid then sedimentation would take place.
- Inertial Impaction: As the porous medium is mostly torturous in nature, therefore, streamlines of the fluid flow change suddenly and a particle owing to its apparent weight tend to deviate from the streamline of flow and get in contact with the porous medium grains.
- Interception: Particle following the stream line of flow hits a grain and gets retained.
- Dispersion/Diffusion: Particle might diffuse due to Brownian motion or disperse indirectly due to diffusion and reach areas that are not normally populated by them and get retained at a grain there.
- Electrostatic Deposition: Due to the difference in surface charge of the particle and rock, there would exist attraction or repulsion force. Van der Waals attraction and double layer repulsion are significant forces responsible for this type of retention mechanism.

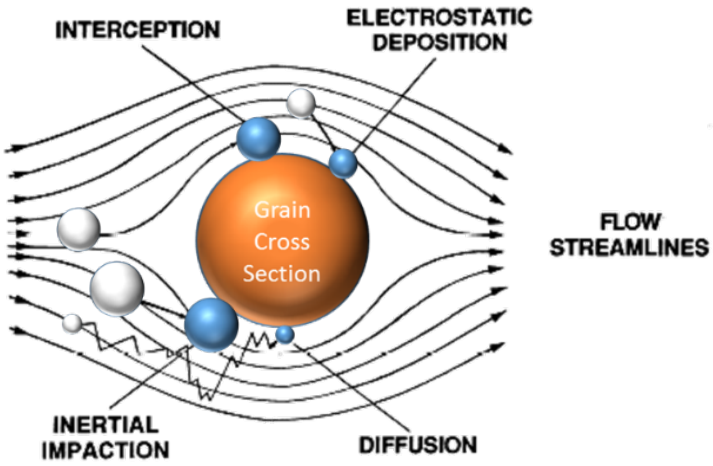

Figure 2-4: Illustration of particle retention mechanisms in porous medium

Looking at multiple collectors, three main retention mechanism can be characterised i.e. surface deposition, plugging and entrainment. All these three retention mechanisms take place due to above described capture processes [9, 10, 12, 16, 38].

2.2.7.1 Surface Deposition

When particles get deposited at the surface of the grains of porous media, it is termed as surface deposition or adsorption. *Figure 2-5* shows surface deposition of particles in porous medium.

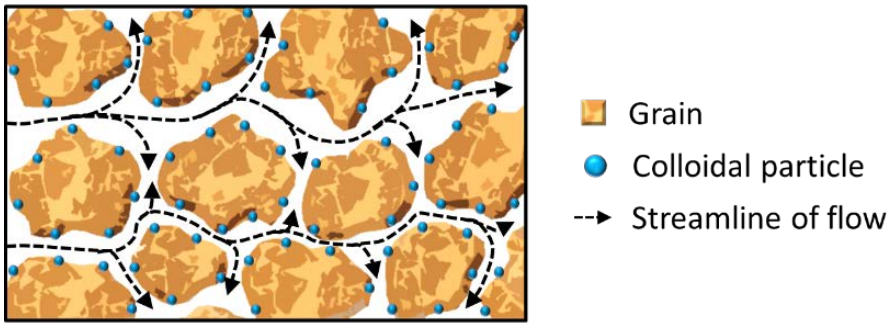

Figure 2-5: Surface deposition of particles in porous medium

2.2.7.2 Plugging

If a single particle or collection of particles approach a pore throat smaller than their size at the same time then plugging would take place. Plugging with single particle is known as mono-particle plugging whereas with multiple particles it is termed as multi-particle plugging. Particles or fines dispersed in-situ can also form a bridge at pore throats in presence of salt over time. This type of plugging is called bridging. Plugging can lead to pore filling which can have severe impacts on permeability reduction of porous medium. Illustrates bridging, multi–particle and mono-particle plugging in porous media.

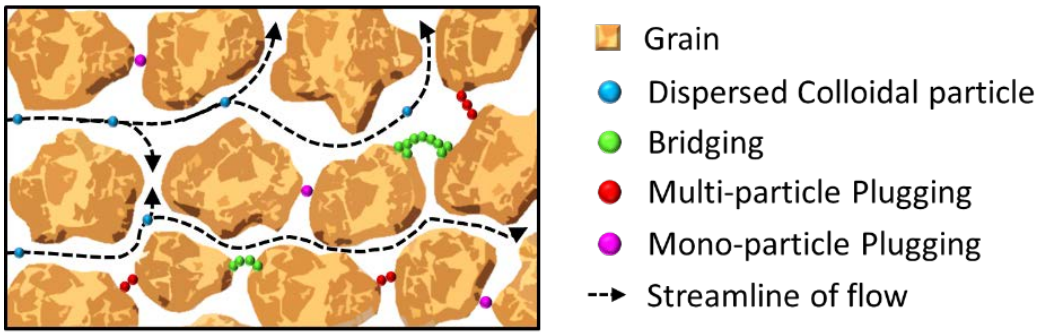

Figure 2-6: Illustration of bridging, multi –particle and mono-particle plugging in porous media

2.2.7.3 Entrainment

Entrainment takes place when a deposited or plugged particle gets detached and is entrained by the flow into porous medium. Due to bridging and plugging of the pore throats, local variations in the flow rate and pressure may occur in the vicinity of the retained particles and/or if a moving particle hits a retained particle at high interstitial velocity, then the retained particle may get detached.

2.2.8 Internal Filter Cake

Retention mechanisms described earlier make a porous medium to act as a filter when colloid is injected into it. Suspended or colloidal particles getting retained inside a porous medium is known as internal filter cake or deep bed filtration.

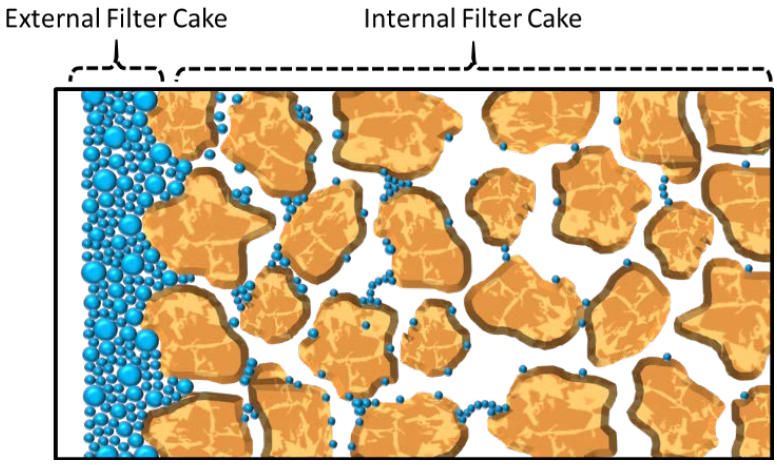

Figure 2-7: External and Internal filter cake

2.2.9 External Filter Cake

External filter cake is the term used to describe the suspended and colloidal particles retained at the interface of a porous medium due to straining or size exclusion. External filter cake may be consolidated by the effect of fluid pressure as colloid flows through the cake.

Based on the retention mechanisms mentioned earlier, impact of each retention mechanism was studied based on their collision probability with varying particle size, shown in *Figure 2-8*. The plot is obtained based on the equations given by Herzig [9]and Civan [11, 16].

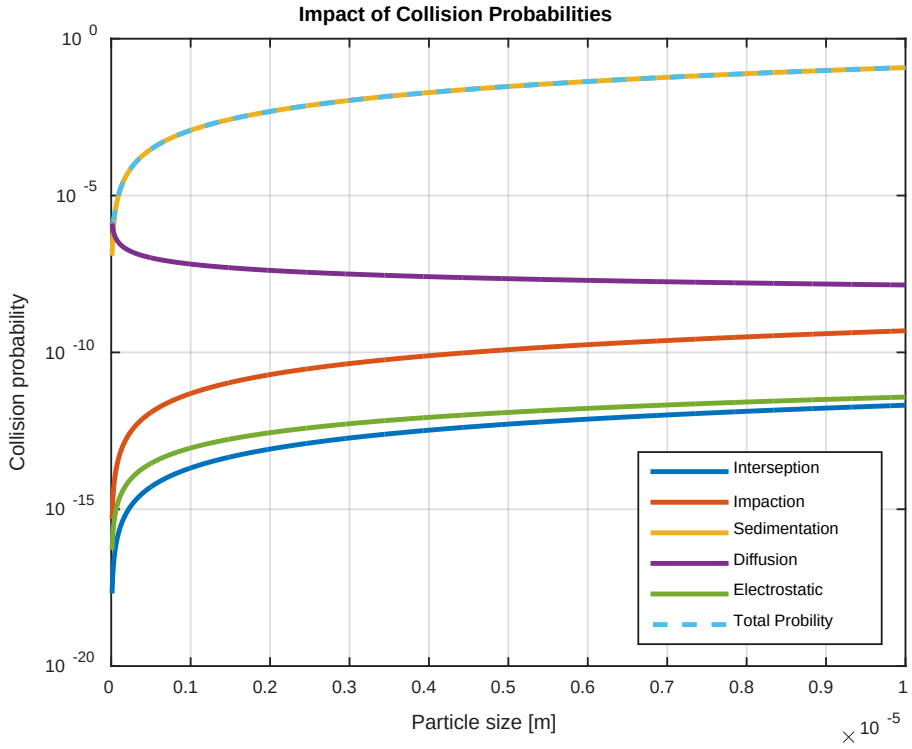

Figure 2-8: Impact of different capture processes on varying particle size

Probability of all the capture processes increases with the increase in particle size except for diffusion or dispersion which on the contrary has higher impact for particles less than 1µm. Based on this information, hydrodynamic dispersion is considered in model formulation.

3 Model Formulation

3.1 DBF Model Formulation

To cater the objective of this study, model for deep bed filtration was developed for ultrafiltration (dispersed nanoparticles in injected fluid). To have an idea of the system under investigation, consider a porous medium that is well consolidated sandstone, known composition, homogeneous and isotropic of porosity φ, initial permeability k_0, mean pore throat diameter d_{pt}, rock density ρ_s, length L and cross sectional area A. The porous medium in fully saturated with brine of known composition, pH, salinity and viscosity μ_b. There exist only single phase and no impurities in the medium. A dilute concentration c of mono dispersed particles that are likely charged are dispersed in same brine that saturated the porous medium. This colloid is injected into the porous medium with constant superficial velocity u. Particles flow into the medium and because of retention mechanism mentioned earlier, start to get retained forming internal filter cake. At this point, it is important to realize the difference between colloidal size and pore size distributions (*see section 5.4.1*). As particles are smaller than the average pore throat diameter of the porous medium hence, one can argue that plugging of colloids is unlikely to take place in general. But as found in literature that even particles may get retained in micro-pores or could plug porous media due to formation of colloidal bridges in the pore throats. Electrostatic retention mechanism dominates in colloidal flow in porous medium that results in adsorption of colloids on grain surface. As time progresses, the retention sites available for the colloids to get trapped starts to decrease until a stage reaches where no more retention of colloids take place. Due to retention of particles, permeability of the porous medium is decreased which results in injectivity decline.

3.1.1 Assumptions

The assumptions taken for the model of deep bed filtration with colloidal flow are

- Simplifying for lab core flood experiments one dimensional model is considered.
- Model assumes single phase fluid flow assuming near well bore of water injection well fluid system that is fully saturated with water after short period of water injection.
- Pore space is that space where there is mobile water that means dead end pores, where the water is trapped, as part of the pore space is not counted.
- Fluid, colloids and rock are incompressible.
- Colloidal suspension is injected at constant superficial velocity.
- Density of colloids is constant in deposited and suspended state.

- Porosity is changing due to retention of colloids and hence porosity and interstitial velocity would vary over time and space.
- Dispersion and the dependence of viscosity on the colloidal concentration were taken into consideration even though both are too small.
- Once the colloids are deposited in the porous medium they can be released and entrained further into porous medium.

3.1.2 Governing Equations

The governing equation for the deep bed filtration model under investigation originates from mass conservation equation and retention kinetics [9, 11, 12, 16, 53, 54].

3.1.2.1 Mass Conservation Equation

Transport equation describing spatial and temporal variation of particle concentration in a porous medium undergoing and advection dispersion is derived based on the assumptions mentioned earlier (*see Appendix A*) and is given by

$$-D\varphi\frac{\partial^2 c}{\partial x^2}+u\frac{\partial c}{\partial x}+\frac{\partial \varphi c}{\partial t}+\frac{\partial \sigma}{\partial t}=0 \tag{1}$$

Where c is the suspended colloidal concentration, φ is the porosity of the porous medium, σ is the retained colloidal concentration and D is the hydrodynamic dispersion coefficient.

3.1.2.2 Hydrodynamic Dispersion

Hydrodynamic dispersion results from both molecular diffusion and mechanical dispersion of colloids in fluid flow. The equation for hydrodynamic dispersion is given by van Genuchten, 1986 [55] as

$$D=D_0\tau+a_L v^n \tag{2}$$

Where D_0 is the molecular diffusion coefficient, τ is the tortuosity of the porous medium, a_L is the longitudinal dispersivity, v is the interstitial velocity and n is an exponent. Sorbie, 1991 found the values for longitudinal dispersivity and exponent for quartz gravel to be 0.2 and 1.083 respectively [39, 56]. As the Peclet number based on parameters of the experiments conducted in this study are in the order of 10^6, mechanical dispersion dominates and molecular diffusion term is negligible.

3.1.2.3 Retention Kinetics

Most deep bed filtration models use the kinetic equation given by [9] for basis of retention kinetics which shows that deposition rate is proportional to the superficial velocity and concentration of suspended particles and is given as

$$\frac{\partial \sigma}{\partial t}=\lambda u c \tag{3}$$

Where λ is the filtration coefficient. In different studies, different formulation for filtration coefficient are used. Gruesbeck and Collins, 1982 concluded that retention rate depends on

adsorption, plugging and entrainment of particles [12]. Their formulation was modified partially by Wang and Civan, 2005 [53] by introducing retention rate coefficients (adopted in this study with sight modification on plugging coefficient condition based on Schlumberger Eclipse reference manual [28, 41, 42]) which is given as

$$\frac{\partial \sigma}{\partial t} = \alpha \varphi c + \lambda u c - \psi(|v| - v_{cr})^{+} \sigma \tag{4}$$

In the change of retention function, first term caters for retention taking place due to surface deposition, second term accounts for plugging and the third term is responsible for the entrainment of the particles. In the first term of equation 4, α is the surface deposition coefficient. The adsorption rate of particles show direct proportionality between retention rate and concentration of particles in dispersed state and the fraction of volume available. This means, due to adsorption, the effective porosity would reduce and hence retention concentration would increase. A time would come when some of the pore throats would become small enough for plugging to take place.

In the second term, λ is the plugging coefficient which is proportional to superficial velocity and suspended colloidal concentration and is given by

$$\lambda = \begin{cases} \lambda\ , & \sigma > \sigma_{cr} \\ 0\ , & otherwise \end{cases} \tag{5}$$

This means that plugging will only occur if the retained colloids concentration σ gets bigger than some critical retained colloids concentration σ_{cr}. This means, due to adsorption, retained colloid concentration at some stage would result in reducing the flow path to an extent where suspended colloids could get directly plugged.

In the third term of equation 4, ψ represents entrainment coefficient of retained particles by flowing phase when the interstitial velocity v becomes larger than some critical interstitial velocity v_{cr}. This term shows direct proportionality of retention rate to the retained particle concentration and the difference between the interstitial and some critical interstitial velocity necessary for retained particle's mobilization which is given by

$$\psi = \begin{cases} \psi\ , & |v| > v_{cr} \\ 0\ , & otherwise \end{cases} \tag{6}$$

This means, due to adsorption and plugging, a stage would come when the interstitial velocity variations would become large enough to release the retained colloids. The interstitial velocity would change with change in porosity due to retention of particles in the porous media.

3.1.2.4 Porosity Reduction Model

As the deposition takes place in the pore space, local porosity changes which is equal to the difference between the initial porosity and the fractional pore volume occupied by the retained colloidal concentration [16, 28, 41]

$$\varphi(\sigma) = \varphi_0 - \int_0^t \frac{\partial \sigma}{\partial t} dt \tag{7}$$

Change in local porosity would result in change in interstitial velocity. This velocity is hence updated based on Darcy's velocity definition that is given as

$$v = \frac{u}{\varphi_0 - \sigma} \tag{8}$$

3.1.2.5 Permeability Reduction Model

Permeability of the porous medium is reduced due to retention of particles therefore, permeability reduction is related to retained particle concentration as

$$k(\sigma) = \frac{k_0}{1 + \beta\sigma} \tag{9}$$

Where $k(\sigma)$ is the permeability reduction function, k_0 is the initial absolute permeability of the porous medium and β is the empirical parameter commonly known as formation damage factor. There are other permeability damage models in the literature but above described model is used for simplicity.

3.1.2.6 Injectivity Decline

Quality of injection is normally given by the non-dimensional normalized injectivity index II. Injectivity is defined as the ratio of volumetric injection flowrate to the pressure difference. Normalized injectivity index is then the ratio between the initial and current injectivity indexes which is equal to normalized permeability if flow rate and viscosity are kept constant i.e. in this study.

$$II = \frac{II_t}{II_0} = \frac{q_t \Delta P_0}{q_0 \Delta P_t} = \frac{k_t}{k_0} \tag{10}$$

Pressure gradient is related to permeability of the porous medium through Darcy's law

$$u = -\frac{k(\sigma)}{\mu_s} \Delta P \tag{11}$$

Where μ_s is the viscosity of the colloid. Einstein's equation for viscosity relates it to the viscosity of the carrier fluid by

$$\mu_s = \mu_b(1 + 2.5c) \tag{12}$$

Where μ_b is the viscosity of the carrier fluid (brine).

3.1.3 Initial and Boundary Conditions

Considering core flood experiments, at initial state the core plug is free of dispersed and retained colloidal concentration hence the initial condition given in equation-13. The

injection face of the core is supplied by constant inlet colloidal flux that results in Robin boundary condition (equation-14) which after discretization becomes simply $c(0,t) = c_{inj}$ (*see Appendix A*). At the end of the core plug, there is no change in concentration hence Neumann boundary condition (equation-14).

3.1.3.1 Initial Conditions:

$$c(x, t = 0) = 0 \quad and \quad \sigma(x, t = 0) = 0 \tag{13}$$

3.1.3.2 Boundary Conditions:

$$uc_{inj}(0,t) = uc - D\varphi \frac{\partial c}{\partial x} \quad \Rightarrow \quad c(0,t) = c_{inj}$$
$$\frac{\partial c}{\partial x}(L,t) = 0 \tag{14}$$

The presented model describes deep bed filtration process for particle flow through a porous medium. The governing equation is solved numerically using Finite Difference method in space and Euler Forward in time. The discretization is presented in *Appendix A*.

4 Experimental Methods

Eight core flood experiments were conducted using silica nanoparticles at different concentrations and flow rates to understand the formation damage mechanism during the flow of nanoparticles through sandstone rock at core scale. Bentheimer sandstone was characterized by performing X-ray diffraction/X-ray fluorescence (XRD/XRF) for determining the composition and Mercury Intrusion Porosimetry (MIP) test was performed to obtain porosity and pore size distribution (PSD). For permeability, absolute permeability tests were conducted using filtered brine prior to every experiment for each core plug. Before the selection of brine, the stability of nanoparticles in different brines was studied. While dealing with nanoparticles, it is extremely important to study their stability in a brine prior to injecting them into the rock to ensure particles do not aggregate beforehand resulting in an apparent increase in particle size. For this, several samples were prepared by varying brine properties and silica nanoparticle concentration. Particle size distribution and zeta potential measurements were taken for these samples. To ensure minimum adsorption of particles on the rock due to electrostatic forces, zeta potential measurements were also taken for rock in brine mixture but the results obtained were not reliable due to a variety of components in the sandstone having different surface charges and also due to unstable suspension in which sand grains tend to settle down. In this section, results obtained for initial analysis on brine, nanoparticles and rock are presented along with core flood experimental setup, procedure and post-experiment analysis techniques.

4.1 Porous Medium

Bentheimer sandstone outcrop sample was selected as a porous medium. These rocks have good lateral continuity and exhibit block scale homogeneous nature. This sandstone block comes from the Romberg quarry in Gildehaus, Germany. It is an Aeolian deposit rock that shows constant mineralogy and is largely free of paramagnetic impurities, well consolidated and has well-sorted grain framework and pore network [57].

4.1.1 Rock Composition

The modal composition of the Bentheimer sandstone was obtained from X-ray diffraction/X-ray Fluorescence (XRD/XRF). It is composed of >90 % quartz, <3 % clay and <5 % feldspar with some traces of carbonate and oxide minerals. Results obtained in this study along with some of the XRD/XRF results taken from the literature for Bentheimer sandstone from Gildehaus are presented below in *Table 4-1*.

Study	Quartz	Clay	Feldspar	Other	Sum
	[wt %]	*[wt %]*	*[wt %]*	*[wt %]*	
This study	**92.0**	**2.80**	**4.50**	**0.70**	**100**
A.E. Peksa et al. (2015)	91.7	2.68	4.86	0.76	100
Maloney et al. (1990)	97.5	0.50	2.00	Traces	100
Van Baaren et al. (1990)	95.0	3.00	2.00	-	100

Table 4-1: XRD results of Bentheimer sandstone from literature

4.1.2 Rock Porosity and Pore Size Distribution (PSD)

Mercury Intrusion Porosimetry (MIP) on a rock sample taken from the same block of core plugs was performed to find the porosity and pore size distribution. *Figure 4-1* shows the pore size distribution of Bentheimer sandstone obtained from MIP test. The procedure of MIP can be found in *Appendix B*. Comparison of pore diameter and porosity results obtained from this study with data from the literature shows that all data display the similar result (see *Table 4-2*).

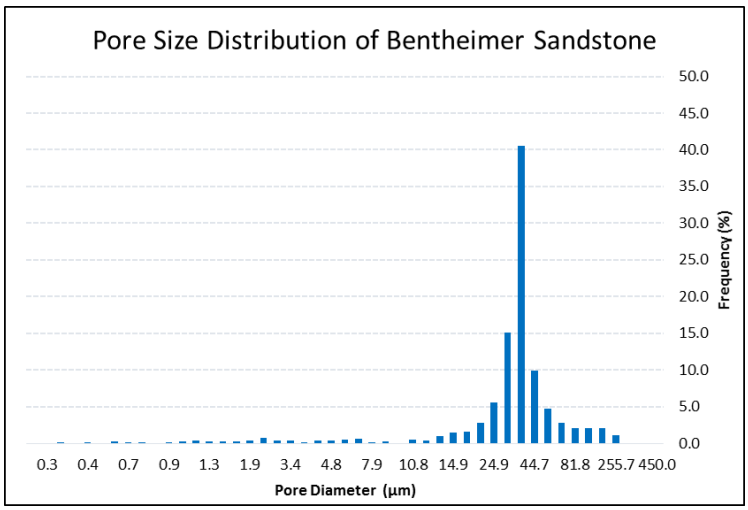

Figure 4-1: Pore size distribution of Bentheimer sandstone

Study	Pore Size	Porosity		
	Avg. Pore diameter [mm]	*Avg. from MIP*	*Avg. from imaging methods*[b]	*Avg. from laboratory methods*[c]
This study	**0.013**	**0.234**	**-**	**-**
A.E. Peksa et al. (2015)	0.014	-	0.254	0.248
Halisch (2013a)	-	0.215	-	-
Dautriat et al. (2009)	-	0.240	-	**-**
Klov (2000)	-	0.220	0.215	**-**

Table 4-2: Porosity and pore diameter results from this study and literature

4.1.3 Rock Permeability

Permeability was obtained by performing absolute permeability tests for each core plug. Brine was injected into a core plug at different flow rates and the pressure difference across

[b] Average from imaging methods contains results from Image Analysis, Micro and Medical CT Scanning.
[c] Average from laboratory methods contains results from Ultra Pycnometer and Gravimetric methods.

the core plug was recorded. Using Darcy's equation permeability was calculated. The plot of flow rate to area $\frac{Q}{A}$ versus pressure difference per length $\frac{\Delta P}{L}$ was generated for each test. For Darcy's flow, data follows a straight line with a slope of $\frac{k}{\mu}$. At high flow rates, turbulent flow is indicated by a deviation from the straight line but in all the tests, those high rates were never achieved. Permeability obtained for all core plugs is shown in *Table 4-3*.

Experiment No.	Length *[cm]*	X-sec. area *[cm^2]*	Slope (k/μ) *[Darcy/cP]*	Regression Coefficient	Permeability *[Darcy]*
CF-1	17.05 ± 0.01	11.64	3.1315	0.9998	2.85 ± 0.15
CF-2	17.00 ± 0.01	11.34	3.0257	0.9994	2.71 ± 0.10
CF-3	16.95 ± 0.01	11.61	3.3514	1.0000	3.05 ± 0.10
CF-4	16.95 ± 0.01	11.61	3.6296	1.0000	3.30 ± 0.10
CF-5	17.00 ± 0.01	11.61	3.2042	1.0000	2.92 ± 0.10
CF-6	17.00 ± 0.01	11.61	3.3830	1.0000	3.08 ± 0.10
CF-7	10.54 ± 0.01	11.64	3.5656	0.9998	3.24± 0.23
CF-8	17.01 ± 0.01	11.34	2.9364	0.9982	2.74 ± 0.11

Table 4-3: Absolute permeability for Bentheimer core plugs for all experiments

4.1.4 Core Plug Preparation

Cylindrical cores were drilled out of a Bentheimer sandstone's large cubical block of arbitrary diameter and then sawn to desired dimensions with an accuracy of ± 1mm with the help of water-cooled diamond saw. These cores were then dried in an oven at a temperature of 60°C for 48 hours to remove water content and moisture. Afterwards, they were placed in the molds and coated with self-hardening glue (Araldite CW2215 with a hardener HY5160). This is done to preserve the core and to ensure that when the core plug is placed in the core holder, the O-rings can be placed properly on glue to make the annular space between the core and core holder completely independent from the inlet. After hardening of the glue, excess glue is machined so that the core plug fits in the core holder precisely. For the intermediate pressure data along the core, three holes were drilled in the core as shown in *Figure 4-2*. These holes were drilled at 21mm, 53mm and 85mm respectively from the injection face. After this, the core plugs were dried once again an oven for 24 hours at a temperature of 30°C.

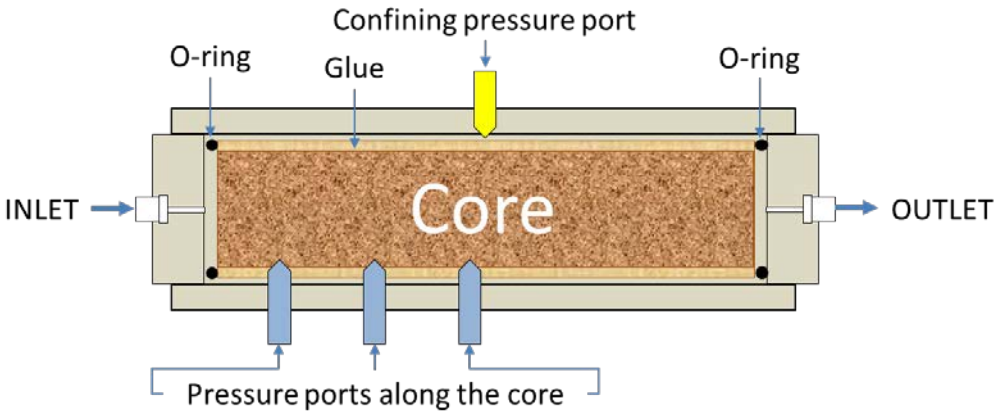

Figure 4-2: Core holder and core plug

4.2 Nanoparticles

Silica (SiO_2) nanoparticles were used in all core-flood experiments. The reason for using silica nanoparticles was their availability in nano-size, spherical shape and negative surface charge. Two batches of silica nanoparticles were purchased from nanoComposix, Prague. Particle specification sheets provided by supplier showed that the silica nanoparticles have a spherical shape (see *Figure 4-3*). Size and other specifications are tabulated in *Table 4-4*. As mentioned earlier, Bentheimer sandstone is composed of about 90-95% quartz and if silica particles are introduced in the rock then it is very likely that there would exist a repulsive force between the grain and particle. This does not ensure that clogging would not take place due to electrostatic forces, as sandstone does contain many other minerals (*see section 4.1.1*), but is an attempt to lessen electrostatic adsorption effect.

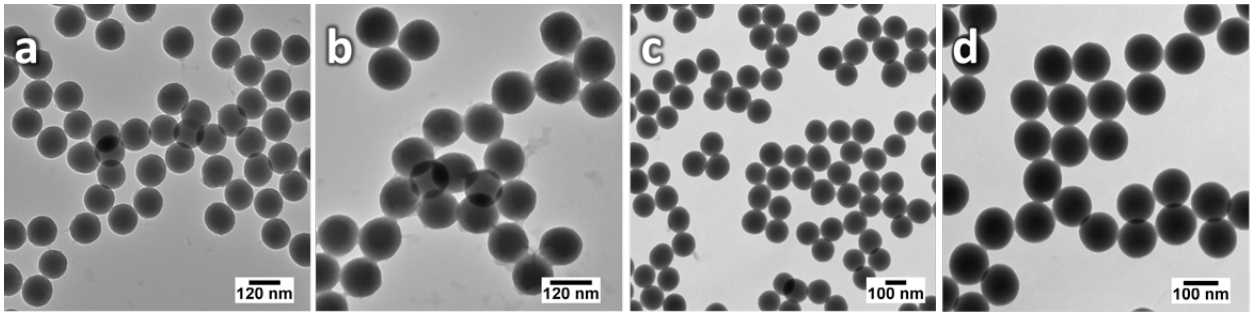

Figure 4-3: TEM Images of Silica nanoparticles provided by nanoComposix. These images are taken with JEOL 1010 Transmission Electron Microscope. a) & b) are for batch-1 and c) & d) are for Batch-2

To reaffirm size of nanoparticles and particle size distribution, samples from both batches were analysed using the most common Dynamic Light Scattering (DLS) technique. DLS is an indirect measurement that is fast and gives hydrodynamic size and size distribution of particles even in nano range while they are dispersed in a liquid. The principle of measurement relies on the size of particles, which move due to Brownian motion, and their speed based on Stokes-Einstein equation [58]. The larger the particle, the slower the Brownian motion will be. Hence, the rate at which intensity of the scattered light fluctuates is different for different sized particles. Smaller particles cause the intensity to fluctuate more rapidly than larger particles. Malvern Zetasizer Nano-ZS device, that uses DLS technique, was used to measure the hydrodynamic size of silica nanoparticles which were found to be in line with the supplier specifications (see *Table 4-4*).

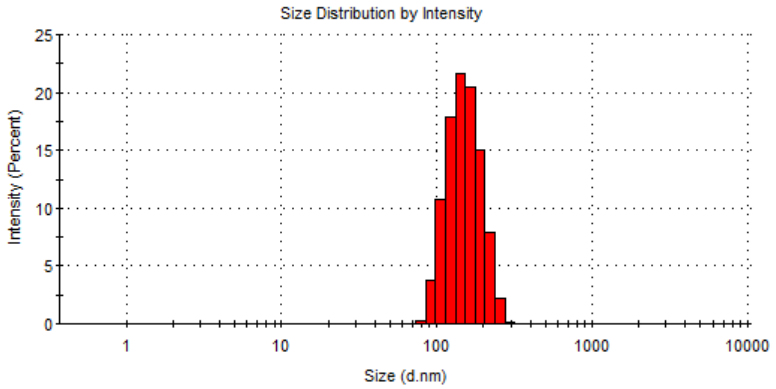

Figure 4-4: Particle size distribution of silica nanoparticles in milliQ water

For reaffirming surface charge, measurements of zeta potential were taken using the same device. The principle of measuring zeta potential and its relevance to surface charge is described earlier in *section 2.2.4.6*. For a description of Zetasizer-ZS equipment, please refer to equipment manual.

Batch No.	Data sheet						Measured			
	Solvent		Shape	Size		Zeta Ptnl.	Solvent		Size	Zeta Ptnl.
	Type	*pH*	*TEM*	*TEM [d.nm]*	*DLS [d.nm]*	*[mV]*	*Type*	*pH*	*DLS [d.nm]*	*[mV]*
1	Milli-Q water	9.1	Spherical	119 ± 6	148.4	-63.3	Milli-Q water	8.3	144.8	-48.8
2	Milli-Q water	9.5	Spherical	119 ± 6	138.0	-51.0	Milli-Q water	8.1	140.2	-43.7

Table 4-4: Specifications of Silica nanoparticles as provided by nanoComposix and measured data

4.3 Brine

Selection of brine was not made arbitrarily. As mentioned earlier, while dealing with nanoparticles, it is important to study the stability of nanoparticles in the brine to avoid particles aggregation. The simplest way to find the stability of a colloidal mixture is through finding out its zeta potential and size distribution [16, 43, 51].

Before presenting the results obtained from nanoparticles stability tests, it is important to recall the electrical properties and surface interaction potentials of nanoparticles (*see section 2.2.4.1*). Size and zeta potential of silica nanoparticles were measured in colloids having different pH, salt concentration and particle concentrations.

4.3.1 Silica Nanoparticle Stability Study in Different Brines

Several samples were prepared using different types and concentration of dissolved salts in filtered (0.45 µm) milliQ water and different concentrations of silica nanoparticles. Particle size and zeta potential measurements were obtained for all these samples using Malvern Zetasizer Nano-ZS. The device displays three readings of each sample (every reading is an average of multiple runs ranging from 12 to 100). *Table 4-5* shows the average results obtained for every three readings of each sample. For some of the samples with dissolved salt concentration more than 10000 ppm, zeta potential readings were unreliable according to zetasizer calculation software.

Sample No.	Brine	Salt Conc. *[ppm]*	Particle Conc. *[ppm]*	pH	Avg. Particle Size *[d.nm]*	Avg. Zeta Ptnl. *[mV]*
SW-1	Synthetic Seawater[d]	33123	10	7.8	671.5	-
SW-2	Synthetic Seawater	33123	100	8.7	1160.0	-
DSW-1	Diluted Seawater	3312	10	8.0	145.4	-21.3
DSW-2	Diluted Seawater	3312	100	8.9	136.3	-23.7
SN-1	$NaNO_3$	850	100	7.1	135.9	-37.5
PC-1	KCl	30000	100	7.2	1602.0	-
SC-1	NaCl	10000	100	7.5	954.3	-17.6
SC-2	NaCl	10000	100	9.4	110.8	-28.2

Table 4-5: Size and zeta potential analysis of silica nanoparticles in different brines

[d] Composition of synthetic seawater is presented in section 4.3.2.

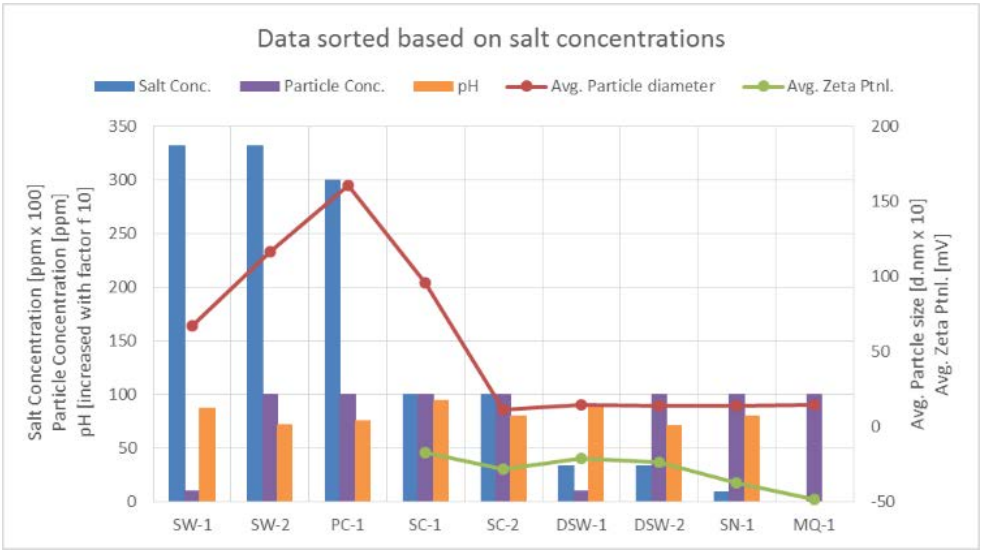

Figure 4-5: Sorted data of size and zeta potential analysis of silica nanoparticles in different brines

From obtained results, following observations were made.

- For same particle concentration and similar pH value *(DSW-1, SW-1), (DSW-2, SW-2)* and *(SN-1, SC-1, PC-1)*, with an increase in dissolved salt concentration, hydrodynamic particle size increases and the magnitude of zeta potential decreases (*see Figure 4-6 a*).
- For same particle concentration and similar dissolved salt concentration irrespective of salt type *(PC-1, SW-2)* and *(SC-1, SC-2)*, with an increase in pH value, hydrodynamic particle size decreases and the magnitude of zeta potential increases (*see Figure 4-6 b*).

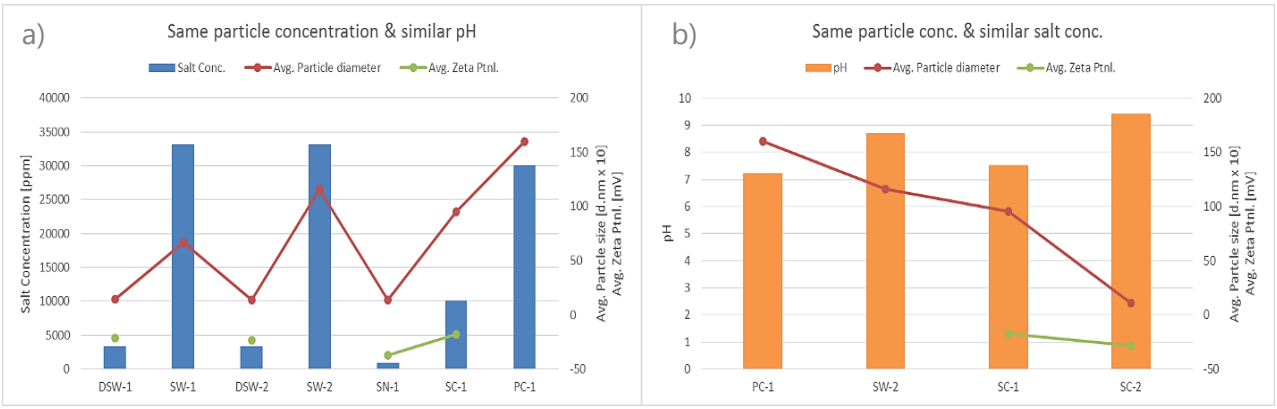

Figure 4-6: a) Samples with same particle concentration and similar pH values b) Samples with same particle concentration and similar salt concentrations

Zeta potential reduces with both, increase in dissolved salt concentration and increase in pH of a sample. From this, it is safe to say that if the salt concentration is below 3000 ppm then silica nanoparticles show hydrodynamic particle size same as provided by the supplier (~140 d.nm). Based on this, diluted synthetic seawater, sodium chloride at higher pH value and sodium nitrate at low concentration gave reasonable results for particle stability. It was decided to use synthetic seawater composition (*see section 4.3.2*) for the brine at a concentration of 1500 ppm. Synthetic seawater was selected to keep the experiments near to real-life situations. Some more tests were conducted on selected brine to further investigate the effect of pH on particle stability.

4.3.2 Diluted Seawater Brine (DSW) Composition

Brine was prepared adopting the synthetic seawater composition. Batches of 10 litres were prepared and then diluted with filtered demineralised water to get salt concentration to 1500 ppm. Brine composition for a batch of 10 L for 33123 ppm concentration is given in *Table 4-6*.

Brine Composition (*Synthetic Seawater*)	
Concentration	33123 *[mg/l]*
Batch size	10 *[litre]*
Cations *[mg/l]*	
Na^+	10182
K^+	371
Ca^{2+}	389
Mg^{2+}	1227
Anions *[mg/l]*	
$SO4^{2-}$	2478
Cl^-	18476
Chloride Salts *[g]*	
NaCl	229
KCl	7
$CaCl_2.2H_20$	14
$MgCl_2.6H_20$	103
Sulphate Salts *[g]*	
$Na_2S0_4.10H_2O$	83

Table 4-6: Synthetic seawater brine composition

4.3.3 Silica Nanoparticle Stability Study in DSW Brine

Four sets of samples were prepared by changing silica particle concentration (~500 ppm, ~250 ppm, ~100 ppm and ~10 ppm). In each set, five samples were prepared by varying their pH. pH was changed by adding drops of 1M HCL and 1M NaOH solutions. Particle size and zeta potential measurements were obtained for all these samples using Malvern Zetasizer Nano-ZS. The results obtained are tabulated in *Table 5-6*.

S. No.	Brine	Salt Conc. *[ppm]*	Particle Conc. *[ppm]*	pH	Avg. Particle Size *[d.nm]*	Avg. Zeta Ptnl. *[mV]*
50-a	Synthetic Seawater	1500 ± 50	50 ± 5	2.7	1013	0.6
50-b	Synthetic Seawater	1500 ± 50	50 ± 5	5.1	1096	-8.5
50-c	Synthetic Seawater	1500 ± 50	50 ± 5	7.0	324	-29.0
50-d	Synthetic Seawater	1500 ± 50	50 ± 5	8.9	351	-24.1
50-e	Synthetic Seawater	1500 ± 50	50 ± 5	10.1	381	-19.7
100-a	Synthetic Seawater	1500 ± 50	100 ± 5	2.3	1049	0.2
100-b	Synthetic Seawater	1500 ± 50	100 ± 5	4.0	1411	-6.5
100-c	Synthetic Seawater	1500 ± 50	100 ± 5	6.6	195	-26.0
100-d	Synthetic Seawater	1500 ± 50	100 ± 5	8.2	173	-27.2
100-e	Synthetic Seawater	1500 ± 50	100 ± 5	10.1	204	-20.1
250-a	Synthetic Seawater	1500 ± 50	250 ± 5	2.6	1229	0.2
250-b	Synthetic Seawater	1500 ± 50	250 ± 5	4.2	976	-13.7
250-c	Synthetic Seawater	1500 ± 50	250 ± 5	6.5	177	-28.5
250-d	Synthetic Seawater	1500 ± 50	250 ± 5	8.2	154	-30.4
250-e	Synthetic Seawater	1500 ± 50	250 ± 5	9.9	785	-25.3

S. No.	Brine	Salt Conc. [ppm]	Particle Conc. [ppm]	pH	Avg. Particle Size [d.nm]	Avg. Zeta Ptnl. [mV]
500-a	Synthetic Seawater	1500 ± 50	499 ± 5	2.5	1578	2.1
500-b	Synthetic Seawater	1500 ± 50	499 ± 5	4.8	1327	-12.4
500-c	Synthetic Seawater	1500 ± 50	499 ± 5	6.7	157	-30.0
500-d	Synthetic Seawater	1500 ± 50	499 ± 5	8.3	146	-32.2
500-e	Synthetic Seawater	1500 ± 50	499 ± 5	10.1	486	-30.4

Table 4-7: Size and zeta potential analysis of silica nanoparticles in synthetic seawater brine

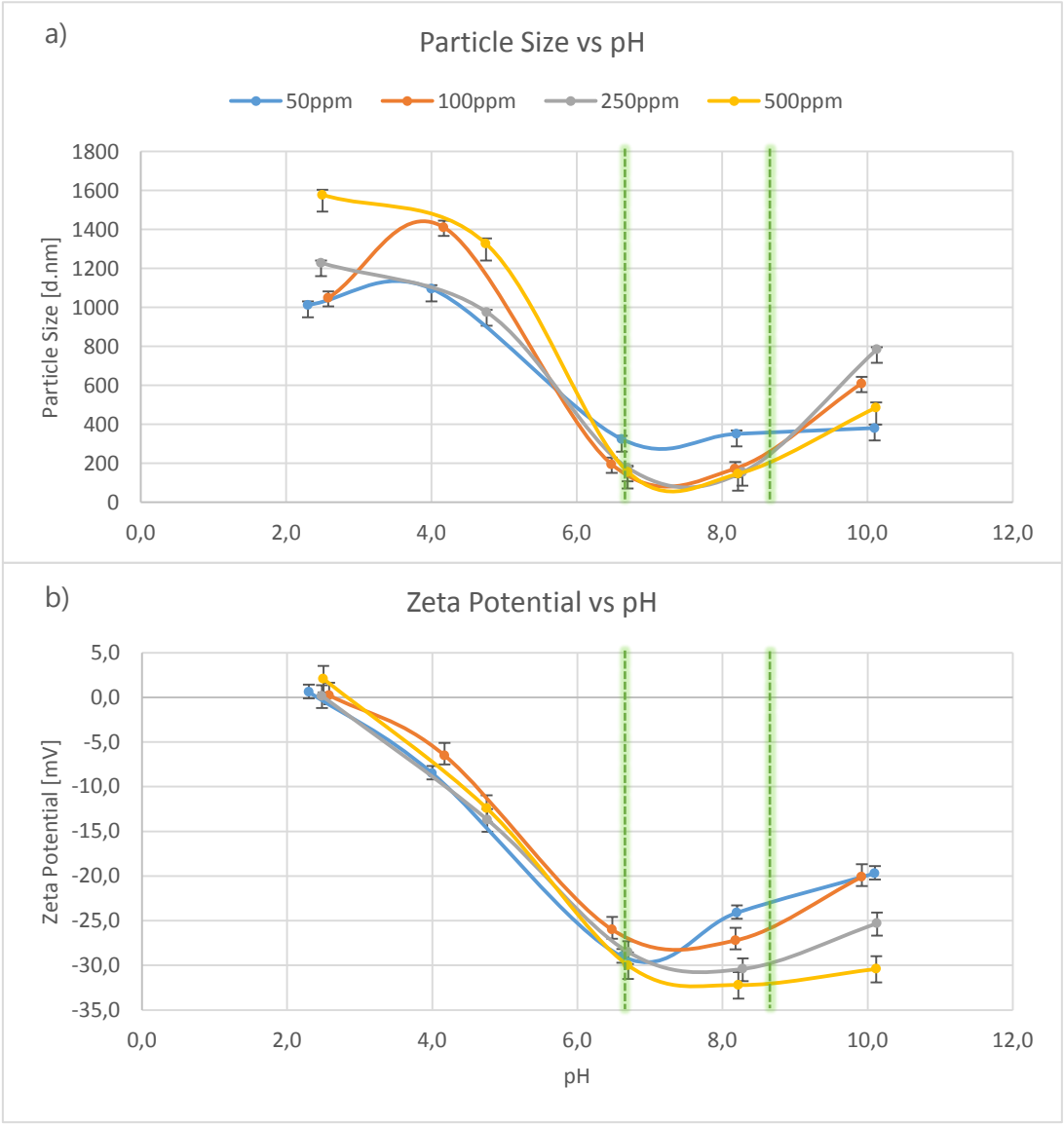

Figure 4-7: Plots of size and zeta potential measurements performed on silica particles in 1500ppm seawater brine. a) Average particle hydrodynamic size versus pH, b) Average zeta potential versus pH.

Figure 4-7 shows the trends of zeta potential and size with increase in pH. It can be observed that with an increase in pH of the solution, zeta potential decreases and after a certain pH value, it starts to increase again. Similar trends are observed in the hydrodynamic particle size.

Initially, at pH of about 2.5, there are sufficient H^+ ions in the electrolyte and as these ions are significantly smaller than all other cations present in the brine, they easily get attracted

by negatively charged nanoparticles and neutralize their surface charge, hence zero zeta potential is observed. pH at this stage is commonly called pH at point of zero charge and written as pH_{pzc}. With further increase in pH value, H^+ ions are relatively reduced in the sample and hence increase in absolute zeta potential is observed. At a higher absolute zeta potential, there exist more repulsive force between particles and solution is stable (*see section 2.2.4.4*). This is also confirmed by the hydrodynamic size trend as reduction in apparent size is observed with increase in pH. With increase in pH, after a certain pH value, absolute zeta potential starts to reduce, this may be as H^+ ions at this stage are relatively too low than OH^- ions, so heavier cations which at lower pH were repelled by H^+ ions make their way in stern layer and start to neutralize the surface charge of particles. Because of this, diffuse layer shrinks, hence reduction in absolute zeta potential value is observed. This causes particles to come close to each other and Van der Waals forces of attraction become stronger than the energy barrier which results in aggregates formation. Formation of aggregates is indirectly confirmed by particle size measurements where bigger size is observed.

Similar tests were performed on samples prepared with 1000 ppm of Bentheimer sandstone mixed in synthetic seawater brine. The sandstone sample used, was taken from the same block from which core plugs were drilled out. Sandstone was crushed and mixed with synthetic seawater brine. The sample was then sonicated for 15 mins. Drops of 1M HCL and 1M NaCl solutions were used to obtain desired pH. Two sets of tests were performed as shown in *Table 4-8*.

Test 1				Test-2			
Sample No.	*Salt Conc. [ppm]*	*pH*	*Avg. Zeta Ptnl. [mV]*	*Sample No.*	*Salt Conc. [ppm]*	*pH*	*Avg. Zeta Ptnl. [mV]*
SST-1a	1500 ± 50	3.0	-20.3	SST-2a	1500 ± 50	2.2	-0.6
SST-1b	1500 ± 50	5.5	-19.8	SST-2b	1500 ± 50	4.0	0.0
SST-1c	1500 ± 50	7.2	0.3	SST-2c	1500 ± 50	6.0	0.4
SST-1d	1500 ± 50	7.5	0.3	SST-2d	1500 ± 50	7.0	0.3
SST-1e	1500 ± 50	9.8	0.2	SST-2e	1500 ± 50	8.0	-32.3
SST-1f	1500 ± 50	10.0	-0.1	SST-2f	1500 ± 50	10.0	-0.2

Table 4-8: Zeta potential analysis of Bentheimer sandstone in synthetic seawater brine

Zetasizer nano device gave error messages while performing measurements of zeta potential with sandstone. Also, the results obtained from both tests do not match at all. This error could be due to different components in the sandstone that behave differently in the brine and have different surface charges. Samples had to be agitated all the time to keep suspension stable whereas while measurement in Zetasizer, sample cannot be agitated, which resulted in sedimentation of sandstone particles in the suspension. Hence, the results for zeta potential of sandstone are not considered reliable.

Based on the results discussed in this section, to keep the silica nanoparticle colloid stable when it is injected in the Bentheimer sandstone core plug, it is was decided to keep the salt concentration in brine at 1500 ppm and pH of the solution in the rage of 6.5 to 8.5 highlighted in *Figure 4-7* by green dotted lines. This pH range will be referred to as "stable range" henceforward in this document.

4.4 Experimental Setup

Experimental setup was designed and built in Delft University of Technology's geo-engineering laboratory. Setup comprised of various parts that are discussed in this section. Overall pressure rating of the experimental setup was 38 Bar.

4.4.1 Core Holder

Core plug holder made of Poly Ether Ether Ketone (PEEK) i.e. a special polymeric material (KETRON PEEK 1000) which has excellent mechanical property and is transparent to X-rays [59] was used. With core plug enclosed in hardened glue and encapsulated in PEEK core holder, the combination can withstand pressure up to 40 Bar and temperature up to 70°C. The core holder had three pressure ports and one confining pressure port (*see Figure 4-2*).

4.4.2 Injection Pump

Injection pump was used for the injection of water into the system for cleaning/flushing the system, injection of brine for permeability test and injection of silica nanoparticle colloid for the experiments, ISCO 500D-Series, dual syringe pump and Quizix-QX pump were used. ISCO pump had flowrate accuracy of ±0.5% of set point whereas Quizix had flowrate accuracy of ±0.1% of set point.

4.4.3 Pressure Measurements

Four pressure differential transducers and two pressure sensors were used for pressure measurements. One differential pressure transducer of ±40 Bar rating was used to measure pressure difference along the inlet and outlet of the core. Three differential pressure transducers of ±3 bar rating were used to measure the pressure difference between specific points along the core (*see section 4.1.4*). Inlet and outlet pressures were monitored using pressure sensors of ±50 Bar rating. All pressure sensors and differential pressure transducers were calibrated prior to experiments and had an offset of ± 0.001 Bar and ±0.01 Bar respectively about the set point. All pressure sensors and differential pressure transducers readings were recorded using data acquisition software 'MP3 Measure' developed by National Instruments.

4.4.4 Flowlines, Connections & Accessories

Flow lines were made up by using plastic tubing with pressure rating of 38 Bar. For connections, sample points and regulating the flow, Swagelok fittings and valves were used. Along with aforementioned parts, setup included a CO_2 cylinder, vacuum pump, back pressure valve for applying back pressure and confining pressure of 25 Bar and N_2 cylinder to apply pressure on back pressure valve for initially saturating the core plug with brine prior to each experiment.

4.4.5 Experimental Setup Diagram

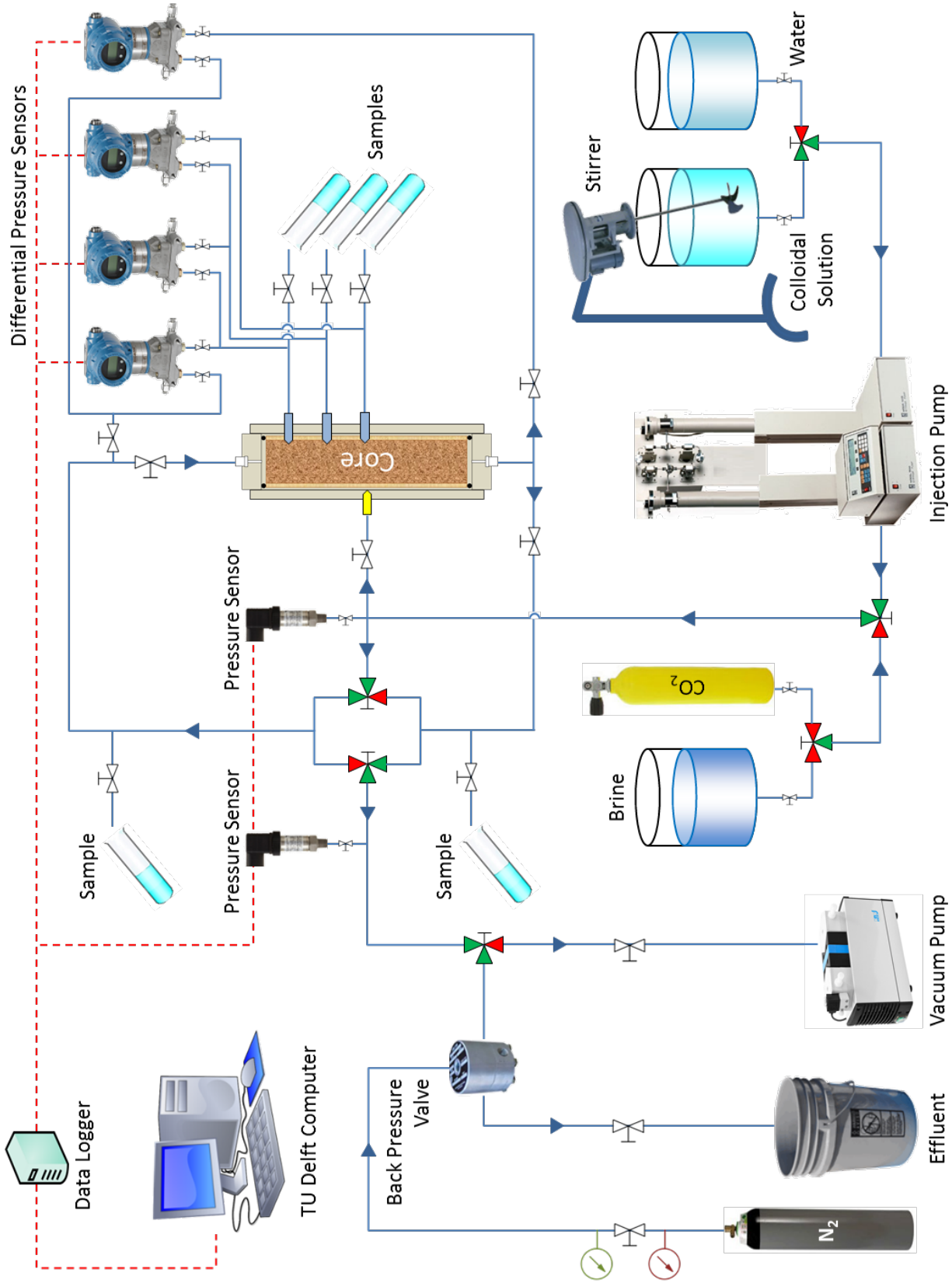

Figure 4-8: Experimental setup diagram

4.5 Experimental Procedure

Prior to starting experiments, the cumulative dead volume of all flow lines, connections and valves was measured precisely. The volume before core inlet and after core outlet were measured. All experiments were conducted at a temperature of 24 ± 3°C and back pressure of 1 ± 1 Bar. The same procedure was followed for all experiments.

1. After placing the core into core holder, initial CT scan of the dry core was taken.
2. All lines in the setup were flushed with CO_2 to make sure no air is present in the lines. Then core holder containing the dry core plug was installed in the system and was flushed with CO_2 for 30 min at atmospheric pressure to remove trapped air from the core plug.
3. The system was then pressurized to 2-3 Bar with CO_2 for a leak test. All connections were checked with snoop leak detection fluid. If a leak was observed, connections were remade.
4. After ensuring no leak, the system was vacuumed at -1 Bar overnight to ensure no moisture or air remained in the system.
5. After that vacuum was filled with CO_2 again, brine was injected into the system at 1 ml/min by allowing the brine to enter the core from the bottom. This is done to ensure gravity stable condition so that no air bubble is formed in the core plug while saturation. Injection of brine was continued until all remaining CO_2 gets dissolved in brine and comes out.
6. Then the back pressure of 10 Bar was applied while injecting brine at the rate of 1 ml/min up to 15-20 pore volumes to ensure complete saturation of core with brine.
7. Once the core gets saturated, permeability tests were conducted. Absolute permeability was calculated by measuring pressure drop across the core at different flow rates.
8. Then brine without silica particles was injected to observe any permeability reduction due to brine. The injection volume of brine varied for all experiments. The brine injection was stopped once differential pressure across the core became stable.
9. After this, colloid was injected into the core plug at a desired rate and 10 ml sample of injection fluid was taken at the inlet of the core plug to obtain initial injection concentration of silica nanoparticles.
10. Samples at inlet and outlet of the core plug were taken periodically to obtain silica nanoparticle concentration profile over time.
11. After completion of the experiment, core holder was removed from the system and final CT scan of the core was taken.
12. Core plug was then removed from the holder and cut into half along the length of core plug for SEM analysis.
13. All lines and pump were flushed by injecting fresh water through the system at high flow rates to remove any retained particles.

4.6 Post Experiment Analysis Techniques

4.6.1 Silicomolybdate Method

The silicomolybdate method was used to analyze colloidal mixture samples obtained at inlet and outlet of the core plug. This is a well-established method that allows measuring the concentration of silica in brine or water using spectrophotometry [60, 61]. Hach method 8185 (Hach Company, 2014) uses the same approach and was followed in this study due to its simplicity of execution, cost and availability. Hach method comprises of molybdate reagent pillow (Na_2MoO_4), acid reagent pillow (H_3NSO_3) and citric acid powder pillow. First molybdate reagent pillow is added in a 10ml sample and swirled until it dissolves. Then acid reagent pillow is added and swirled till the reagent mixes completely. At this point, yellow color starts to appear if the silica is present in the sample. Silica reacts with molybdate ions under acidic conditions to form yellow color Silicomolybdic acid complexes ($H_4[SiO4.Mo_{12}O_{36}].xH_2O$). The sample is then given 10 min reaction time. If there is phosphate in the sample then citric acid powder pillow should be added then and 2 minute reaction time should be given as well. This neutralizes any yellow color formed due to phosphate interference. The sample is then placed in the spectrophotometer device and the absorbance value is noted. Different samples with the known concentration of silica nanoparticles in brine were prepared initially and their corresponding absorbance values were used to get a baseline plot. Silica concentration in the samples obtained from the experiments was then obtained from this plot.

4.6.2 Scanning Electron Microscopy and CT-Scan

SEM images were also taken for first 3 experiments by breaking the core into two pieces along the length of the core. Results obtained were not promising. Silica nanoparticles were not visible in SEM images. One of the reasons for this is the limitation of SEM's resolution but the main reason is the fact that Bentheimer sandstone is mainly composed of quartz i.e. silica, hence there is no density contrast between the grains and nanoparticles. For the same reason, medical CT-scan images were also unable to detect nanoparticles.

5 Results & Discussion

To study the effect of ultrafiltration on injectivity decline, eight core flood experiments were conducted on Bentheimer sandstone core plugs. Filtered 15 times diluted synthetic seawater brine was initially injected which was followed by colloid in all experiments. Operating parameters such as flow rate, colloidal concentration and pH of colloid were varied in the conducted experiments. In this section results obtained from these experiments are presented and discussed.

The raw data obtained from experiments was pressure profile and colloidal influent/effluent concentration. Pressure data was used to obtain the permeability profiles for all experiments. These profiles were compared with respect to changes in effluent concentrations and operating parameters to get insight into the flow of nanoparticles through porous media.

5.1 Core Plug Parameters

Eight core flood (CF) experiments were conducted using Bentheimer sandstone cylindrical core plugs. These experiments were labelled CF-1 through CF-8. For each core plug, absolute permeability was measured after saturating the core (*see section 4.1.3*) using the same brine that was used for preparing colloid. Core plug related properties are tabulated below in *Table 5-1*.

Experiment No.	Length *[mm]*	Diameter *[cm]*	X-section Area *[cm^2]*	Pore Volume *[cm^3]*	Absolute Permeability *[Darcy]*
CF-1	17.05	3.85	11.64	45.65	2.85
CF-2	17.00	3.80	11.34	44.35	2.71
CF-3	16.95	3.85	11.61	45.27	3.05
CF-4	16.95	3.85	11.61	45.27	3.30
CF-5	17.00	3.85	11.61	45.40	2.92
CF-6	17.00	3.85	11.61	45.40	3.08
CF-7	10.54	3.85	11.64	28.18	3.24
CF-8	17.01	3.80	11.34	44.35	2.74

Table 5-1: Bentheimer core plug properties for each experiment

While injecting brine for permeability calculation, some unexpected readings were obtained from the pressure points along the core. The first segment of the core plug (i.e. ~21mm) always showed relatively lower permeability in comparison to the other segments of the core. For an example, permeability variation in the core plug CF-3 is presented. *Figure 5-1* shows linear regression obtained from the pressure drop data for each segment of CF-3 core plug.

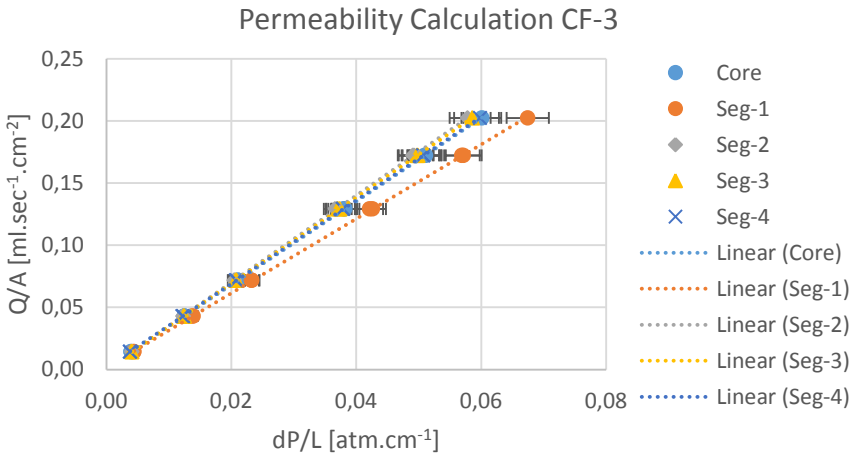

Figure 5-1: Permeability calculation from pressure drop data from each segment of the CF-3 core plug. Slope of the linear regression multiplied with viscosity (0.91cP) gives the permeability

Permeability in all four segments of the CF-3 core plug was 2.72 D, 3.19 D, 3.15 D, 3.06 D respectively and 3.05 D of the whole core. The standard deviation of the absolute permeability of each segment excluding the first segment is 6.7 %. This could be attributed to the minor heterogeneity of the rock and is usual for semi-homogeneous sandstones such as Bentheimer sandstone. Including the first segment in the analysis yields a standard deviation of 21.2 %. The difference in the permeability of first segment and rest of the segments was similarly observed in all the core plugs used in experiments. Comparable mismatches can be found in the literature where core flood experiments are involved. *Table 5-2* shows the permeability derived from pressure taps along the core for each experiment.

Exp. No.	Core	Segment 1	Segment 2	Segment 3	Segment 4	Stdv. (Excl. Segment 1)
	[Darcy]	*[Darcy]*	*[Darcy]*	*[Darcy]*	*[Darcy]*	*[%]*
CF-1	2.85	1.68	3.20	3.30	3.09	10.7
CF-2	2.71	1.43	3.15	3.02	2.99	8.4
CF-3	3.05	2.72	3.19	3.15	3.06	6.7
CF-4	3.30	3.02	3.36	3.36	3.34	1.1
CF-5	2.92	2.34	3.05	3.22	2.94	14.1
CF-6	3.08	2.54	3.26	3.22	3.12	7.2
CF-7	3.24	3.00	3.33	3.41	3.12	0.2
CF-8	2.74	1.32	3.16	3.13	3.06	5.3

Table 5-2: Permeability variation in each segment of the core plugs used in experiments

The reason for this mismatch could be argued that the first segment has significantly lower permeability due to the consequence of the sawing procedure of cutting the core plugs. Sawing core plugs to desired length results in damaging the face of the core plug which results in lower permeability of the first segment. On the other hand, this could be due to the inaccuracy in the measurement of the length of the first segment and subsequent segments. In most cases, this mismatch could be due to both effects [30, 37]. The first segment of the core cannot be ignored and hence differential pressure along the whole core plug was taken to calculate absolute permeability of core plugs. Linear regression plots obtained from the pressure drop data for each segment of all the core plugs used in experiments are presented in *Appendix C*.

5.2 Flow Parameters

Flow parameters were kept such that near wellbore conditions of a water injection well can be achieved as much as the experimental setup could allow. This includes relatively higher injection rates compared to usual core flood experiments as typical fluid flow velocities in the vicinity of an injection well are usually in the range 10^{-3} to 10^{-2} m/s [30]. The concentration of colloids in the injection fluid was kept 50 to 100 ppm. Injection related parameters are tabulated in *Table 5-3*.

Exp. No.	Brine pH	Np Concentration	Injection Rate	Total PV Injected	Duration
		[ppm]	*[ml/min]*	*[PV]*	*[hrs]*
CF-1	7.2	50	47	2188	35.4
CF-2	7.1	100	141	43142	226.2
CF-3	7.4	50	141	38543	206.2
CF-4	7.3	100	141	38639	206.7
CF-5	9.6	100	141	5188	27.8
CF-6	4.0	100	141	6114	32.8
CF-7	6.8	50	47	1790	17.9
CF-8	7.3	50	141	28633	149.3

Table 5-3: Injection related parameters along with permeability reduction percentage derived from pressure drop data for brine and colloidal mixture flow for each experiment

5.3 Initial Brine Flow

Filtered brine was injected in experiments CF-1 through CF-8 prior to colloid injection except for CF-7. The reason for injecting brine was to ensure rock properties do not change any further due to brine and rock interaction. This was achieved by first filtering brine with a 0.45µm filter to ensure no suspended particles are present in the brine. It was observed that the absolute permeability of the core plugs reduced further from what was calculated before. The extent of permeability damage was from 1.5 to 10% (*see Table 5-4*). This reduction could be due to fines migration and/or clay swelling. Permeability obtained at this stage was taken as initial permeability (k_0).

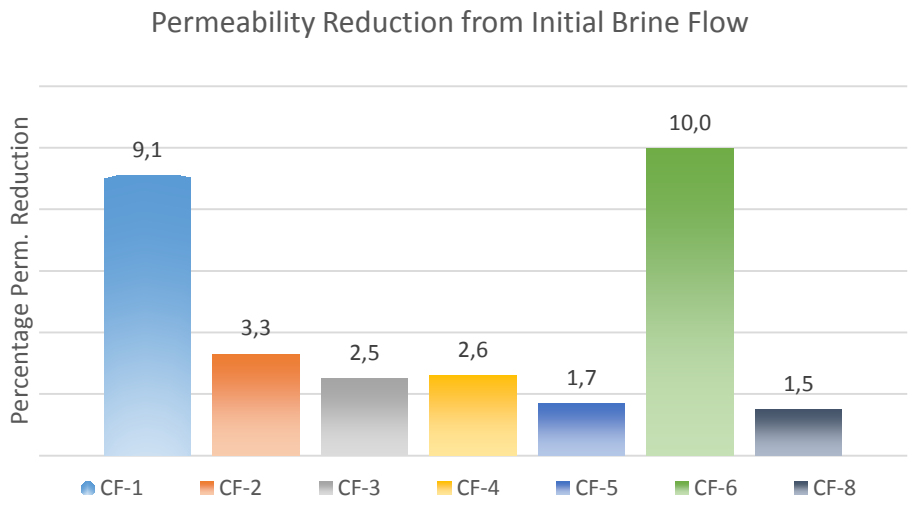

Figure 5-2: Permeability reduction percentage from initial brine flow in all experiments

Exp. No.	Pore Volume [cm^3]	Brine pH	Injection Rate [cm^3/min]	Brine Injected [PV]	Absolute Permeability [Darcy]	Perm. after Brine Inj. (k_0) [Darcy]	Permeability Reduction [%]
CF-1	45.65	7.2	47	1073	2.85	2.59	9.1
CF-2	44.35	7.1	141	4548	2.71	2.62	3.3
CF-3	45.27	7.4	141	834	3.05	2.97	2.5
CF-4	45.27	7.3	141	3089	3.30	3.21	2.6
CF-5	45.40	9.6	141	4593	2.92	2.87	1.7
CF-6	45.40	4.0	141	1061	3.08	2.75	10.0
CF-7	28.18	6.8	47	-	3.24	-	-
CF-8	44.35	7.3	141	724	2.74	2.70	1.5

Table 5-4: Permeability reduction percentage derived from pressure drop data for initial brine flow through Bentheimer sandstone for each experiment

5.4 Main Colloidal Flow

Once initial permeability was obtained after initial brine injection, silica nanoparticle colloid was injected. During colloidal flow, differential pressure was recorded along the core (*see section 4.1.4 and 4.4.3*). These pressure measurements provided insight into deposition profile and overall injectivity decline. Influent and effluent samples were taken at regular intervals and were analysed to provide silica concentration profile over time.

Before presenting the results obtained, it is important to characterize the experiments based on some important parameters that were changed.

- Experiments CF-1 through CF-4 were conducted while keeping the colloidal pH in the stable range that was obtained through stability analysis (*see section 4.3.3*).
- Experiment CF-5 and CF-6 were conducted at colloidal pH above and below the stable range respectively.
- Experiment CF-7 was conducted with a core containing a fracture and injection fluid having iron particles along with silica nanoparticles.
- Experiment CF-8 was unsuccessful due to changing of the injection pump and therefore presented in *Appendix C*.

It is also important to note that plots obtained from normalized values will be used to represent permeability decline, pressure drop and pressure. Permeability is normalized with respect to initial permeability k_0 (obtained after initial brine injection). Pressure drop is computed from differential pressure readings which is normalized with respect to initial differential pressure dP_0. Pressure is normalized with respect to back pressure or end pressure P_{end} i.e. ~1 Bar for all experiments.

5.4.1 Particle vs Pore Size Distribution

To signify the difference between particle and pore size, let us recall silica nanoparticle size distribution (*see section 4.2*) and Bentheimer sandstone's mean pore size distribution obtained from MIP (*see section 4.1.2*). *Figure 5-3* shows the nanoparticle distribution in comparison to pore size distribution. This gives an idea of how small the injected particles are in comparison to space available for their flow. It is clearly visible from *Figure 5-3* that order of magnitude 2 difference in size exists between particle and pore size.

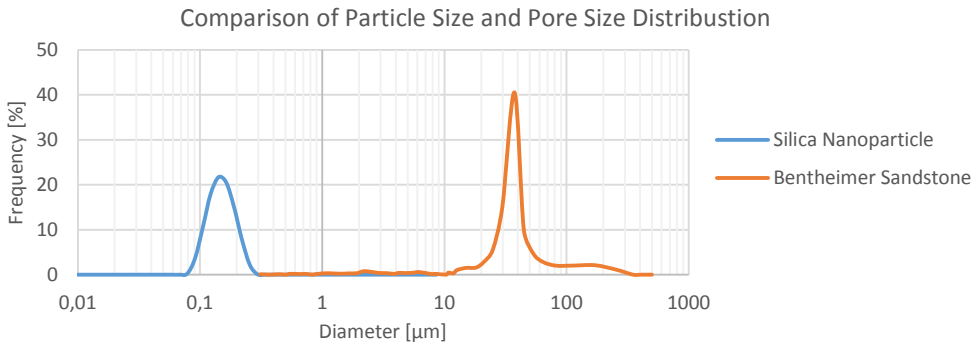

Figure 5-3: Comparison of Silica nanoparticle size distribution and Bentheimer sandstone pore size distribution

5.4.2 Experiment CF-1 through CF-4

In experiment CF-1, colloid of concentration 50 ppm was injected at the rate of 47 ml/min for about 1100 PVs. Almost linear permeability damage was observed. No external filter cake was formed that can be seen in Figure 5-4. The jumps in the trend are due to frequent sampling at injection till 1000 PV, after that sample duration was prolonged which is clearly visible. From Figure 5-5 it is observed that permeability damage is significant near the injection face i.e. permeability damage or increase in pressure is largest in segment 1.

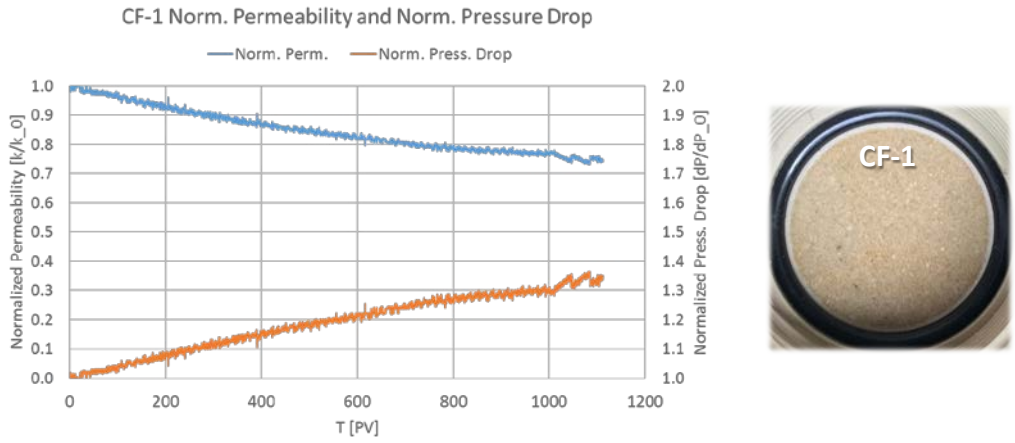

Figure 5-4: Left: Norm. Permeability and pressure drop over PV injected, Right: Injection face of the core after exp. CF-1

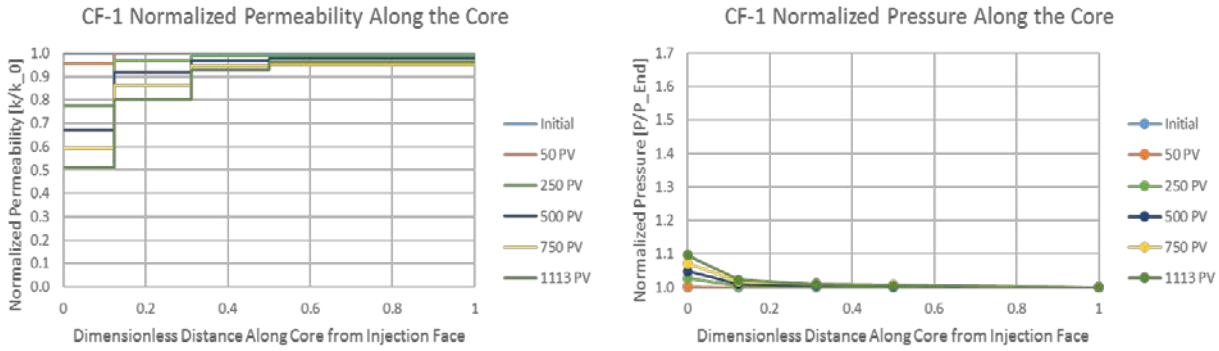

Figure 5-5: Normalized permeability and pressure along the core at different injected PV of experiment CF-1

Duration of this experiment was kept in accordance with core flood experiment's duration found in literature i.e. usually from few hundred pore volumes to thousand pore volumes [8,

30, 59]. From the result obtained it was evident that even this duration was not sufficient to fully capture the whole trend of the colloidal flow through porous media. The trend obtained in CF-1 shows a linear decline in permeability and if it is extrapolated, it would continue till the permeability goes to zero. Therefore, next experiments were conducted for longer durations to fully capture the deposition phenomenon.

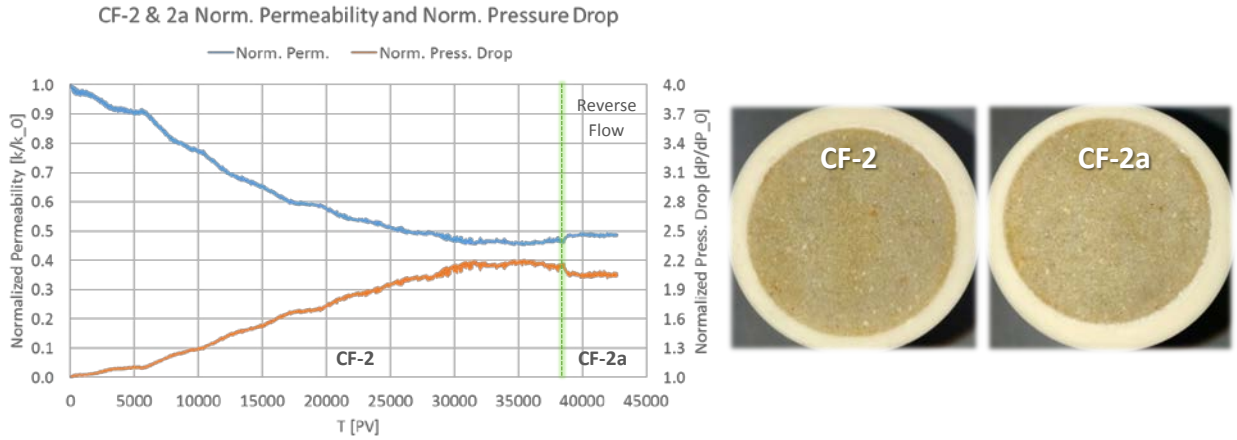

Figure 5-6: Left: Norm. Permeability and pressure drop over PV injected, Right: Injection face of core after exp. CF-2 & 2a

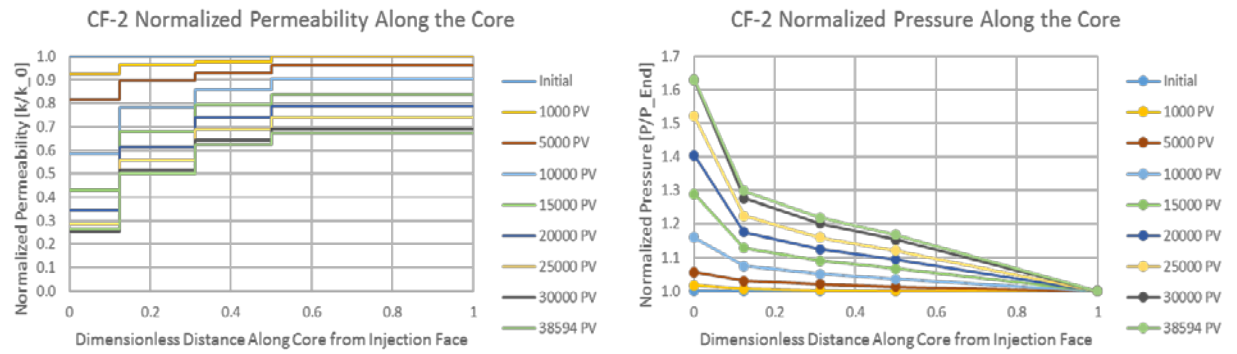

Figure 5-7: Normalized permeability and pressure along the core at different injected PV of experiment CF-2

Experiment CF-2 was conducted with 100 ppm colloid concentration which was injected at the rate of 141 ml/min (3x of CF-1's injection rate) for about 38500 PV. From the trend obtained for normalized permeability shown in *Figure 5-6* on the left section of the green dotted line, it is was observed that after about 28000 PV no further permeability damage took place and a plateau was attained after 53% permeability reduction. This experiment was further extended by inverting the core holder so that injection takes place from the opposite side of the initial injection face. This extension was named CF-2a. This was done to observe whether reverse flow could result in releasing the retained nanoparticles. In *Figure 5-6*, right section of the green dotted line shows the reverse flow. All other flow parameters were kept same. Recovered permeability accounted for 2.2% of initial permeability k_0, which is not a significant increase. Normalized permeability and pressure along the core at different pore volumes shown in *Figure 5-7* indicate a similar trend, but more pronounced, as experiment CF-1. Also, no external filter cake was formed on the injection faces as shown in *Figure 5-6* right.

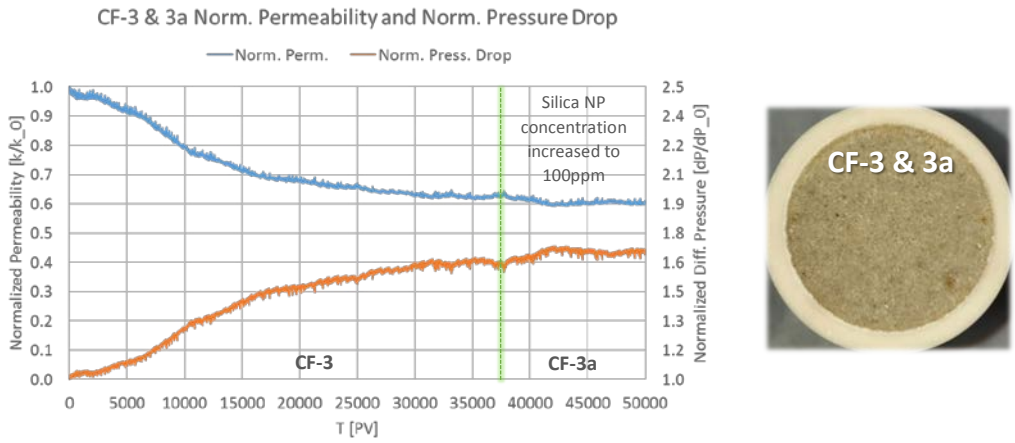

Figure 5-8: Left: Norm. Permeability and pressure drop over PV injected, Right: Injection face of core after exp. CF-3 & 3a

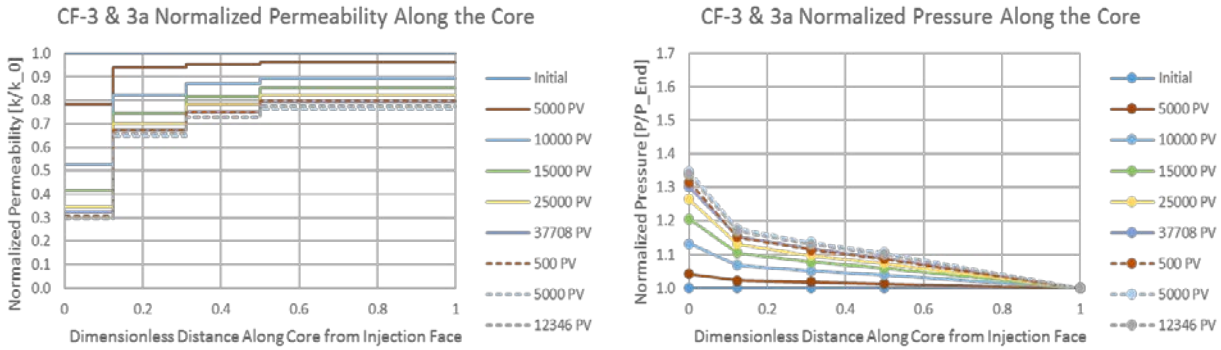

Figure 5-9: Normalized permeability and pressure along the core at different injected PV of experiment CF-3 & 3a

Experiment CF-3 was conducted with 50 ppm colloid concentration which was injected at rate of 141 ml/min for about 37700 PV. From the trend obtained for normalized permeability shown in *Figure 5-8* on the left section of the green dotted line, it is was observed that after about 28000 PV no further permeability damage took place and a plateau was attained similar to CF-2 after 37% permeability reduction. This experiment was further extended by increasing silica nanoparticle concentration in the injection colloid to 100 ppm. This extension was named CF-3a. The reason was to observe whether increasing nanoparticle concentration in the injected colloid could cause additional permeability reduction that may reach the same level as experienced in CF-2. In *Figure 5-8*, right section of the green dotted line represents CF-3a. All other flow parameters were kept same. An additional decrease in permeability accounted for 2.7% of initial permeability k_0, which is not significant. This indicates that no further substantial retention is taking place once the plateau is achieved. Normalized permeability and pressure along the core at different pore volumes shown in *Figure 5-9* depict a similar trend as experiment CF-2. Also, no external filter cake was formed on the injection face as shown in *Figure 5-8* right.

Experiment CF-4 was conducted with 100 ppm colloid concentration which was injected at the rate of 141 ml/min for about 35500 PV. From the trend obtained for normalized permeability shown in *Figure 5-10*, it is was observed that after about 28000 PV no further permeability damage took place and a plateau was attained after 31% permeability reduction.

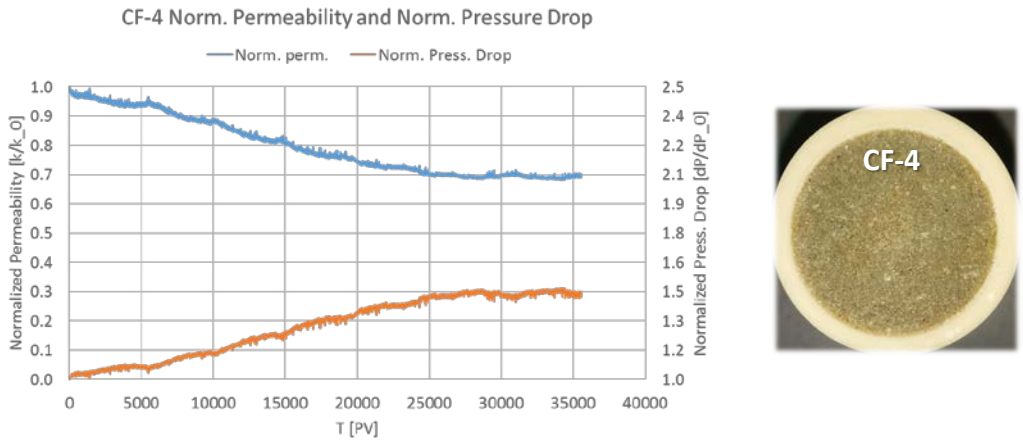

Figure 5-10: Left: Norm. Permeability and pressure drop over PV injected, Right: Injection face of the core after exp. CF-4

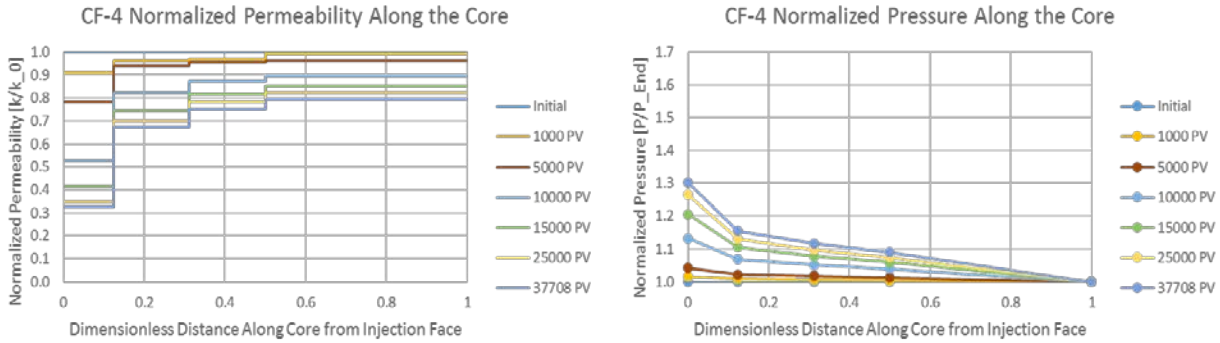

Figure 5-11: Normalized permeability and pressure along the core at different injected PV of experiment CF-4

Normalized permeability and pressure along the core at different pore volumes shown in *Figure 5-11* indicate a similar trend as experiment CF-3. In this experiment also, no external filter cake was formed on the injection face as shown in *Figure 5-10* right.

5.4.3 Experiment CF-5 and CF-6

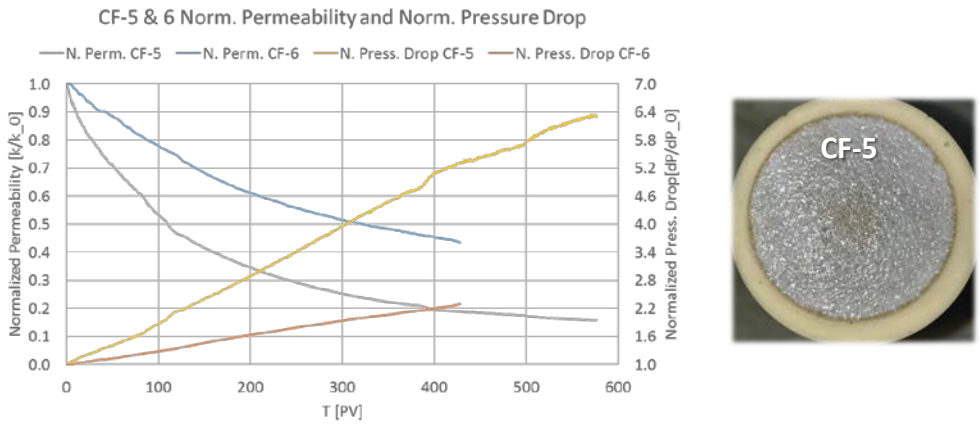

Figure 5-12: Left: Norm. Permeability and pressure drop over PV injected for experiment CF-5 and 6, Right: Injection face of the core after exp. CF-5

Experiment CF-5 and CF-6 were both conducted with 100 ppm colloidal concentration which was injected at the rate of 141 ml/min, colloidal pH was kept 9.6 and 4.0 respectively. The reason for keeping pH outside the stable range was to validate the stability study performed

on brine and nanoparticle interactions presented earlier in *section 4.3.3*. Results obtained from these experiments show drastic linear permeability decline, unlike earlier experiments, over less than 600 PV injection. Permeability reduction in CF-5 and CF-6 were about 85% and 56% respectively. This is attributed to the formation of external filter cake at injection face and sensitivity of clay minerals in sandstone to pH variation. Image of EFC for experiment CF-5 is shown in *Figure 5-12* right. Thickness calculation of EFC is provided in *Appendix C*.

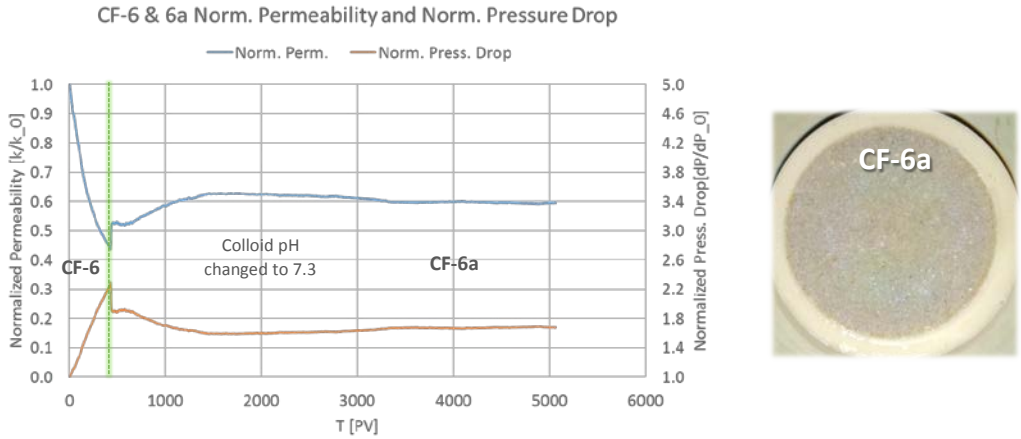

Figure 5-13: Left: Norm. Permeability and pressure drop over PV injected for experiment CF-6 and 6a, Right: Injection face of the core after exp. CF-6a

CF-6 was further extended by increasing colloidal pH from 4.0 to 7.3. This extension was named CF-6a. The reason was to observe whether increasing colloidal pH to stable range could help in removing external filter cake from injection face. In *Figure 5-13*, right section of the green dotted line shows CF-6a. All other flow parameters were kept same. Recovered permeability accounted for 16% of initial permeability k_0. From the image of injection face of core plug used in CF-6 and 6a shown in *Figure 5-13* right, it visible that external filter cake did form in CF-6 but was largely removed in CF-6a.

5.4.4 Experiment CF-7

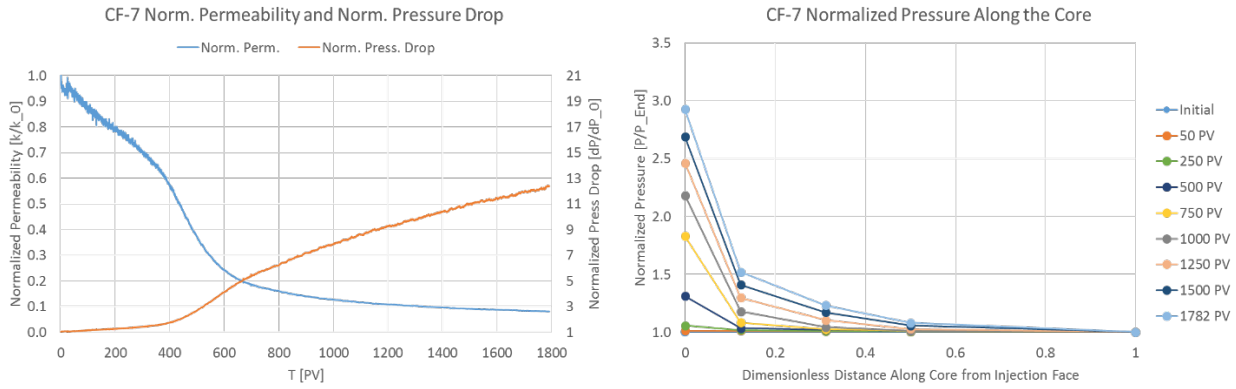

Figure 5-14: Left: Norm. Permeability and pressure drop over PV injected, Right: Norm. Pressure along the core at different injected PV

In experiment CF-7, colloid of concentration 50 ppm was injected at the rate of 47 ml/min for about 1800 PVs. The core plug used in this experiment had a fracture along the core as shown in the CT scan image in *Figure 5-15* left. Also, the injection bucket contained an iron washer that got oxidized and released iron particles. Image of injection bucket after

concluding the experiment is shown in *Figure 5-15* middle. Therefore, injection fluid contained both silica nanoparticles and iron particles. From the trend observed for permeability damage, it can be inferred that both internal and external filter cakes were formed.

Figure 5-15: Left: CT scan image of fracture along the core, Middle: Rust formation in injection bucket, Right: Injection face of the core after exp. CF-7

Table 5-5 shows a summary of the results obtained from all earlier presented experiments. Minus sign in injectivity decline column in *Table 5-5* represents recovered injectivity.

Exp. No.	Pore Volume	Brine pH	Np Conc.	Injection Rate	Colloid Injection	Initial Perm (k_0)	Perm. after Np Injection	Injectivity decline
	[ml]		*[ppm]*	*[ml/min]*	*[PVI]*	*[Darcy]*	*[Darcy]*	*[%]*
CF-1	45.65	7.2	50	47	1113	2.59	1.93	25.5
CF-2	44.35	7.1	100	141	38594	2.62	1.23	53.0
CF-2a	44.35	7.1	100	141	4111	2.62	1.29	-2.2
CF-3	45.27	7.4	50	141	37708	2.97	1.87	37.0
CF-3a	45.27	7.4	100	141	12346	2.97	1.79	2.7
CF-4	45.27	7.3	100	141	35549	3.21	2.23	31.0
CF-5	45.40	9.6	100	141	576	2.87	0.44	85.0
CF-6	45.40	4.0	100	141	428	2.75	1.20	56.5
CF-6a	45.40	7.3	100	141	4640	2.75	1.64	-16.0
CF-7	28.18	6.8	50	47	1782	3.24	0.26	92.0

Table 5-5: Summary of flow parameters and injectivity decline percentage derived from pressure drop data

5.5 Discussion

In all the experiments conducted in this study, the concentration of silica nanoparticles was kept higher than theoretical values of colloid concentration expected in ultra-filtered water (i.e. <10 ppm). One of the reasons to keep concentration high was to accelerate retention of nanoparticles which would result in reduced experimental duration while the other reason was to minimize error in the influent and effluent analysis. If the concentration is too little, then the spectrophotometric method used in this study (*see section 4.6.1*) does not provide with reliable results. Plots for influent/effluent analysis are presented in *Appendix C*

Based on the results obtained from CF-1 it was decided to run other experiments for longer durations. Few hundred pore volumes are not enough to capture complete retention phenomena of nanoparticle flow through porous media at injection rates similar to this study. Also, it was observed that frequent sampling caused variation in injection rate which resulted in a lower slope of the pressure drop than when the samples were taken at longer intervals. During sampling at injection, flow through core plug is minimal. Hence, the

nanoparticles that got retained due to direct interception, inertial or hydrodynamic effects may get released and once the flow resumes, they follow the streamlines and less flow resistance is faced than before sampling. This effect is clearly visible in pressure drop plot shown in *Figure 5-4*.

In normalized permeability plots of experiments CF-2, 3 and 4, three phases are prominently visible that are shown in *Figure 5-16* separated by two light green bars and are labelled A, B and C. Light green bars indicate a range in PVs after which next phase starts.

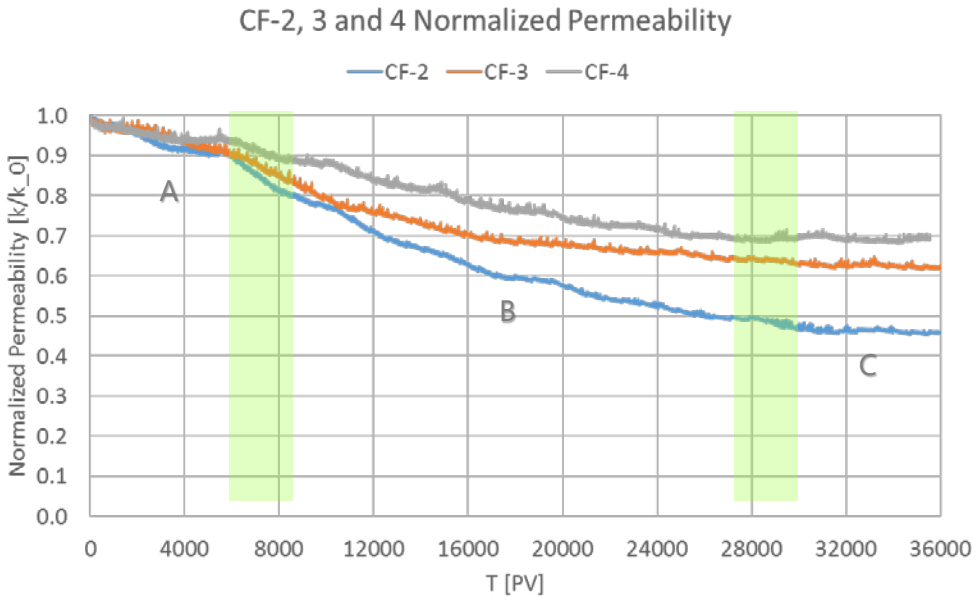

Figure 5-16: Normalized permeability over pore volumes injected for CF-2, 3 and 4

In phase A, the derivative of normalized permeability has a lower value. After some pore volumes injected, the value of the derivative becomes relatively higher i.e. phase B. This phase stays for a longer duration compared to phase A and is followed by phase C where the derivative of normalized permeability goes to zero which means no further permeability decline takes place. This could be explained in terms of retention mechanisms at the pore scale. The average size of injected nanoparticles in comparison to mean pore size of Bentheimer sandstone is very small (*see section 5.4.1*). Initially, when injection commences (i.e. phase A), due to the considerably small size of nanoparticles they can easily pass through the core. This rules out direct interception or plugging mechanism whereas all other depositional mechanisms are still taking place which includes dispersion/diffusion, inertial, hydrodynamic and electrostatic retention mechanisms (*see section 2.2.7*). It is hypothesised that initially nanoparticles get deposited on the grain surface mainly due to surface interaction potentials that are based on DLVO theory and kinetic energies of particles. Bentheimer sandstone is largely composed of quartz that is negatively charged. Freely moving cations present in the brine are attracted towards these grains. The overall charge on the grain surface reduces. When silica nanoparticles that are also negatively charged flowing at high velocities collide with the grain surface, overcoming the net repulsive energy barrier, they get attached to the grain surface. This could explain the linear decline in injectivity in the first phase. As more and more nanoparticles are deposited on grains, effective pore size

reduces which initiates plugging of pore throats by incoming nanoparticles. This is when phase B starts. During this phase, it is hypothesized that both surface deposition and plugging are taking place. Nanoparticles may also get retained by forming bridges which could result in pore throat plugging as well. Small pore throats would be plugged first which would result in increasing tortuosity of the porous medium as the number of interconnections between pore bodies would reduce. This could explain the increase in the slope of injectivity decline in this phase compared to phase A. Due to plugging and surface deposition, smaller pore throats get completely clogged whereas bigger pore throats remain open. Consequently, it is further hypothesized that the pressure drop across the retained nanoparticles in plugged pore throats could become large enough to unplug them. Also, interstitial velocity would increase due to plugging and deposition. Nanoparticles that are flowing at these high interstitial velocities when collide with retained nanoparticles, may release them. This is when phase C starts. In this phase, entrainment mechanism equilibrates effects of surface deposition and plugging due to release of retained nanoparticles. Flow in this phase would largely take place from preferred large open channels. This could explain constant injectivity observed in phase C. In *Figure 5-17* a simple illustration is made to depict retention of nanoparticles during phase A where surface deposition predominantly takes place, phase B where both surface deposition and plugging mainly take place and phase C where all three retention mechanisms i.e. surface deposition, plugging and entrainment simultaneously take place.

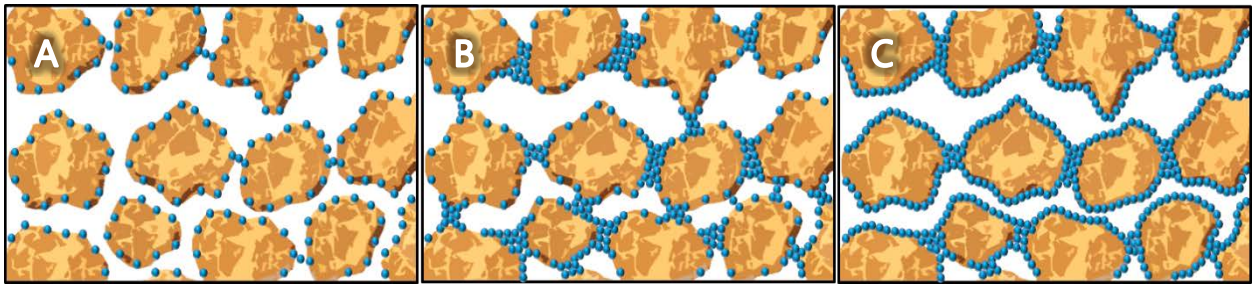

Figure 5-17: Simplified depiction of retention of nanoparticle at pore scale during phase A (left), B (middle) and C (right)

Another prominent feature of experiments CF-2, 3 and 4 is the maximum injectivity decline. All flow parameters were kept same except CF-3 had a lower colloidal concentration of 50 ppm instead of 100 ppm. In terms of rock properties, permeability of all three core plugs were different i.e. CF-2 < CF-3 < CF-4 (*see Table 5-5*). Higher permeability represents less resistance to flow, that could be interpreted as the availability of bigger sized flow channels. Only looking at the first phase-A, where surface deposition is dominant, it can be seen that similar injectivity decline was observed i.e. ~10% in all three experiments (*see Figure 5-16*). But in phase-B, where plugging is dominant, injectivity decline is different for all three experiments. This is because plugging is inversely proportional to the size of flow channels. Therefore, it could be argued that in nanoparticle flow through porous media, retention mechanisms are relatively less effected by the colloidal concentration but are more sensitive to the initial permeability of the medium given all other parameters are kept same.

In experiment CF-2a, when flow was reversed after reaching stable permeability in CF-2, only 2.2% of the initial permeability was recovered after which permeability became stable again. This shows that some of the nanoparticles that were loosely plugged in CF-2 got released, recovering permeability of the medium. Therefore, it is hypothesized that damage induced by nanoparticle retention is not considerably dependent on flow direction.

In experiment CF-3a, when the colloidal concentration was increased to 100 ppm after reaching stable permeability with a colloidal concentration of 50 ppm in CF-3, only 2.7% of the initial permeability was further damaged after which permeability became stable again. This could be described based on the earlier discussed hypothesis of retention mechanisms. Once permeability is stabilized, it could be assumed that all available retention sites are occupied. Flow mainly takes place from unplugged channels. In these channels, surface deposition did take place earlier but was not sufficient for plugging to have an effect. Negatively charged deposited nanoparticles acts as a coating layer on the grains that result in net repulsive force between grain and approaching dispersed nanoparticles. Hence, increasing concentration may not aid in increasing surface deposition but, could result in increased plugging. When multiple nanoparticles approach a pore throat smaller than the collective size of nanoparticles at the same time, they could result in plugging. Increasing colloidal concentration therefore, increases the probability of multiple particle pore throat plugging as shown in *Figure 5-18*. Therefore, it is hypothesized that additional permeability damage might have been caused by primarily plugging mechanism.

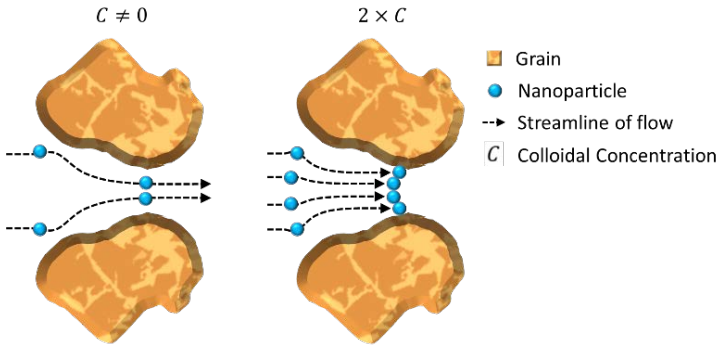

Figure 5-18: Simple pore scale illustration of multiple particle pore throat plugging at different colloidal concentration

In experiments CF-5 and 6, colloidal pH was kept outside the stable range which was obtained from silica nanoparticle stability analysis i.e. 6.5 to 8.5 (*see section 4.3.3*). Results obtained from these experiments complimented stability analysis and were expected. These results showed that if injected colloid is not kept within the stable range, nanoparticles aggregate and behave as a large sized particles and the external filter cake is formed. In EFC, wormholes were found which are assumed to be connected with high permeable channels. Apart from EFC formation, there was another prominent feature observed in these two experiments i.e. the slope of injectivity decline. All flow parameters except pH of injection fluid, were kept same. The permeability of the core plug used for CF-5 was ~4% more than CF-6. Contrary to that, looking at 400 PVI, injectivity decline in CF-5 was ~25% more than CF-6. This extra decline is attributed to the sensitivity of clay minerals to high pH fluids (*see section 2.2.4.2*). Therefore, in CF-5, main factors contributing to injectivity decline are both

aggregation of nanoparticles and sensitivity of clay minerals to high pH fluids. In experiment CF-6a, pH of colloid was brought from 4 to 7.3 which is within the stable range. Changing the pH resulted in recovering permeability. This is because EFC was slowly wiped out due to nanoparticle's increase in zeta potential value. Traces of EFC developed in CF-6 can be seen in *Figure 5-13* right.

Moreover, a mass balance was carried out for the EFC formed in CF-5. This was done to find out if prediction can be made for the thickness of external filter cake. As experienced in CF-7, initially internal filter cake forms and after some stage or transition time [62] external filter cake starts to develop. It is widely agreed that once EFC starts to form, very few particles make their way into the porous medium especially in the case where dispersed particles form uncompressible EFC [11, 16, 17, 20, 27, 39, 53, 62-65]. Mass balance approach works by locating the transition time from the experimental result and using the fluid volume injected after transition time to calculate mass of injected particles. Knowing the cross-sectional area of the core plug, thickness of the filter cake can be predicted. For CF-5, pressure drop profile indicates that external filter cake started to form right from the beginning of the experiment. Therefore, the volume of fluid injected was accounted from beginning till the end of experiment. Thickness calculation showed 0.37 mm thick filter cake (*see Appendix C*).

$$M_{colloid_{inj}} = Volume_{inj}.Concentration_{colloid} = 26.2l \times 0.1gl^{-1} = 2.62g$$

$$M_{Colloid_{EFC}} = Area_{x-sec}.Thickness_{ECF}.Density_{colloid} = 11.61cm^2 \times 3.7E^{-2} \times 2.65gcm^{-3} = 1.14g$$

This shows that mass accumulated at EFC is less than half of what was injected. This mismatch is due to following reasons. EFC formed by silica nanoparticles is very compressible and unconsolidated. There are worm holes in the filter cake which indicate that not all nanoparticles are retained at the injection face but are also flowing through the core.

In experiment CF-7, there was a fracture along the core and iron ions were formed in the injection fluid due to oxidation of an iron washer in the injection bucket. EFC was found on the injection face which corresponds to the presence of bigger particles. Hence, four samples were prepared to investigate the stability of injection fluid using 0.1M Iron sulphate hepta-hydrate and 0.1M iron chloride tetra-hydrate dissolved in the same colloid used in CF-7 as shown in *Figure 5-19*. It was observed that presence of iron ions significantly reduced the pH of the fluid and iron oxide was formed. Average hydrodynamic size and mean zeta potential measurements were carried out which showed that injection fluid was not stable due to the presence of iron oxide and dispersed particles were an order of magnitude bigger than silica nanoparticles as shown in *Table 5-6*.

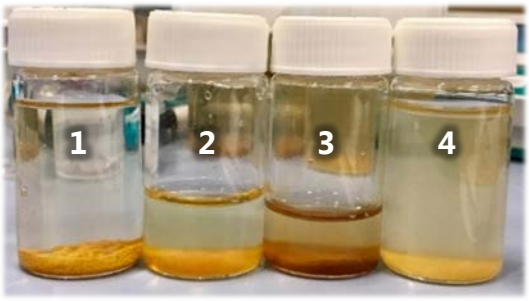

Figure 5-19: Samples prepared with CF-7's colloid and iron salts

S. No.	Sample Containing	Size *[d.µm]*	Zeta Ptnl. *[mV]*
1	Iron sulfate hepta-hydrate (0.1M Fe^{+2})	16	+0.1
2	Iron sulfate hepta-hydrate (0.1M Fe^{+2}) [*filtered using 0.45µm filter*]	1.3	+2.1
3	Iron chloride tetra-hydrate (0.1M Fe^{+2}) [*filtered using 0.45µm filter*]	0.3	+11.9
4	Iron chloride tetra-hydrate (0.1M Fe^{+2})	8	+6.3

Table 5-6: Size and zeta potential measurements for samples containing iron particles

In all the experiments conducted in this study, it can be seen that permeability reduction was significantly more near injection face and relatively less towards the outlet of the core plug. This attribute of particulate flow through porous media is encountered in almost all core flood experiments present in literature where suspension or colloid is injected into a porous medium. Following explanation is presented to explain this phenomenon. Consider a porous media consisting of different sized interconnected cylindrical flow channels divided into two equal sections as shown in *Figure 5-20*.

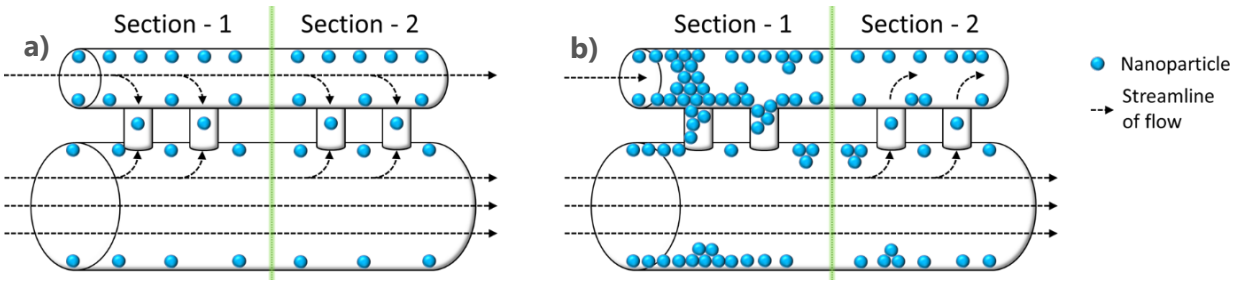

Figure 5-20: Assumed depositional model of porous media showing two sections i.e. section-1 near injection face and section-2 near outlet of porous media, a) at $t > t_0$, b) at $t \gg t_0$

Once the colloid injection is commenced in a virgin porous medium, surface deposition starts to take place. This would cause thinning of flow channels, first in section-1 at some time $t > t_0$. Smaller channels in section-1 would get plugged eventually at some time $t \gg t_0$ resulting in higher permeability damage in section-1 than section-2. Consequently, higher pressure drop would be observed near injection face compared to the outlet.

5.6 Model Validation

Core plug and flow parameters used in experiments CF-2 through 4 were used as input parameters in the presented model and the results were generated. *Figure 5-21* shows the experimental and model predicted normalized permeability curves. Model results were found to be in good agreement with experimental results. The root mean square error associated with the match between the experimental and model predicted results for normalized permeability were found to be less than 2%. All three phases discussed earlier are clearly visible from the normalized permeability curve. The values of coefficients used in the model to predict injectivity decline are tabulated in *Table 5-7*.

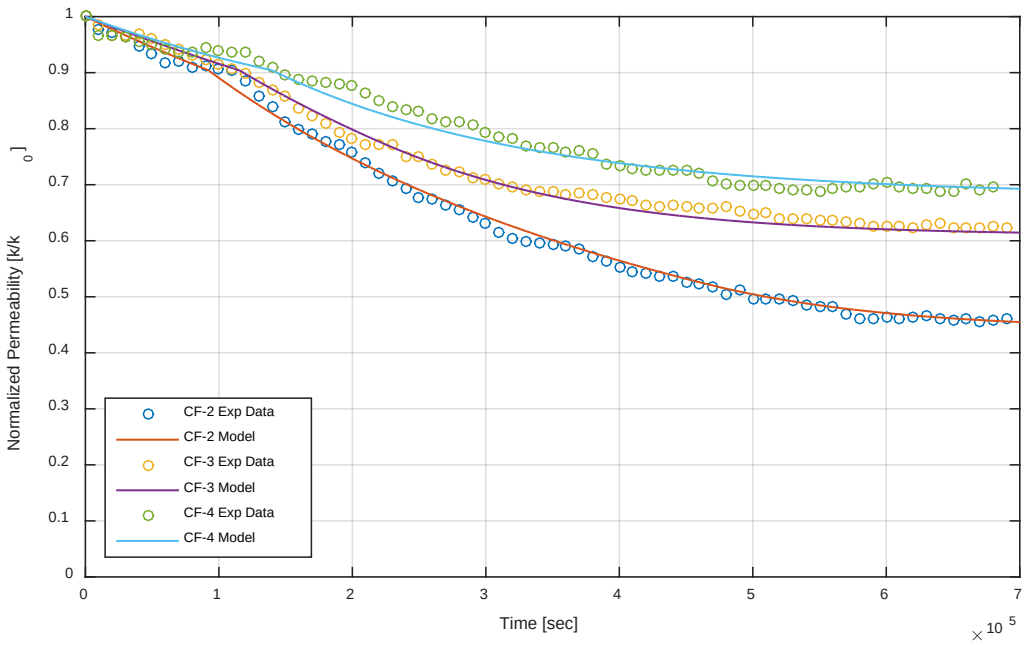

Figure 5-21: Model predicted normalized permeability curves for experiment CF-2, 3 and 4

Exp. No.	k_0 [m^2]	C_0	β	σ_{cr}	v_{cr} [m/s]	α [s^{-1}]	λ [m^{-1}]	ψ [m^{-1}]	RMS Error
CF-2	2.59e-12	100e-6	2.0e3	5.30e-5	8.840e-3	2.50e-5	2.50e-3	2.50e-1	1.3%
CF-3	2.93e-12	50e-6	2.0e3	5.30e-5	8.828e-3	4.00e-5	4.00e-3	4.00e-1	1.2%
CF-4	3.17e-12	100e-6	2.0e3	5.30e-5	8.813e-3	1.90e-5	1.90e-3	1.90e-1	1.7%

Table 5-7: Values of coefficients used in presented model

Formation damage coefficient β and critical retained colloidal concentration σ_{cr} was found to be same for all three experiments. For a given type of sandstone and particles, aforementioned particles remain same regardless of the change in colloidal concentration and initial permeability of rock. Critical velocity v_{cr} was found to be inversely proportional to initial permeability.

Retention rate function $\frac{\partial \sigma}{\partial t}$ (equation-4) used in the presented model has three distinct terms (*see section 3.1.2.3*). First two terms $\alpha \varphi c$ and $\lambda u c$ contribute to retention of particles and the last term $\psi(|v| - v_{cr})^{+}\sigma$ balances their effect due to entrainment of retained particles. It was found that for a given system, all three terms of retention rate function should have the same order of magnitude for reaching stable permeability. Model predicted results showed that retention rate coefficients i.e. surface deposition, plugging and entrainment (if written in scientific notation) were found to have the same coefficient with increasing exponent with an order of magnitude two. This reduces the complexity of finding each retention coefficient separately for a given system.

Retention coefficients were also found to have an inversely proportional relation with initial permeability. This could be explained based on the discussion presented earlier. Low permeability indicates more resistance to flow which could be interpreted as smaller channels for flow. Smaller channels can more easily retain particles than bigger channels.

6 Conclusions

In this study, experiments were carried out to investigate injectivity decline due to ultra-filtered water injection into porous media. Following conclusions could be drawn from the experiments.

- Stability analysis of colloid is critical while dealing with nanoparticles.
- For a given pH of brine, with an increase in dissolved salt concentration, the stability of dispersed nanoparticles decreases. For a given dissolved salt concentration in brine, there exists a stable pH range in which dispersed nanoparticles are stable i.e. ~6.5 to 8.5.
- As silica nanoparticles are an order of magnitude 2 smaller in size than pore size distribution of Bentheimer sandstone, hence the duration of experiment has to be long i.e. >25000 PV to capture entire retention mechanisms.
- Frequent disturbance in injection rate would result in lower injectivity decline.
- No external filter cake develops in the flow of nanoparticles through porous media provided colloid is stable. Only deep bed filtration takes place where three main retention mechanisms dominate i.e. surface deposition, plugging and entrainment.
- Increase in colloidal concentration does not significantly effects surface deposition phase but could result in increased plugging of porous media.
- Injectivity decline in colloidal flow through porous media is strongly related to the initial permeability of porous media.
- Retained nanoparticles are largely permanent as flow reversal did not result in significant permeability recovery.
- If colloid is injected into a porous media in unstable pH conditions, injectivity decline is drastic as nanoparticles aggregate and act as micron-sized particles. This results in the formation of external filter cake which contains wormholes connected to high permeable channels of porous media.
- External filter cake formed by nanoparticles due to unstable pH of colloid is not permanent and could be removed by bringing pH of colloid back into stable range.
- Presence of iron particles in injected fluid results in drastic injectivity decline even if there exists a fracture in the porous media.
- Permeability damage is always more near the injection face in particulate flow through porous media than the outlet.
- The model presented in this study takes into account all three major retention mechanisms and was found to be in good agreement with experimental results.
- Maximum permeability reduction observed was about 50%, this shows that frequency of stimulation jobs can be reduced or completely avoided by implementing ultrafiltration on water injection wells.

7 Recommendations

Based on the results of this study, following recommendations are made.

- Experiments in this study have shown that retention rate is dependent on the permeability of porous media. Further experimental studies on nano-particulate flow through low to medium permeable porous mediums could give better understanding of this dependence.
- Bentheimer sandstone is a homogeneous sandstone i.e. ~95% composed of quartz which is not the case in most of the reservoirs which suffer from injectivity decline, therefore, it is recommended to conduct experiments on rocks of different compositions.
- Different nanoparticles such as fly-ash (negatively charged) or Hematite nanoparticles (positively charged) could also be used in core flood experiments to confirm the behavior observed in this study.
- Silica nanoparticles in sandstone have poor optical resolution hence nanoparticles which could be detected by CT scanner might be used to complement deposition profiles computed from pressure drop data.
- In this study, synthetic ultra-filtered water was used with high concentrations of dispersed nanoparticles which is an exaggeration of what is expected from ultrafiltration. At the same time, the permeability of the sandstone used was too high that is not normally found in actual reservoirs. Therefore, it is expected that overall behavior might remain same if actual ultra-filtered water with more realistic permeability rock is used. To confirm or deny this, it is recommended to perform experiments with actual ultra-filtered water with realistic permeability rocks.

Nomenclature

CF Core-Flood
DBF Deep Bed Filtration
DLS Dynamic Light Scattering
DLVO Derjaguin & Landau, 1941 and Verwey & Overbeek, 1948 - Theory of colloidal stability
DSW Diluted Sea Water
EFC External Filter-Cake
EOR Enhanced Oil Recovery
FWI Fresh Water Injection
GWPC Ground Water Protection Council
IFC Internal Filter-Cake
IOGP International association of Oil and Gas Producers
IOR Improved Oil Recovery
LDV Laser Doppler Velocimetry
MIP Mercury Intrusion Porosimetry
NETL National Energy Technology Laboratory
PALS Phase Analysis Light Scattering
PEEK Poly Ether Ether Ketone
pH Potential of Hydrogen
PSD Pore Size Distribution
PV Pore Volume
PVI Pore Volume Injected
PWI Produced Water Injection
PWRI Produced Water Re-Injection
pzc Point of Zero Charge
SEM Scanning Electron Microscopy
SWI Sea Water Injection
TDS Total Dissolved Solids
TEM Transmission Electron Microscopy
TSS Total Suspended Solids
UKCS United Kingdom Continental Shelf
XRD X-Ray Diffraction
XRF X-Ray Flourocense

Appendix A

Transport Equation and Solution

Mass Balance for Conservation Equation

Consider that the flow is one dimensional, in x-direction and taking place in a core plug of cross sectional area A having porosity $\varphi(x,t)$ and dimensions $\Delta x, \Delta y, \Delta z$. Now let $c(x,t)$ be the concentration of silica nanoparticle in colloidal suspension measured in volume fraction of the injected fluid of density ρ. Let $Q(x,t)$ denote the flux i.e. the colloidal suspension mass crossing a cross section in a given time. Due to the flow of colloidal suspension through porous medium, some of the silica nanoparticles will get retained in the medium. Let $\sigma(x,t)$ be the concentration of the retained silica nanoparticles measured in volume fraction of porous medium. Finally, let u be the Darcy's superficial velocity at which colloidal suspension is flowing through the porous medium which is constant.

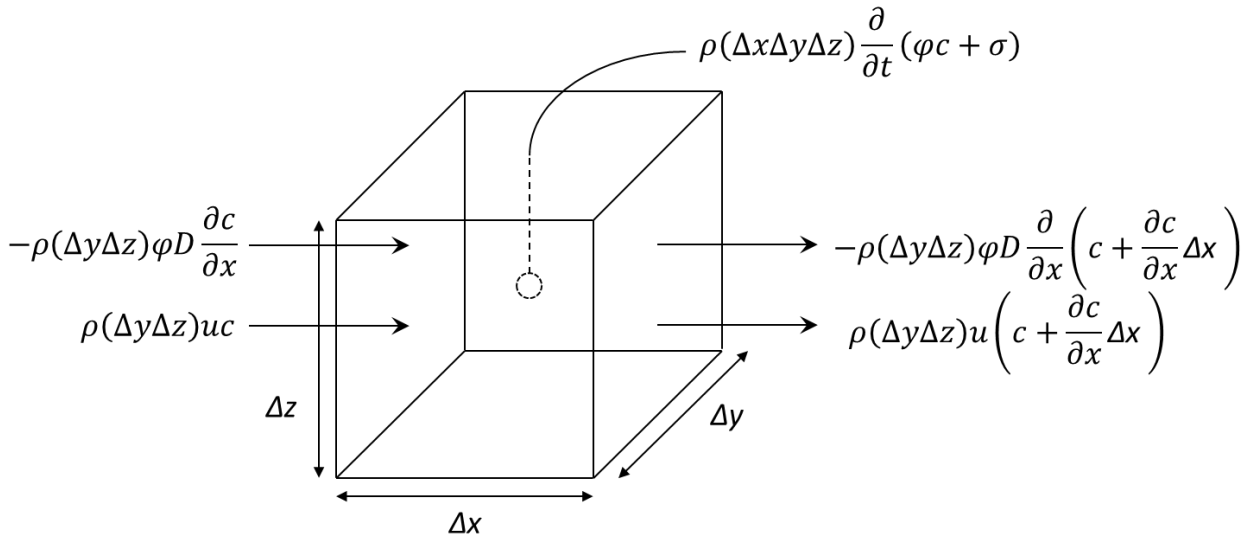

Total flux entering the control volume in a given time is given by

$$Q_{in}=\rho(\Delta y\Delta z)\left(uc-\varphi D\frac{\partial c}{\partial x}\right)$$

Total flux leaving the control volume in a given time is given by

$$Q_{out}=\rho(\Delta y\Delta z)\left(u\left(c+\frac{\partial c}{\partial x}\Delta x\right)-\varphi D\frac{\partial}{\partial x}\left(c+\frac{\partial c}{\partial x}\Delta x\right)\right)$$

Total flux accumulating in the control volume in a given time is given by

$$Q_{accumulated}=\rho(\Delta x\Delta y\Delta z)\frac{\partial}{\partial t}(\varphi c+\sigma)$$

Where Q and D are the colloidal flux and hydrodynamic dispersion coefficient. According to the mass conservation

$$\sum m_{in} - \sum m_{out} = \sum m_{accumulated}$$

$$\rho(\Delta y \Delta z)\left(uc - \varphi D\frac{\partial c}{\partial x}\right) - \rho(\Delta y \Delta z)\left(u\left(c + \frac{\partial c}{\partial x}\Delta x\right) - \varphi D\frac{\partial}{\partial x}\left(c + \frac{\partial c}{\partial x}\Delta x\right)\right)$$
$$= \rho(\Delta x \Delta y \Delta z)\frac{\partial}{\partial t}(\varphi c + \sigma)$$

Dividing the whole equation with $\rho(\Delta y \Delta z)$

$$uc - \varphi D\frac{\partial c}{\partial x} - uc - \Delta x u\frac{\partial c}{\partial x} + \varphi D\frac{\partial c}{\partial x} + \Delta x \varphi D\frac{\partial^2 c}{\partial x^2} = \Delta x\frac{\partial \varphi c}{\partial t} + \Delta x\frac{\partial \sigma}{\partial t}$$

$$-\Delta x u\frac{\partial c}{\partial x} + \Delta x \varphi D\frac{\partial^2 c}{\partial x^2} = \Delta x\frac{\partial \varphi c}{\partial t} + \Delta x\frac{\partial \sigma}{\partial t}$$

Dividing the whole equation with Δx, and rearranging yields the final transport equation

$$-\varphi D\frac{\partial^2 c}{\partial x^2} + u\frac{\partial c}{\partial x} + \frac{\partial \varphi c}{\partial t} + \frac{\partial \sigma}{\partial t} = 0$$

Solution for Explicit Model for Deep Bed Filtration

The governing equation comes from mass balance and kinetic equation and is given by

$$-D\varphi\frac{\partial^2 c}{\partial x^2} + u\frac{\partial c}{\partial x} + \frac{\partial \varphi c}{\partial t} + \frac{\partial \sigma}{\partial t} = 0 \tag{15}$$

The system under investigation is one dimensional and the porosity of the porous medium is changing with time due to retention of particles. The relationship of change in retention concentration is given by

$$\frac{\partial \sigma}{\partial t} = \alpha\varphi c + \lambda u c - \psi(|v| - v_{cr})^{+}\sigma \tag{16}$$

In the change of retention function, the first term caters the adsorption, the second term accounts for plugging of the particles in the porous media and the third term is responsible for the entrainment. In the first term of equation 16, α is the pore surface deposition coefficient. The adsorption rate of particles show direct proportionality between retention rate and concentration of colloids in suspended state and the fraction of volume available. This means, due to adsorption, the effective porosity would reduce and hence retention concentration would increase. A time would come when some of the pore throats would become small enough for plugging to take place.

In the second term, λ is the pore throat plugging coefficient which is proportional to superficial velocity and dispersed colloidal concentration which is given by

$$\lambda = \begin{cases} \lambda\ , & \sigma > \sigma_{cr} \\ 0\ , & otherwise \end{cases} \tag{17}$$

This means that plugging will only occur if the retained colloids concentration σ gets bigger than some critical retained colloids concentration σ_{cr}. Hence, due to adsorption, retained

colloidal concentration at some stage would result in reducing the flow path to an extent where dispersed colloids could get directly plugged.

In the third term of equation 16, ψ represents entrainment coefficient of retained particles by flowing phase when the interstitial velocity v becomes larger than some critical interstitial velocity v_{cr}. This term shows direct proportionality of retention rate to the retained colloidal concentration and the difference between the interstitial and some critical interstitial velocity necessary for retained particle's mobilization. This means, due to adsorption and plugging, a stage would come when the interstitial velocity variations would become large enough to release the retained colloids. Entrainment coefficient is given by

$$\psi = \begin{cases} \psi, & |v| > v_{cr} \\ 0, & otherwise \end{cases} \tag{18}$$

The interstitial velocity would change with change in porosity due to retention of nanoparticles in the porous media. The porosity reduction is given by

$$\varphi(\sigma) = \varphi_0 - \int_0^t \frac{\partial \sigma}{\partial t} dt \tag{19}$$

Hence, the interstitial velocity reduction is given by

$$v = \frac{u}{\varphi_0 - \sigma} \tag{20}$$

Initial and Boundary Conditions:

Considering core flood experiments, at initial state the core plug is free of suspended and retained colloid concentration hence the initial condition given in equation-21. The injection face of the core is supplied by constant inlet colloidal flux that results in Robin boundary condition (equation-22) which after discretization becomes simply $c(0,t) = c_{inj}$ shown later in equation-28. At the end of the core plug, there is no change in concentration hence Neumann boundary condition (equation-23).

Initial conditions:

$$c(x, t=0) = 0 \quad and \quad \sigma(x, t=0) = 0 \tag{21}$$

Boundary conditions:

$$\begin{gathered} uc_{inj}(0,t) = uc - D\varphi \frac{\partial c}{\partial x} \quad \Rightarrow \quad c(0,t) = c_{inj} \\ \frac{\partial c}{\partial x}(L,t) = 0 \end{gathered} \tag{22}$$

Discretization

To discretize the governing equation-15, Finite difference scheme was adopted to discretize in spatial domain and Euler forward (Explicit) for time integration. An assumption is made

that the change in retention concentration of nanoparticles over single time step is too small and hence change in porosity over one time step is negligible. Retention concentration for each time step is calculated separately and porosity is updated which gives new interstitial velocity.

First term:

$$-D\varphi\frac{\partial^2 c}{\partial x^2} = -D\varphi_i^n\left[\frac{c_{i-1}^n - 2c_i^n + c_{i+1}^n}{\Delta x^2}\right] \tag{23}$$

Second term:

$$u\frac{\partial c}{\partial x} = u\left[\frac{c_i^n - c_{i-1}^n}{\Delta x}\right] \tag{24}$$

Third term: [assuming $\frac{\partial\varphi}{\partial t}\Big|_t^{t+1} = 0$]

$$\frac{\partial\varphi c}{\partial t} = \frac{\partial\varphi c}{\partial\varphi}\frac{\partial\varphi}{\partial t} + \frac{\partial\varphi c}{\partial c}\frac{\partial c}{\partial t}$$
$$\frac{\partial\varphi c}{\partial t} = \varphi_i^n\left[\frac{c_i^{n+1} - c_i^n}{\Delta t}\right] \tag{25}$$

Fourth term:

$$\frac{\partial\sigma}{\partial t} = \alpha\varphi_i^n c_i^n + \lambda u c_i^n - \psi(v(\sigma_i^n) - v_{cr})\sigma_i^n \tag{26}$$

Now combining equations-23 through 26 together, equations for finding concentration in each cell at next time step can be derived.

For Cell i:

$$-D\varphi_i^n\left[\frac{c_{i-1}^n - 2c_i^n + c_{i+1}^n}{\Delta x^2}\right] + u\left[\frac{c_i^n - c_{i-1}^n}{\Delta x}\right] + \varphi_i^n\left[\frac{c_i^{n+1} - c_i^n}{\Delta t}\right] + \alpha\varphi_i^n c_i^n + \lambda u c_i^n - \psi(v(\sigma_i^n) - v_{cr})\sigma_i^n = 0$$

$$c_i^{n+1} = \frac{\psi(v(\sigma_i^n) - v_{cr})\sigma_i^n + c_{i-1}^n\left[\frac{D\varphi_i^n}{\Delta x^2} + \frac{u}{\Delta x}\right] - c_i^n\left[\frac{2D\varphi_i^n}{\Delta x^2} + \frac{u}{\Delta x} - \frac{\varphi_i^n}{\Delta t} + \alpha\varphi_i^n + \lambda u\right] + c_{i+1}^n\left[\frac{D\varphi_i^n}{\Delta x^2}\right]}{\left(\frac{\varphi_i^n}{\Delta t}\right)} \tag{27}$$

For Cell 1:

Considering boundary condition given in equation-21 and discretizing it to find colloidal concentration at the fictitious inlet boundary.

$$uc_{inj} = uc_1^n - D\varphi_1^n\left[\frac{c_1^n - c_0^n}{\Delta x}\right] = uc_1^n - c_1^n\left[\frac{D\varphi_1^n}{\Delta x}\right] + \overbrace{c_0^n}^{c_{inj}}\left[\frac{D\varphi_1^n}{\Delta x}\right]$$
$$c_1^n\left[u - \frac{D\varphi_1^n}{\Delta x}\right] = c_{inj}\left[u - \frac{D\varphi_1^n}{\Delta x}\right] \tag{28}$$
$$c_1^n = c_{inj}$$

Therefore,

$$c_1^{n+1} = c_{inj} \tag{29}$$

For Cell N:

Similarly for cell N we get

$$c_N^{n+1} = \frac{\psi(v(\sigma_N^n) - v_{cr})\sigma_N^n + c_N^n\left[\frac{D\varphi_N^n}{\Delta x^2} + \frac{u}{\Delta x}\right] - c_N^n\left[\frac{D\varphi_N^n}{\Delta x^2} + \frac{u}{\Delta x} - \frac{\varphi_N^n}{\Delta t} + \alpha\varphi_N^n + \lambda u\right]}{\frac{\varphi_N^n}{\Delta t}} \tag{30}$$

In equation-27, 29 and 30 all the terms are known and hence colloidal concentration for the next time step can be calculated.

For σ, φ *and* v:

Retention concentration σ_i, porosity φ_i and interstitial velocity v_i are updated at each time step by discretising equation-26.

$$\frac{\partial\sigma}{\partial t} = \frac{\sigma_i^{n+1} - \sigma_i^n}{\Delta t} = \alpha\varphi_i^n c_i^n + \lambda u c_i^n - \psi(v(\sigma_i^n) - v_{cr})\sigma_i^n$$
$$\sigma_i^{n+1} = \Delta t(\alpha\varphi_i^n c_i^n + \lambda u c_i^n - \psi(v(\sigma_i^n) - v_{cr})\sigma_i^n) + \sigma_i^n \tag{31}$$

Now porosity at next time step can be calculated by discretizing equation-19 and 31.

$$\varphi_i^{n+1} = \varphi_0 - \sigma_i^{n+1} \tag{32}$$

And velocity from equation-20, 31 and 32.

$$v_i^{n+1} = \frac{u}{\varphi_0 - \sigma_i^{n+1}} \tag{33}$$

Permeability Reduction Model

Permeability of the porous medium is reduced due to deposition of colloids in the pores and throats of the medium. Permeability damage induced by the deposition of colloids in the porous medium taking into account the harmonic average of the plugged and unplugged parts of the porous medium given as

$$k(\sigma) = \frac{k_0}{1 + \beta\sigma} \tag{34}$$

Where $k(\sigma)$ is the permeability reduction function, k_0 is the initial absolute permeability of the porous medium and β is the empirical parameter commonly known as formation damage factor.

Injectivity Decline

Quality of injection is normally given by the non-dimensional normalized injectivity index II. Injectivity is defined as the ratio of volumetric injection flowrate to the pressure difference. Normalized injectivity index is then the ratio between the initial and current injectivity

indexes which is equal to normalized permeability if flow rate and viscosity are kept constant i.e. in this study.

$$II = \frac{II_t}{II_0} = \frac{q_t \Delta P_0}{q_0 \Delta P_t} = \frac{k_t}{k_0} \tag{35}$$

Pressure gradient is related to permeability of the porous medium through Darcy's law

$$u = -\frac{k(\sigma)}{\mu_s} \Delta P \tag{36}$$

Where μ_s is the viscosity of injected colloid. Generalized Einstein's equation for viscosity is used to calculate the alteration in viscosity of the colloidal suspension

$$\mu_s = \mu_b(1 + 2.5c) \tag{37}$$

Where, μ_b is the viscosity of the carrier fluid (brine).

Flow Chart for Injectivity Decline (DBF Model)

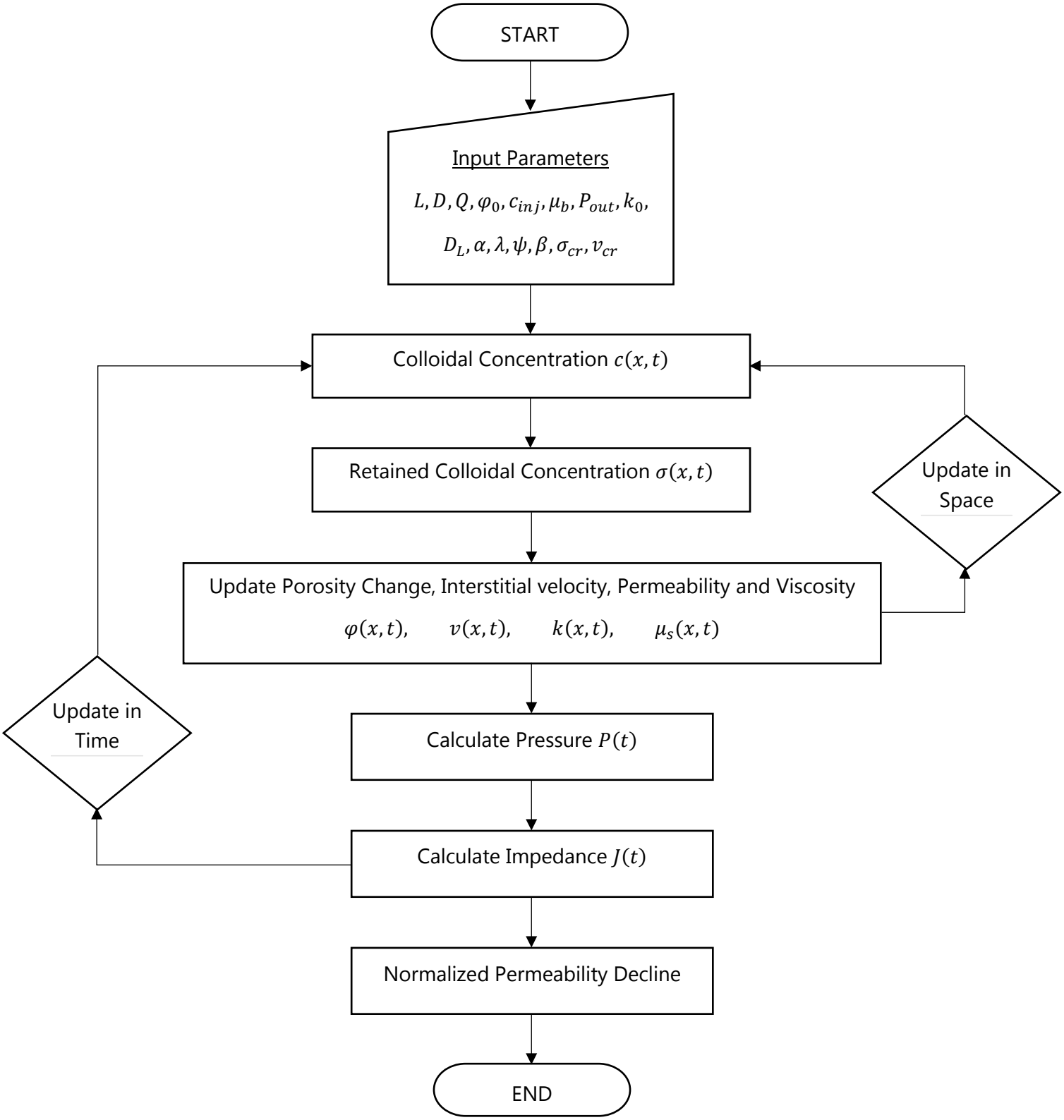

Appendix B

Picture of Experimental Setup

Mercury Intrusion Porosimetry

Mercury Intrusion Porosimetry (MIP) test has been performed to find the pore size distribution of Bentheimer sandstone. Micromeritics AutoPore IV (Mercury Porosimeter) was used to perform the test. Penetrometer was used for taking measurements as shown in *Figure B-1*. The penetrometer is made of glass (which acts as an insulator) and filled with mercury (that acts as a conductor). The stem of the penetrometer is a capillary that acts as a reservoir for the analytical volume of mercury. The stem is plated with metal (also a conductor). The two conductors, mercury, and the metal plating, are separated by glass, thus forming a coaxial capacitor. As pressure forces mercury out of the capillary and into the sample, the mercury inside the capillary decreases and so is the capacitance. The decrease in capacitance, therefore, is proportional to the volume of mercury leaving the capillary with each change in pressure.

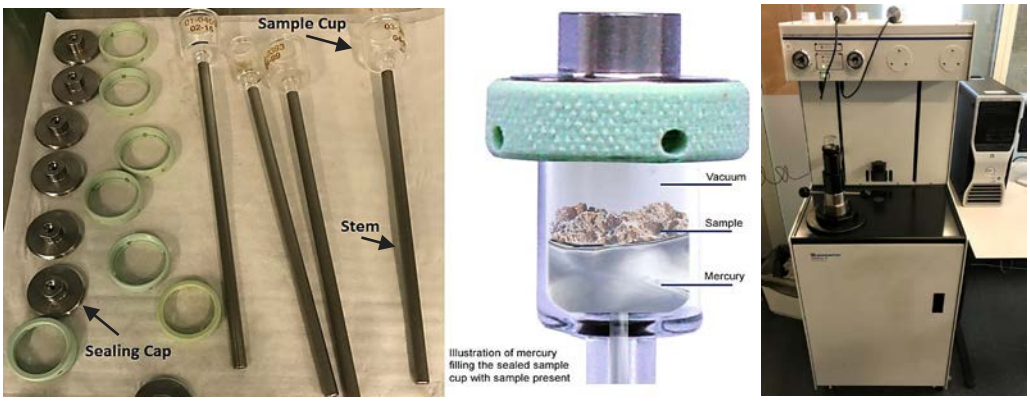

Figure B-1: Left: Penetrometer used for Mercury Intrusion Porosimetry, Right: Micromeritics AutoPore IV (Mercury Porosimeter)

A sample of the Bentheimer sandstone was taken from the same block from which core plugs (used in injection experiments) were drilled. This sample was then broken into small pieces to increase the surface area for mercury intrusion. Prior to MIP test, sample was placed in the oven for 24hrs at 60°C. Then the sample was placed in the vacuum chamber for 24hrs to ensure no air remains in the sample. At this stage the sample is free of moisture and air and ready to be tested. After ensuring that there is no moisture and air in the sample, it is placed in the penetrometer's sample cup. The Penetrometer is then placed in the MIP machine and vacuumed to evacuate any air, while still evacuating, mercury is allowed to fill in the sample cup. Next, pressure is increased towards atmospheric value while the volume of mercury entering the large openings in the sample is being monitored. After pressure reaches atmospheric value, pores of about 12mm are believed to be filled by mercury. Penetrometer is then placed in the pressure vessel for the remainder of the test. Pressure is then increased in a step by step manner till maximum pressure of 212MPa. For each pressure step corresponding pore diameter range is calculated using Washburn's equation shown below.

$$D = -\frac{4\gamma cos\theta}{P}$$

Value of $\theta = 141°$, $\gamma = 485\ dynes.cm^{-1}$. The changes in volume of mercury can be observed visually, but measurements are done using electronic means of detecting the rise and fall of mercury within the capillary which are much more sensitive, providing even greater volume sensitivity down to less than a microliter. All the measurements of pressure, cumulative volume of mercury intruded and corresponding pore diameter range are recorded. After maximum pressure of 212MPa, pressure is reduced and mercury leaves the pores called extrusion process. This process is also recorded.

Below is the plot for pore size distribution deduced from the raw data obtained from MIP test.

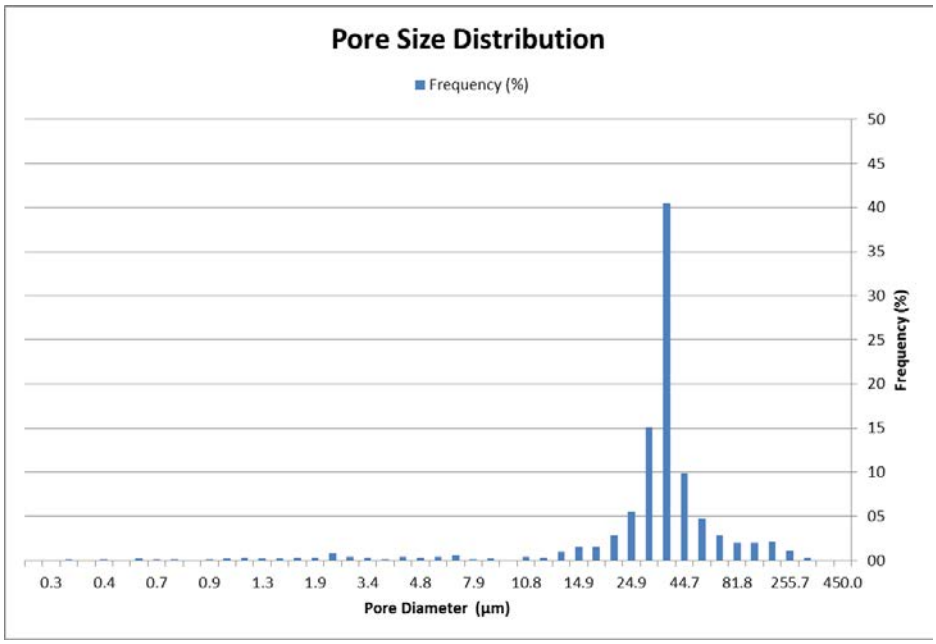

Figure B-2: Penetrometer used for Mercury Intrusion Porosimetry

XRD/XRF Analysis of Bentheimer Sandstone

XRD and XRF test fro bentheimer sandstone was conducted in X-Ray Diffraction facilities in Material Science and Engineering TU Delft Faculty.

Experimental conditions for XRF:

- For XRF analysis the measurements were performed with a Panalytical Axios Max WD-XRF spectrometer and data evaluation was done with SuperQ5.0i/Omnian software.

	Compound Name	Conc. wt(%)	Absolute Error (%)
1	SiO2	95.915	0.1
2	Al2O3	3.127	0.05
3	K2O	0.538	0.02
4	Fe2O3	0.161	0.01
5	TiO2	0.096	0.009
6	Na2O	0.047	0.006
7	Cl	0.027	0.005
8	P2O5	0.022	0.004
9	Cr2O3	0.017	0.004
10	SO3	0.015	0.004
11	CaO	0.013	0.003
12	Ta2O5	0.01	0.003
13	ZrO2	0.005	0.002
14	ZnO	0.004	0.002
15	PbO	0.003	0.002

Figure B-3: XRF result for Bentheimer sandstone

Experimental conditions for XRD:

- Sample: The sample is powdered with mortar and pestle.
- Specimens: A thin layer of sample powder was deposited on a Si510 wafer from a powder-ethanol suspension and fixed in PMMA sample holder L510.
- Experimental Instrument: Bruker D8 Advance diffractometer Bragg-Brentano geometry and Lynxeye position sensitive detector. Cu Ka radiation. Divergence slit V12, scatter screen height 5 mm, 45 kV 40 mA. Sample spinning. Detector settings: LL 0.11, W 0.14.
- Measurement: Coupled θ -2θ scan 10° - 90°, step size 0.034 ° 2θ, counting time per step 2 s.
- Data evaluation: Bruker software DiffracSuite.EVA vs 4.2.

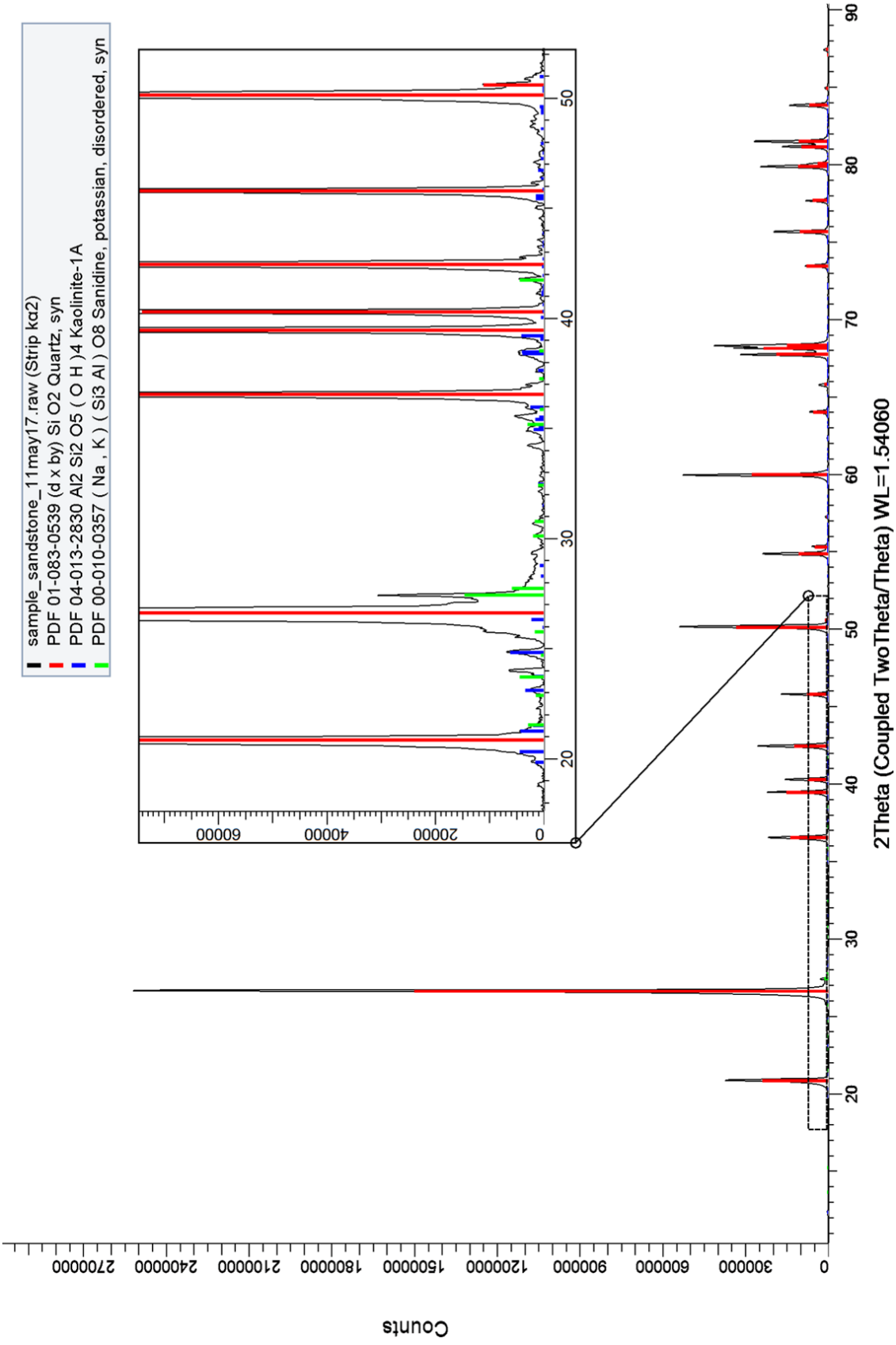

Figure B-4: XRD result for Bentheimer sandstone

Appendix C

Experiment CF-8 - Unsuccessful Story

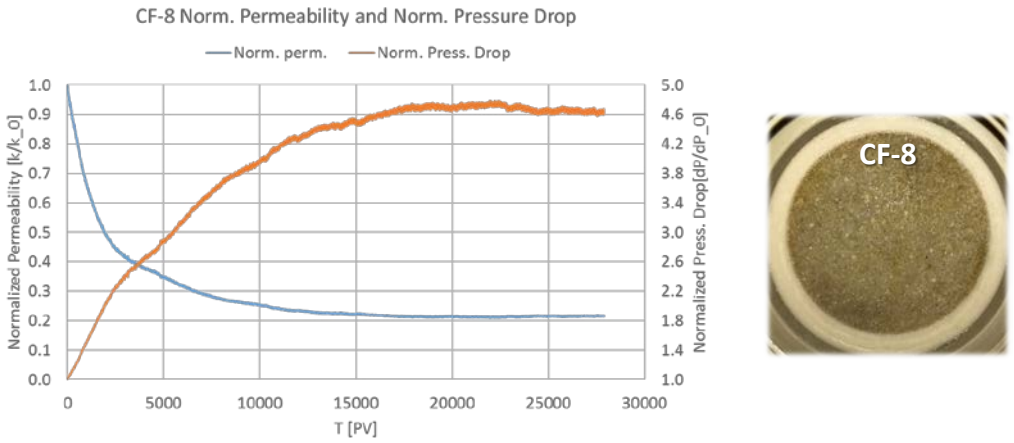

Figure C-1: Left: Norm. Permeability and pressure drop over PV injected, Right: Injection face of core after exp. CF-8

In CF-8, when injection was diverted to colloid from brine, ISCO Pump that was being used as injection pump broke. The failure was in one of the needle valves. As particles were already being injected, a new Quizix pump was immediately prepared to be installed in the setup. Quizix pump was thoroughly flushed with initially fresh water then brine but this pump still contained some 'alien' particles. The result obtained from CF-8 showed ~80% injectivity decline and no filter cake was observed as can be seen in *Figure C-1*. From obtained result it is hypothesized that new pump also contained nanoparticles as no EFC is seen. The nanoparticles where also negatively charged but less strong than silica nanoparticles that plugged the pores as can be seen in SEM image shown in Figure C-2, the left and middle images are at 1cm and 2cm away from injection face for CF-8 whereas right image is for CF-1 at 1 cm from injection face. CF-8 shows extensive plugging and cementation of particles in the pores whereas in CF-1 pores are clearly open.

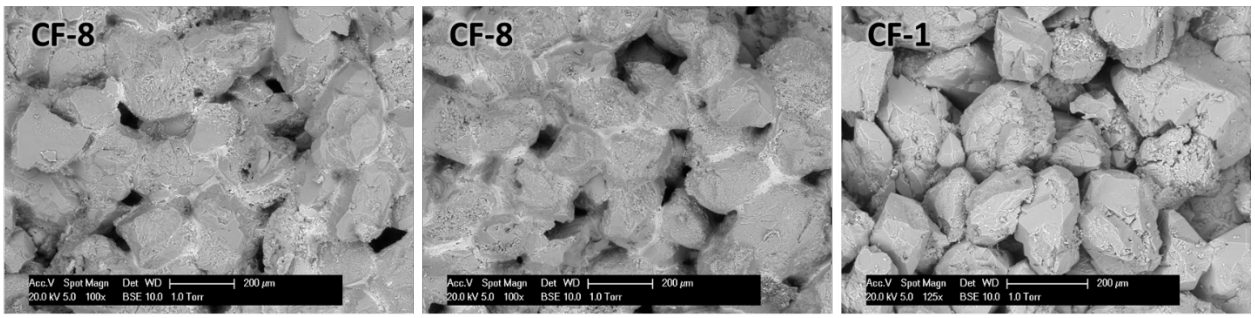

Figure C-2: Left and Middle: SEM image of CF-8 at 1cm and 2cm away from injection face respectively, Right: SEM image of CF-1 at 1cm away from injection face

Experiment CF-5 EFC

External filter cake developed on injection face of core plug used in CF-5 was carefully analysed using Leica MZ16-A stereomicroscope. The thickness of the cake was found to be 0.37mm.

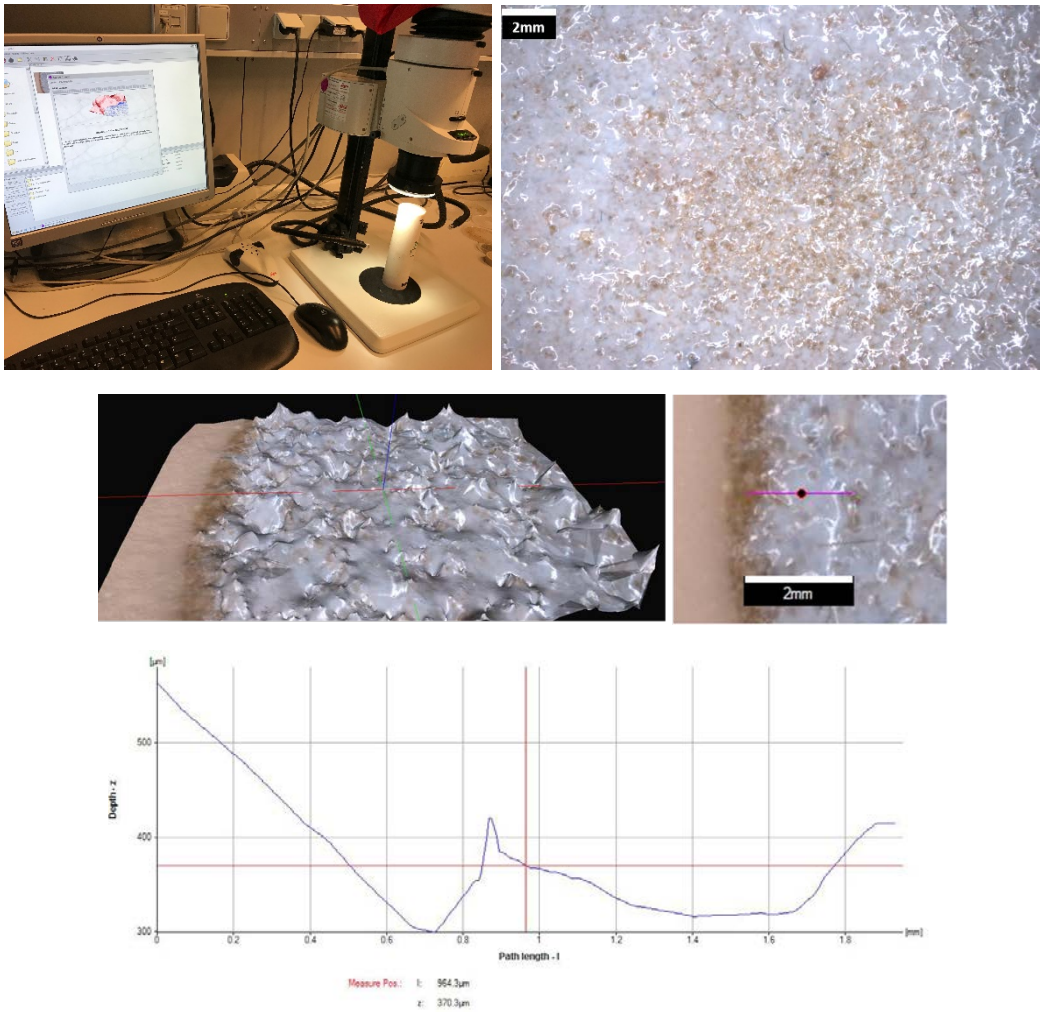

Figure C-3: a) Leica MZ16-A stereomicroscope, b) picture of EFC of CF-5, c) 3D image processing and calculation of external filter cake thickness

Core Plug Dimension Measurement

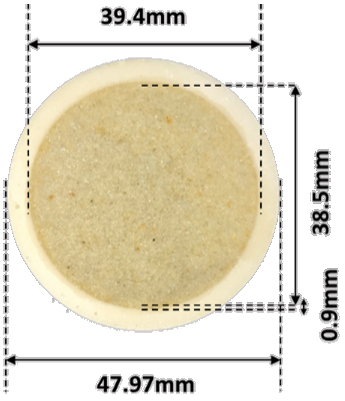

Figure C-4: X-Section measurement for core plugs

Influent/Effluent Analysis

Silica concentration profile over time for influent and effluent samples

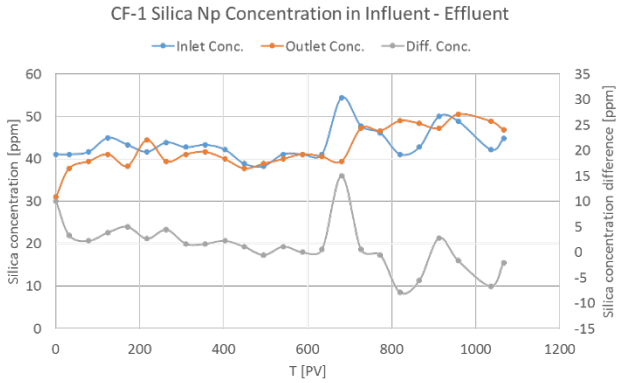

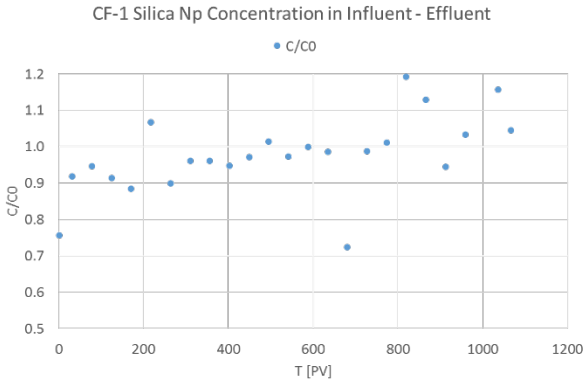

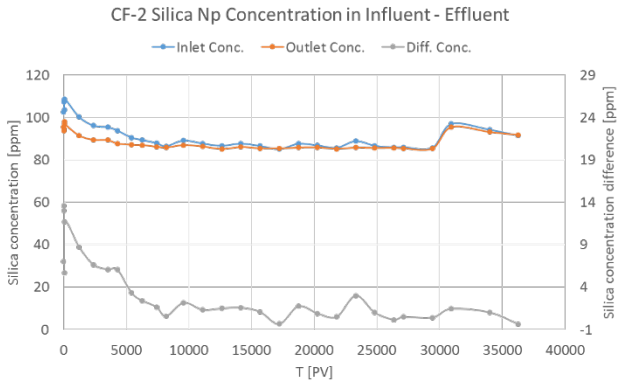

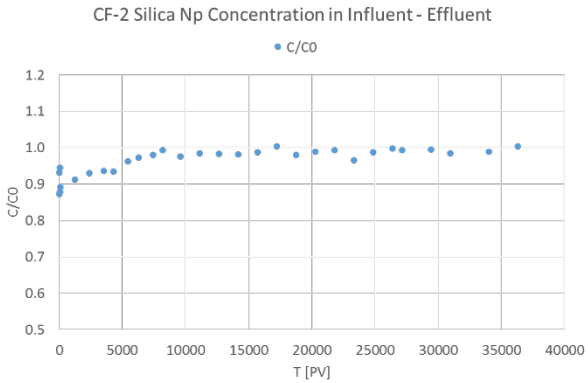

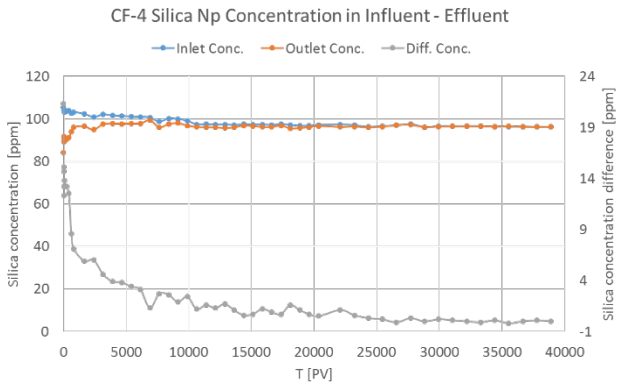

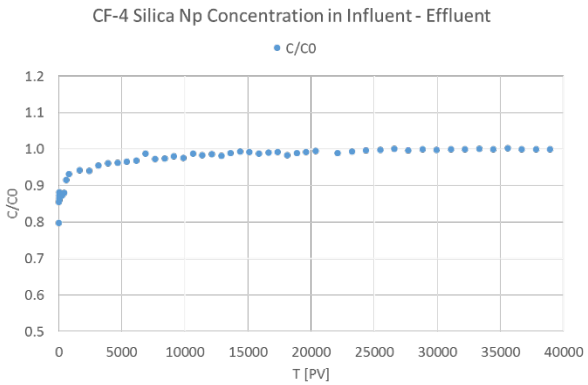

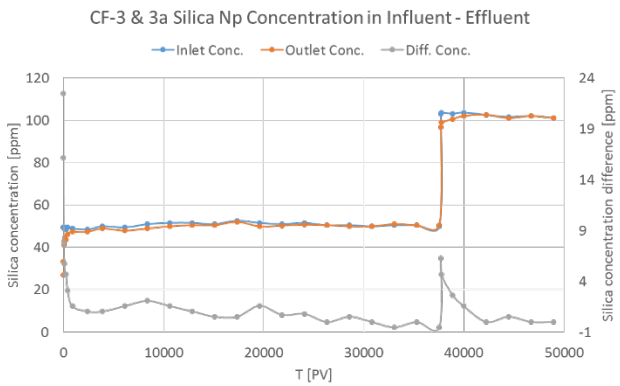

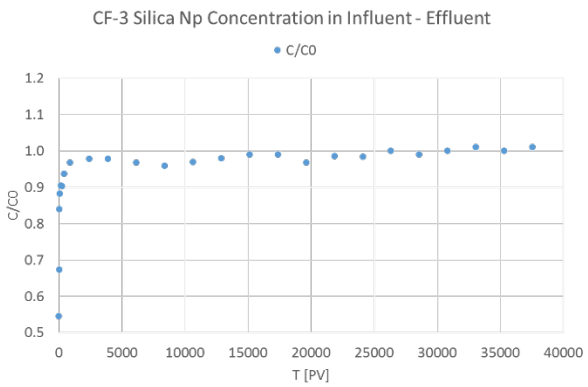

Permeability Calculation Plots

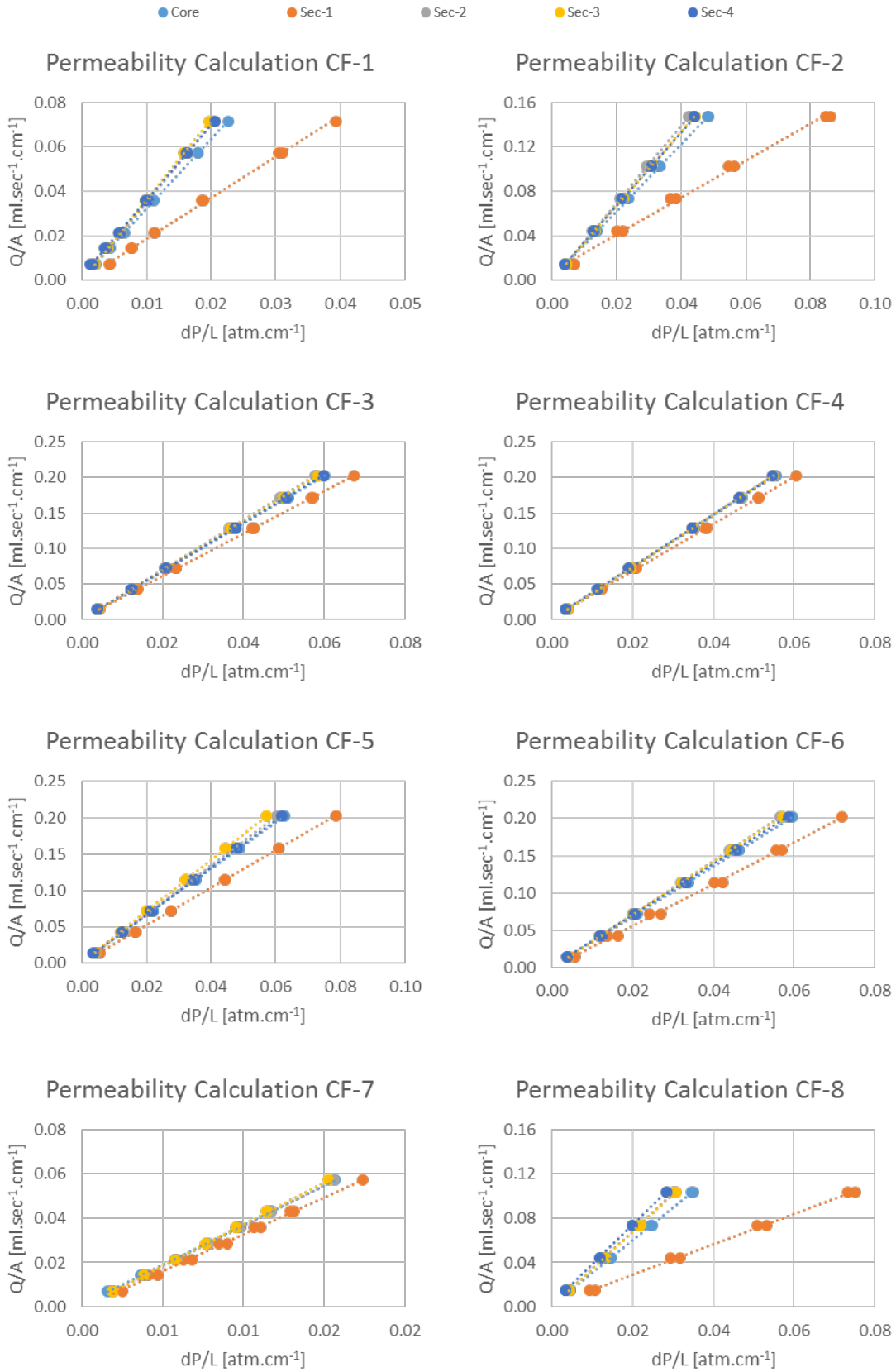

References

[1] S. Watson. How Geothermal Energy Works [Online]. Available: https://science.howstuffworks.com/environmental/energy/geothermal-energy.htm

[2] D. Bennion, F. Thomas, D. Imer, and T. Ma, "Water quality considerations resulting in the impaired injectivity of water injection and disposal wells," in *Canadian International Petroleum Conference*, 2000: Petroleum Society of Canada.

[3] C. Clark and J. Veil, "Produced water volumes and management practices in the United States," Argonne National Laboratory (ANL)2009.

[4] K. B. Gregory, R. D. Vidic, and D. A. Dzombak, "Water management challenges associated with the production of shale gas by hydraulic fracturing," *Elements,* vol. 7, no. 3, pp. 181-186, 2011.

[5] A. Kalantariasl, "Advanced analytical models for well injectivity decline," 2015.

[6] IOGP, "Environmental performance indicators 2014 data," IOPG2015, Available: http://www.iogp.org.

[7] J. Veil, "US produced water volumes and management practices in 2012," *Oklahoma City, OK: Ground Water Protection Council,* 2015.

[8] C. Clark, C. Harto, J. Sullivan, and M. Wang, "Water use in the development and operation of geothermal power plants," Argonne National Laboratory (ANL)2010.

[9] J. Herzig, D. Leclerc, and P. L. Goff, "Flow of suspensions through porous media—application to deep filtration," *Industrial & Engineering Chemistry,* vol. 62, no. 5, pp. 8-35, 1970.

[10] O. Vetter and V. Kandarpa, "Reinjection and injection of fluids in geothermal operations (state of the art)," Vetter Research, Costa Mesa, CA (USA)1982.

[11] F. Civan, "Formation damage mechanisms and their phenomenological modeling-an overview," in *European Formation Damage Conference*, 2007: Society of Petroleum Engineers.

[12] C. Gruesbeck and R. Collins, "Entrainment and deposition of fine particles in porous media," *Society of Petroleum Engineers Journal,* vol. 22, no. 06, pp. 847-856, 1982.

[13] L. Costier, P. J. van den Hoek, C. J. Davidson, M. Ding, H. van den Berg, and R. Hofland, "Predicting Water Injection Dynamics by Leading-edge Coreflood Testing," in *EUROPEC/EAGE Conference and Exhibition*, 2009: Society of Petroleum Engineers.

[14] T. Hofsaess and W. Kleinitz, "30 Years of Predicting Injectivity after Barkman & Davidson: Where are we today?," in *SPE European Formation Damage Conference*, 2003: Society of Petroleum Engineers.

[15] A. Vaz Jr, P. G. Bedrikovetsky, C. J. A. Furtado, A. G. Siqueira, and A. L. S. de Souza, "Effects of Residual Oil on Re-Injection of Produced Water," in *SPE Europec/EAGE Annual Conference and Exhibition*, 2006: Society of Petroleum Engineers.

[16] F. Civan, *Reservoir formation damage*. Gulf Professional Publishing, 2015.

[17] A. Kalantariasl *et al.*, "Injectivity during PWRI and Disposal in Thick Low Permeable Formations (Laboratory and Mathematical Modelling, Field Case)," in *SPE European Formation Damage Conference and Exhibition*, 2015: Society of Petroleum Engineers.

[18] J. H. Barkman and D. H. Davidson, "Measuring water quality and predicting well impairment," *Journal of Petroleum Technology,* vol. 24, no. 07, pp. 865-873, 1972.

[19] L. Nabzar, J.-P. Coste, and G. Chauveteau, "Water quality and well injectivity," in *IOR 1997-9th European Symposium on Improved Oil Recovery*, 1997.

[20] P. Bedrikovetsky, D. Marchesin, F. Shecaira, A. Souza, P. Milanez, and E. Rezende, "Characterisation of deep bed filtration system from laboratory pressure drop measurements," *Journal of Petroleum Science and Engineering,* vol. 32, no. 2, pp. 167-177, 2001.

[21] A. H. De Zwart, "Investigation of clogging processes in unconsolidated aquifers near water supply wells," 2007.

[22] A. Abrams, "Mud design to minimize rock impairment due to particle invasion," *Journal of petroleum technology,* vol. 29, no. 05, pp. 586-592, 1977.

[23] J. Eylander, "Suspended solids specifications for water injection from coreflood tests," in *SPE International Symposium on Oilfield Chemistry*, 1987: Society of Petroleum Engineers.

[24] Z. Khatib, "Prediction of formation damage due to suspended solids: Modeling approach of filter cake buildup in injectors," in *SPE Annual Technical Conference and Exhibition*, 1994: Society of Petroleum Engineers.

[25] X. Liu and F. Civan, "Formation damage and filter cake buildup in laboratory core tests: modeling and model-assisted analysis," *SPE Formation Evaluation,* vol. 11, no. 01, pp. 26-30, 1996.

[26] M. M. Sharma, S. Pang, K. E. Wennberg, and L. Morgenthaler, "Injectivity decline in water-injection wells: an offshore Gulf of Mexico case study," *SPE Production & Facilities,* vol. 15, no. 01, pp. 6-13, 2000.

[27] F. Altoe, P. Bedrikovetsky, A. Siqueira, A. Souza, and F. Shecaira, "Role of Dispersion in Injectivity Impairment: mathematical and laboratory study," in *SPE Annual Technical Conference and Exhibition*, 2004: Society of Petroleum Engineers.

[28] T. Yi, A. Fadili, M. N. Ibrahim, and B. S. Al-Matar, "Modeling the Effect of Asphaltene on the Development of the Marrat Field," in *8th European Formation Damage Conference*, 2009: Society of Petroleum Engineers.

[29] R. Farajzadeh, "Produced Water Re-Injection (PWRI), an Experimental Investigation into Internal Filtration and External Cake Build-up," *Faculty of Civil Engineering and Geosciences,* 2004.

[30] F. A. H. Al-Abduwani, "Internal filtration and external filter cake build-up in sandstones," TU Delft, Delft University of Technology, 2005.

[31] S. Buret, L. Nabzar, and A. Jada, "Water Quality and Well Injectivity: Do Residual Oil-in-Water Emulsions Matter?," *SPE Journal,* vol. 15, no. 02, pp. 557-568, 2010.

[32] M. Bader, "Sulfate scale problems in oil fields water injection operations," *Desalination,* vol. 201, no. 1-3, pp. 100-105, 2006.

[33] E. A. Vik and A. J. Dinning, "Produced Water Re-Injection-The Potential to Become an Improved Oil Recovery Method," *Exploration & Production Oil & Gas Review,* vol. 7, no. 1, pp. 1-3, 2009.

[34] N. Morrow and J. Buckley, "Improved oil recovery by low-salinity waterflooding," *Journal of Petroleum Technology,* vol. 63, no. 05, pp. 106-112, 2011.

[35] F. Civan, "Practical model for compressive cake filtration including fine particle invasion," *AIChE journal,* vol. 44, no. 11, pp. 2388-2398, 1998.

[36] E. C. Donaldson, B. A. Baker, and H. Carroll, "Particle transport in sandstones," in *SPE Annual Fall Technical Conference and Exhibition*, 1977: Society of Petroleum Engineers.

[37] A. C. Todd, J. Somerville, and G. Scott, "The application of depth of formation damage measurements in predicting water injectivity decline," in *SPE Formation Damage Control Symposium*, 1984: Society of Petroleum Engineers.

[38] O. Vetter, V. Kandarpa, M. Stratton, and E. Veith, "Particle invasion into porous medium and related injectivity problems," in *SPE international symposium on oilfield chemistry*, 1987: Society of Petroleum Engineers.

[39] R. C. Yerramilli, P. Zitha, S. S. Yerramilli, and P. Bedrikovetsky, "A novel water injectivity model and experimental validation using CT scanned core-floods," in *SPE European Formation Damage Conference & Exhibition*, 2013: Society of Petroleum Engineers.

[40] J. Wang, X. Teng, H. Wang, and H. Ban, "Characterizing the metal adsorption capability of a class F coal fly ash," *Environmental science & technology,* vol. 38, no. 24, pp. 6710-6715, 2004.

[41] E. S. Boek, A. Fadili, M. J. Williams, and J. Padding, "Prediction of asphaltene deposition in porous media by systematic upscaling from a colloidal pore scale model to a deep bed filtration model," in *SPE Annual Technical Conference and Exhibition*, 2011: Society of Petroleum Engineers.

[42] E. U. M. SCHLUMBERGER, "Technical Description," *Schlumberger Ltd,* 2009.

[43] M. Elimelech, J. Gregory, and X. Jia, *Particle deposition and aggregation: measurement, modelling and simulation*. Butterworth-Heinemann, 2013.

[44] P. Vilks, H. Miller, and D. Doern, "Natural colloids and suspended particles in the Whiteshell Research Area, Manitoba, Canada, and their potential effect on radiocolloid formation," *Applied Geochemistry,* vol. 6, no. 5, pp. 565-574, 1991.

[45] C. C. Patton, "Injection-water quality," *Journal of Petroleum Technology,* vol. 42, no. 10, pp. 1,238-1,240, 1990.

[46] J. N. Ryan and M. Elimelech, "Colloid mobilization and transport in groundwater," *Colloids and surfaces A: Physicochemical and engineering aspects,* vol. 107, pp. 1-56, 1996.

[47] W. Stumm, *Chemistry of the solid-water interface: processes at the mineral-water and particle-water interface in natural systems*. John Wiley & Son Inc., 1992.

[48] K. K. Mohan and H. S. Fogler, "Colloidally induced smectitic fines migration: existence of microquakes," *AIChE journal,* vol. 43, no. 3, pp. 565-576, 1997.

[49] S. R. Bishop, "The experimental investigation of formation damage due to the induced flocculation of clays within a sandstone pore structure by a high salinity brine," in *SPE European Formation Damage Conference*, 1997: Society of Petroleum Engineers.

[50] A. A. Tchistiakov, "Colloid chemistry of in-situ clay-induced formation damage," in *SPE International Symposium on Formation Damage Control*, 2000: Society of Petroleum Engineers.

[51] R. J. Hunter, *Foundations of colloid science*. Oxford University Press, 2001.

[52] W. Hower, R. Lasater, and R. Mihram, "Compatibility of injection fluids with reservoir components," 1972.

[53] S. Wang and F. Civan, "Modeling formation damage by asphaltene deposition during primary oil recovery," *Journal of energy resources technology,* vol. 127, no. 4, pp. 310-317, 2005.

[54] E. M. LaBolle, J. Quastel, and G. E. Fogg, "Diffusion theory for transport in porous media: Transition-probability densities of diffusion processes corresponding to

advection-dispersion equations," *Water Resources Research,* vol. 34, no. 7, pp. 1685-1693, 1998.

[55] M. T. Van Genuchten and P. Wierenga, "Solute dispersion coefficients and retardation factors," *Methods of Soil Analysis: Part 1—Physical and Mineralogical Methods,* no. methodsofsoilan1, pp. 1025-1054, 1986.

[56] G. Chauveteau and K. Sorbie, *Mobility control by polymers*. Elsevier Science Publishers, 1991.

[57] A. E. Peksa, K.-H. A. Wolf, and P. L. Zitha, "Bentheimer sandstone revisited for experimental purposes," *Marine and Petroleum Geology,* vol. 67, pp. 701-719, 2015.

[58] N. Lenchenkov and C. van Kruijsdijk, "Conformance Control in Heterogeneous Oil Reservoirs with Polymer Gels and Nano-Spheres."

[59] R. Yerramilli, "Water injectivity prediction: Experiments and modeling," 2012.

[60] R. Lawson, T. Gresham, I. Richardson, F. Siega, and S. Addison, "LONG RUN POLYMERIZATION EXPERIMENTS AT THE KAWERAU GEOTHERMAL LIMITED POWER PLANT," in *Proceedings 38th New Zealand Geothermal Workshop*, 2016, vol. 23, p. 25.

[61] T. Coradin, D. Eglin, and J. Livage, "The silicomolybdic acid spectrophotometric method and its application to silicate/biopolymer interaction studies," *Journal of Spectroscopy,* vol. 18, no. 4, pp. 567-576, 2004.

[62] P. Shutong and M. M. Sharma, "A model for predicting injectivity decline in water-injection wells," *SPE Formation Evaluation,* vol. 12, no. 03, pp. 194-201, 1997.

[63] P. G. Bedrikovetsky, C. J. A. Furtado, A. Siqueira, and A. L. S. de Souza, "A comprehensive model for injectivity decline prediction during PWRI," in *European Formation Damage Conference*, 2007: Society of Petroleum Engineers.

[64] P. G. Bedrikovetsky, E. J. Mackay, R. M. Silva, F. M. Patricio, and F. F. Rosário, "Produced water re-injection with seawater treated by sulphate reduction plant: Injectivity decline, analytical model," *Journal of Petroleum Science and Engineering,* vol. 68, no. 1, pp. 19-28, 2009.

[65] P. Bedrikovetsky, A. S. Vaz, C. J. Furtado, and A. R. Serra de Souza, "Formation-damage evaluation from nonlinear skin growth during coreflooding," *SPE Reservoir Evaluation & Engineering,* vol. 14, no. 02, pp. 193-203, 2011.